4-2001

Study of Automotive Hydromount Mechanism

Min Lu
Western Michigan University

STUDY OF AUTOMOTIVE HYDROMOUNT MECHANISM

by

Min Lu

A Dissertation
Submitted to the
Faculty of The Graduate College
in partial fulfillment of the
Degree of Doctor of Philosophy
Department of Mechanical and Aeronautical Engineering

Western Michigan University
Kalamazoo, Michigan
April 2001

STUDY OF AUTOMOTIVE HYDROMOUNT MECHANISM

Min Lu, Ph.D.

Western Michigan University, 2001

The hydromount mechanism is studied. It was determined that the dynamic characteristics of the hydromounts are related to the rubber static stiffness, rubber damping coefficient, volumetric stiffness, and effectiveness of the oscillating fluid in the inertia track. At high frequencies the motion of the fluid in the inertia track diminishes so that its effect is negligible and may be ignored. It is also concluded that the rubber damping has a minimal effect on the hydromount dynamic properties and may be neglected. The maximum loss angle, which corresponds to the maximum damping coefficient of the hydromount, occurs near the inertia track fluid resonant frequency. The degree of this proximity depends on the damping ratio and dynamic stiffness ratio. Through a parametric study it was found that a higher rubber static stiffness results in a higher peak dynamic stiffness, but at a lower peak loss angle. Increasing the volumetric stiffness, fluid density, or inertia track cross-sectional area and length results in an increase of the peak dynamic stiffness and peak loss angle. A larger equivalent piston area results in lower peak dynamic stiffness and peak loss angle. The inertia track damping coefficient, generated by the oscillating fluid between chambers, is a function of the frequency along with other variables: inertia track equivalent radius, length, fluid density and viscosity. The predicted dynamic characteristics of a variety of hydromounts match reasonably well with test results.

INFORMATION TO USERS

This manuscript has been reproduced from the microfilm master. UMI films the text directly from the original or copy submitted. Thus, some thesis and dissertation copies are in typewriter face, while others may be from any type of computer printer.

The quality of this reproduction is dependent upon the quality of the copy submitted. Broken or indistinct print, colored or poor quality illustrations and photographs, print bleedthrough, substandard margins, and improper alignment can adversely affect reproduction.

In the unlikely event that the author did not send UMI a complete manuscript and there are missing pages, these will be noted. Also, if unauthorized copyright material had to be removed, a note will indicate the deletion.

Oversize materials (e.g., maps, drawings, charts) are reproduced by sectioning the original, beginning at the upper left-hand corner and continuing from left to right in equal sections with small overlaps.

Photographs included in the original manuscript have been reproduced xerographically in this copy. Higher quality 6" x 9" black and white photographic prints are available for any photographs or illustrations appearing in this copy for an additional charge. Contact UMI directly to order.

Bell & Howell Information and Learning
300 North Zeeb Road, Ann Arbor, MI 48106-1346 USA
800-521-0600

Bell & Howell Information and Learning Company
300 North Zeeb Road
P.O. Box 1346
Ann Arbor, MI 48106-1346

ACKNOWLEDGMENTS

It is my illiterate parents who have been my spiritual support in my deep soul for the successful completion of my Ph.D. program. I would also like to thank my wife, Wan-Su Chen, for her support and understand during the most stressful years of my life. Such a strong guilt has remained in my heart to my three children, Vicki, Michael and Andrew, who were all born during the period of my doctoral education, for not having time with them. Dr. Judah Ari-Gur's patience and encouragement were the main force driving me strong when I was down. Jim Vance, Louis Mattia and Pat Corcoran's support between my job and education is deeply appreciated. Gratitude is expressed to the members of my graduate committee, Dr. Iskender Sahin, Dr. James Kamman and Dr. Frank Severance, for their time and advice. John Garety's help in experiment during the research is also deeply appreciated.

Min Lu

TABLE OF CONTENTS

Table of Contents—continued

Table of Contents--continued

Table of Contents—continued

Table of Contents—continued

LIST OF TABLES

LIST OF FIGURES

List of Figures-Continued

List of Figures-Continued

List of Figures-Continued

List of Figures-Continued

List of Figures-Continued

CHAPTER I

INTRODUCTION

In this chapter, the hydromount device is described by the introduction of vehicle vibration sources, isolation approaches, the characteristics of the ideal mount and the conventional rubber mounts. The need for this research is justified following the literature review. The goal and scope of the research are then presented. At the end, the dissertation organization is given.

Vehicle Vibration Sources

The vibration which engine mounts need to isolate comes from two sources: road input featuring the relatively high amplitude displacement vibration, and engine imbalance force featuring the noise. The frequency range of the road input is about 0-30 Hz, while the frequency range of the engine imbalanced force is 30-200 Hz (Brach and Haddow, 1993).

Isolation of Vehicle Vibration

Vibration is inevitable for the vehicle, but a properly designed system can reduce the vibration to a minimum. There are two approaches to vibration reduction. The first is that of optimizing mount placement. By positioning the mount and orientation properly, the vibration can be reduced significantly. On the other hand, properly choosing the dynamic characteristics of the mounts, namely their dynamic stiffness and damping level,

to reduce the vibration is the goal of the mount characteristic approach. The research performed for this dissertation falls within the second category.

Ideal Mounts

The mount characteristic approach deals with the optimization of the mount dynamic characteristics, which are its dynamic stiffness and damping level. Dynamic stiffness is defined as the frequency dependent load amplitude divided by its displacement amplitude. Damping is normally measured by the phase difference between the load and the displacement. Since the phase is zero for zero damping and it increases for higher damping, it is often referred to as the loss angle. Occasionally, both terms, phase angle and loss angle, are interchangeable. Ideally the best mounts are those which meet the requirements (Brach and Haddow, 1993): a) high stiffness and high damping at low frequencies; b) low stiffness and low damping at high frequencies.

Conventional Rubber Mounts

The advantage of the rubber mount is that it is simple and easy to manufacture, but it is impossible by its nature to tune its maximum damping into the frequency where the system resonates. So it is impossible for conventional rubber mounts to meet the conflicting mount design requirements: large stiffness and large damping at low frequencies and low stiffness and low damping at high frequencies.

A picture of a rubber mount is presented in Figure 1.1. The typical dynamic properties of a rubber mount are illustrated in Figure 1.2, where the dynamic stiffness and loss angle are presented as a function of frequency.

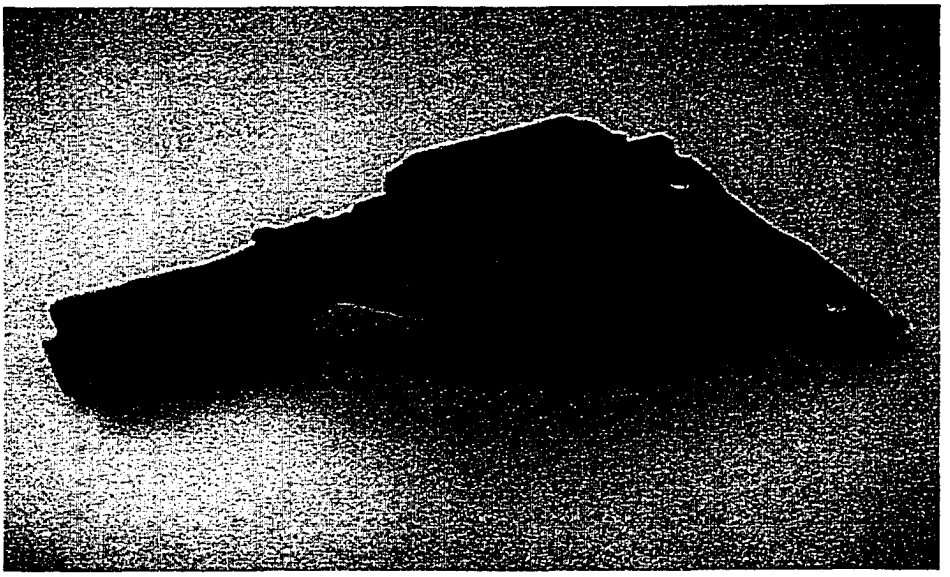

Figure 1.1. Photo of a Rubber Mount

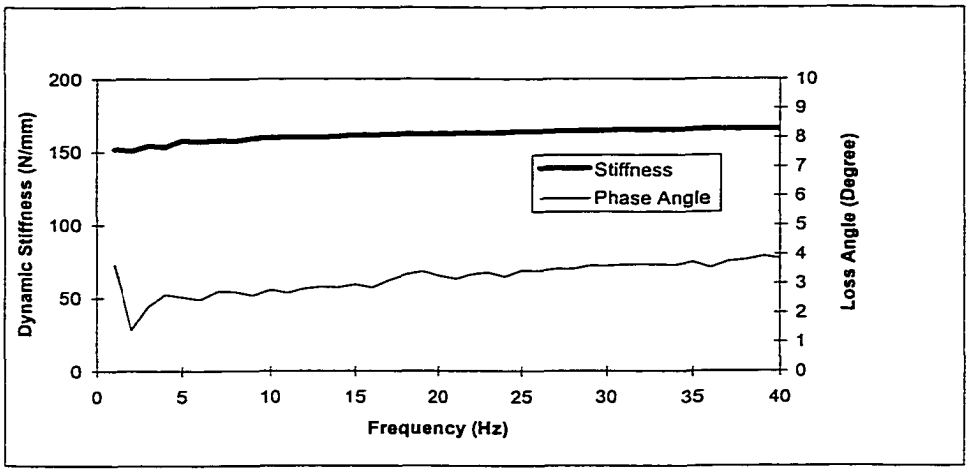

Figure 1.2. Typical Dynamic Characteristics of a Rubber Mount

Hydromounts

The basic layout of a hydromount consists of a main rubber element, an upper chamber, a channel plate, an inertia track, a lower chamber and a bellow (Figure 1.3). The chambers are filled with a hydraulic fluid that flows back and forth between the upper and lower chambers through the inertia track. To illustrate the effectiveness of the fluid, the dynamic characteristics of a hydromount with and without fluid inside the mount are compared in Figure 1.4.

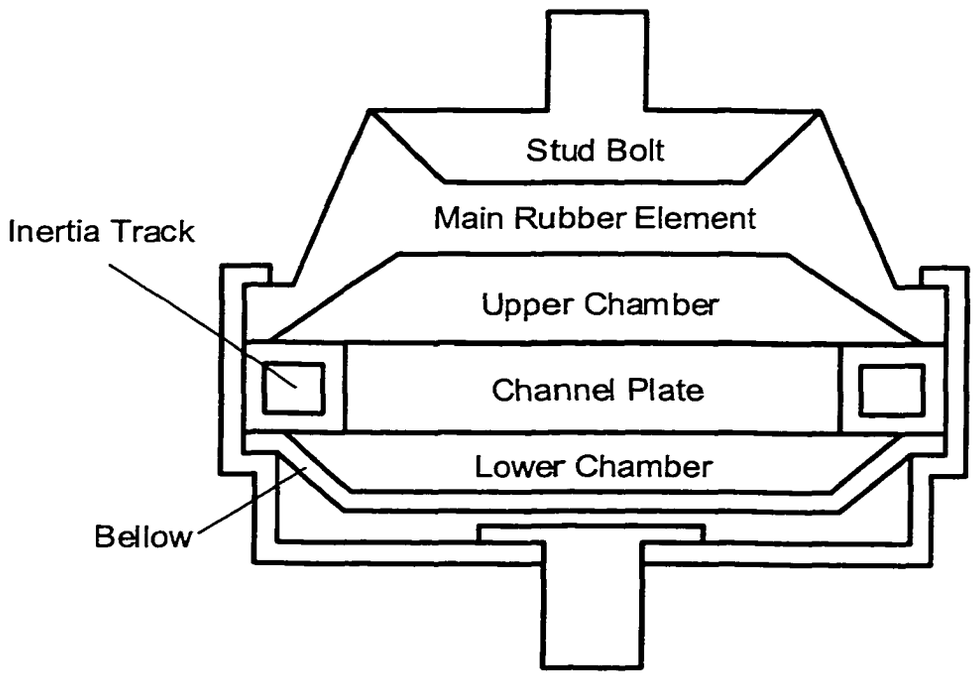

Figure 1.3. Basic Layout of the Hydromount

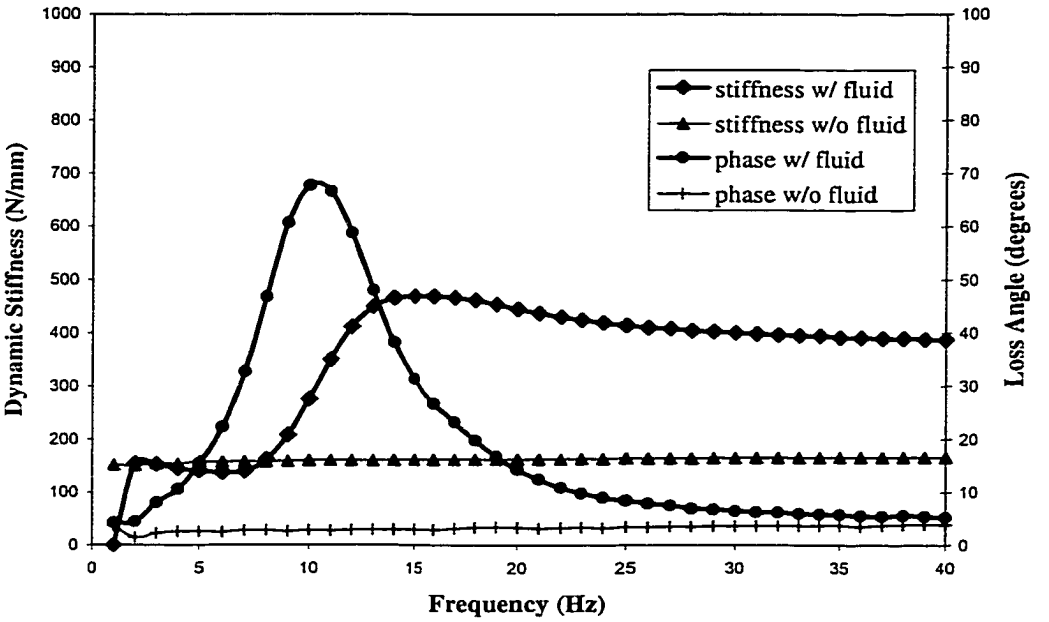

Figure 1.4. Dynamic Characteristics of a Hydromount With and Without Fluid

It is seen that the hydromount has peak values of dynamic stiffness and damping at a low frequency, and the stiffness and damping decrease at high frequencies. It meets the mount design requirements: large stiffness and large damping at practically low frequencies and low stiffness and low damping at high frequencies.

Hydromount With Decoupler

The mounts with low stiffness and low damping at high frequencies result in a good isolation of vibration. However, because of the fluid inside the hydromount, its dynamic stiffness cannot be designed as low as desired. Adding a membrane-like floating element, a decoupler, between the two chambers in the hydromount (Figure 1.5) results in a low stiffness of the mounts for the low amplitude vibration, typical to the high frequency noise, because the fluid flows around the floating decoupler and bypasses the

inertia track. Therefore, when the fluid effect is eliminated, the mount behavior resembles a rubber mount. However, in the large amplitude (low frequency) range, the decoupler is pushed to seal the bypass and the flow between the chambers is forced to go through the inertia track. In Figure 1.6 the typical dynamic characteristics of a hydromount with decoupler are shown for the cases of low amplitude (0.1 mm) and high amplitude (1.0 mm) vibration. It shows that for 0.1 mm amplitude the mount behaves like a rubber mount, but for 1.0 mm amplitude, it functions as a hydromount.

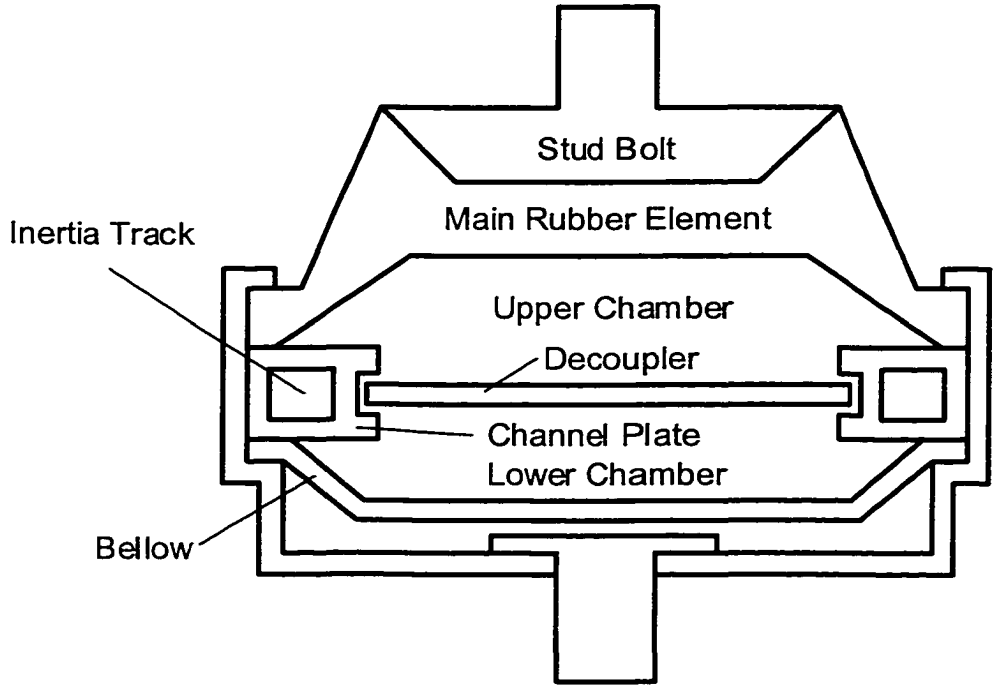

Figure 1.5. Basic Layout of the Hydromount With Decoupler

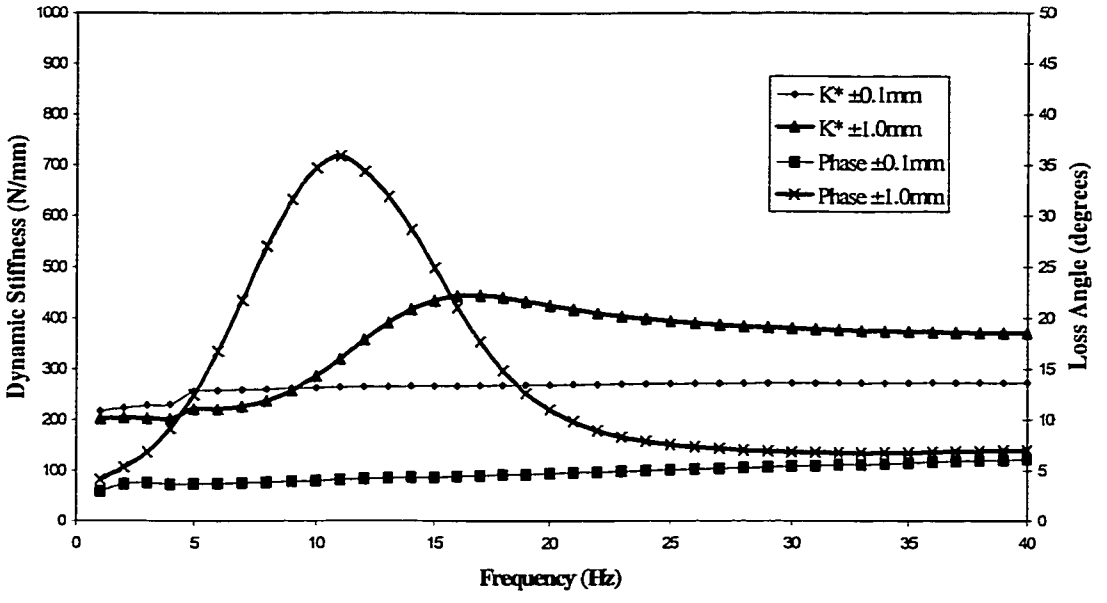

Figure 1.6. Dynamic Characteristics of a Hydromount With Decoupler

Literature Review

The literature review is comprised of two sections: hydromount (without decoupler) and hydromount with decoupler. At the end, the comments on literature will be made.

Hydromount

General Motors Corporation patented a hydraulic engine mount for the purpose of providing increased damping in 1962. However, it was not until 1984 that the first research paper, "A New Generation of Engine Mounts" was presented in SAE conference by Bernuchon (1984), who proposed a linear two-degrees-of-freedom model of the system (Figure 1.7) but did not perform any analysis. Corcoran and Ticks (1984) used the concept of stiffness factor, which is the ratio of the damping spring stiffness *NK* (dynamic

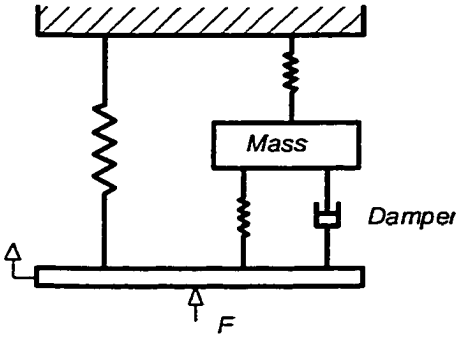

Figure 1.7. Hydromount Model Proposed by Bernuchon (1984)

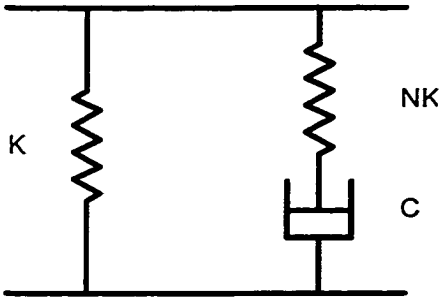

Figure 1.8. Hydromount Model Proposed by Corcoran and Ticks (1984)

stiffness) to the suspension spring stiffness K (static stiffness), and discussed the hydromount mechanism based on a single-degree-of-freedom model (Figure 1.8). They found that their hydromount model displayed a large spring factor N (=NK/K) at engine resonance (normally between 5 to 15 Hz) and a low spring factor thereafter. Their work explained the fact that hydromounts possess high dynamic stiffness at low frequencies and low stiffness at high frequencies. Muzechuk (1984) proposed his version of a hydromount model (Figure 1.9) based on the parameters he defined as bulge stiffness, damping coefficient, diaphragm stiffness and free soft travel. But he did not perform any analysis using this model. Flower (1985) proposed a hydromount model shown in Figure

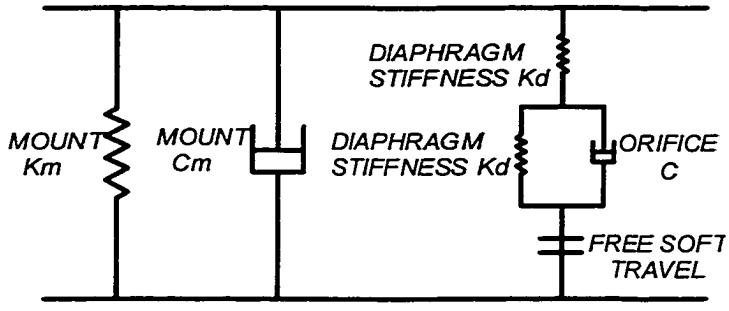

Figure 1.9. Hydromount Model Proposed by Muzechuk (1984)

1.10, where K_R is the static stiffness, R_R is the damping coefficient of the main rubber element, A_p is the piston area, A_t is the cross-sectional area of inertia track, C_T is the compliance of the top chamber that can be expressed as the ratio of top chamber volume change to the pressure change, I_f is the fluid inertia which is inversely proportional to A_t, C_B is the bottom compliance, and R_0 is the damping of the inertia track. He used bond graph techniques to develop the dynamic stiffness expressed by

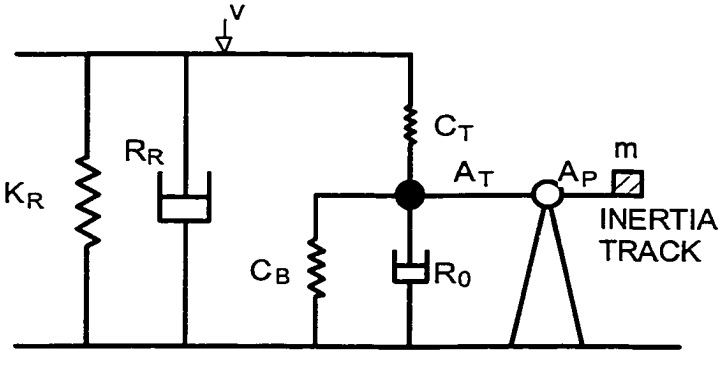

Figure 1.10. Hydromount Model Proposed by Flower (1985)

$$k_{dy} = k_R + j\omega R_R + \frac{A_p^{\,2}}{C_T} \bullet \frac{\frac{1}{I_f}\frac{1}{C_B} - \omega^2 + j\frac{R_0}{I_f}\omega}{\frac{1}{I_f}\left(\frac{1}{C_B} + \frac{1}{C_T}\right) - \omega^2 + j\frac{R_0}{I_f}\omega} \tag{1.1}$$

He also found that the undamped natural frequency of the liquid in the inertia track is given by

$$\omega_N^{\,2} = \frac{1}{I_f}\left(\frac{1}{C_B} + \frac{1}{C_T}\right) \tag{1.2}$$

Although his theoretical prediction did not agree well with the experimental result, Flower's hydromount model made a fundamental contribution in easy explanation of the fluid mass effect to the hydromount dynamic characteristics: the equivalent mass of fluid in the inertia track is amplified by A_p/A_t. Clark (1985) proposed a two-degrees-of-freedom model (Figure 1.11) for a mount that has an inertia track. In his model, *K1* is the shear stiffness of the main spring; *C1* is the internal rubber damping of the main spring in shear; *K2* is the bulge stiffness of the main spring; *C2* is the internal rubber damping of the main spring in bulge; *K3* is the secondary spring stiffness; *C3* is the internal rubber damping of the secondary spring; *K4* is the auxiliary spring stiffness; *C4* is the damping due to fluid flow in the damping channel; *M* is the equivalent vibratory mass; *x(t)* is the input displacement; *F(t)* is the transmitted force on the supporting foundation. But he further assumed that the equivalent vibratory mass *M* is not significant for low frequencies (0-20 Hz), which contradicts Flower's model, so that his analytical model becomes similar to Corcoran's model (see Figure 1.8), which is over simplified. The hydromount model shown in Figure 1.12 was proposed by Sugino and Abe (1986). In their model, f_0 is the resonant frequency of the fluid inside orifice; k_1 is the supporting

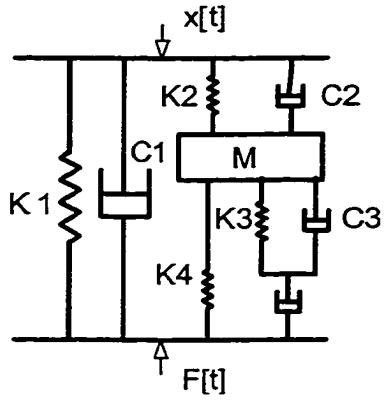

Figure 1.11. Hydromount Model Proposed by Clark (1985)

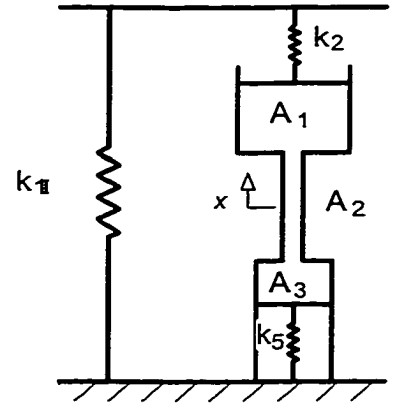

Figure 1.12. Hydromount Model Proposed by Sugino and Abe(1986)

elasticity; k_2 is the expansion elasticity; k_5 is the equivalent elasticity of air chamber; k_{st} is the static spring constant; $k_{d\infty}$ is the dynamic spring constant when frequency is sufficiently high; m is the mass of fluid inside orifice; ρ is the density of fluid; c is the damping coefficient of orifice; A_1 is the effective area of rubber; A_2 is the cross-sectional

area of orifice; A_3 is the effective area of air chamber; l is the length of orifice; F is the transmission force. They produced three main results, which are expressed by

$$f_0 = \frac{1}{2\pi}\sqrt{\frac{k_2 + \left(\frac{A_1}{A_3}\right)^2 k_5}{\left(\frac{A_1}{A_2}\right)^2 m}} \tag{1.3}$$

$$k_{st} = k_1 + \frac{\left(\frac{A_1}{A_3}\right)^2 k_2 k_5}{k_2 + \left(\frac{A_1}{A_3}\right)^2 k_5} \tag{1.4}$$

$$k_{d\infty} = k_1 + k_2\left(1 - \frac{A_2}{A_1}\right) \approx k_1 + k_2. \tag{1.5}$$

Again, those analytical results are unable to be verified by experiments except for equation 1.5. In studying semi-active hydraulic engine mounts in his Ph.D. research, Graf (1987) considered the mount as a multi-input multi-output linear system. The mechanical impedance of the system was assumed as

$$Z(\omega) = \frac{F(j\omega)}{x(j\omega)} = j\omega c + k \tag{1.6}$$

where the real part of the mechanical impedance is the stiffness of the viscoelastic element, and the imaginary part contains the product of the damping rate and frequency.

In deriving the mechanical impedance by a state-space model, Graf used the linear relationship between the pressure Δp and volume flow rate q as

$$\Delta p = \frac{128\mu l}{\pi d^4} q \tag{1.7}$$

where l is the length of the inertia track, d is the diameter of inertia track and μ is the fluid viscosity. Equation 1.7 is based on the assumption of fully-developed one-dimensional, steady-state laminar flow (Rosenberg and Karnopp, 1983). Seto et al (1991) modeled the hydromount as a vibration absorber, shown in Figure 1.13, in which A_u, A_0 and A_b are the mean cross-sectional areas of the upper chamber, the orifice, and the lower chamber respectively; K_m and K_e are the stiffnesses of the structural and hydraulic springs; X_u, X_0 and X_b are the flow displacements in the upper chamber, in the orifice and in the lower chamber; m is the mass of flow in the orifice. They used optimization theory to minimize the ratio of the engine displacement to the frame displacement. The prediction of the dynamic characteristics was not of interest of the paper. Kim and Singh (1992, 1993) developed a linear time invariant model of the mount using lumped mechanical and fluid elements as shown in Figure 1.14, in which *#1*, *#2* and *#I* are the control volumes of the upper chamber, lower chamber and inertia track respectively; $P_1(t)$ and $P_2(t)$ are the pressure in the upper and lower chambers; I_i is the time-invariant inertances of *#i* ($I_i = \rho l/A$, where ρ is the fluid density; l is the inertia track length; and A is the inertia track cross-sectional area); q_i is the volume flow rate; R_i is the nonlinear fluid resistance; and C_1 and C_2 are the nonlinear compliance of *#1* and *#2*. They assumed that the flow inside the hydromount is an oscillating turbulent flow that is not amenable to an

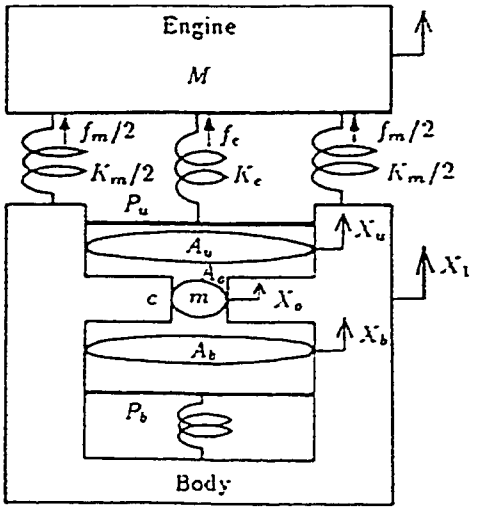

Figure 1.13. Hydromount Model Proposed by Seto et al (1991)

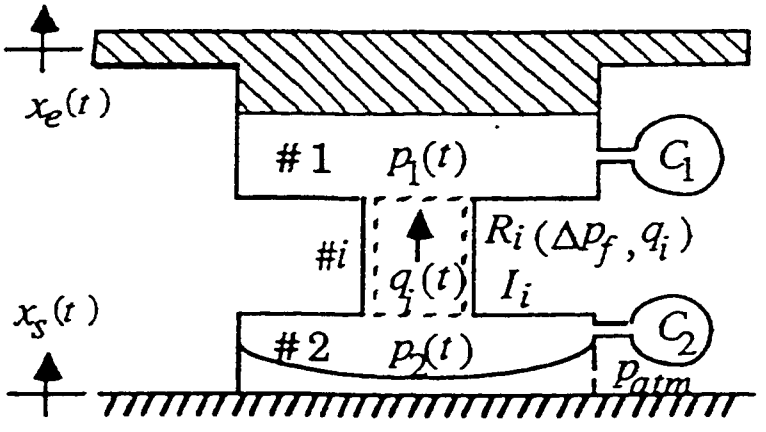

Figure 1.14. Hydromount Model Proposed by Kim (1993)

accurate analysis. Therefore, in order to use their model, the mount has to be built to have its flow parameters tested. Gau and Cotton (1995) performed an experimental parametric study of hydromount dynamic characteristics. They found that the peak of the dynamic stiffness increases as the volumetric stiffness, fluid density, inertia track cross-sectional area, or inertia track length increase; it decreases with the fluid viscosity increases. The resonant frequency increases as the volumetric stiffness and inertia track cross-sectional area increase; it decreases as the fluid density, fluid viscosity and inertia track length increase.

Hydromount With Decoupler

After analyzing the single degree of freedom model of a hydromount, Corcoran and Ticks (1984) concluded that the hydromount displayed a large spring factor (N) at low frequencies and low spring factor at high frequencies. They then proposed to add a "clearance space", now known as a decoupler, into the hydromount. Researchers like Muzechuk (1984) and Flower (1985), mentioned the decoupler in their hydromount model but did not perform any analysis with it. Singh et al (1992) performed linear and non-linear analyses of hydromounts with decoupler effects using lumped mechanical and fluid elements. Further analytical work based on Kim and Singh's hydromount with decoupler model was done by Royston (1997). However, because of the complexity of the parameters, the theory is not suitable for practical applications.

Comments on Published Literature

The hydromount has generated interest among many researchers since the early 1980's. To this date, no unified theory has yet been published. The published models

explain certain features of the hydromounts successfully but then fail to explain others. There is a need for more research toward the development of better and more comprehensive models.

The Goal of the Proposed Research

The goal of the proposed research is to develop a theory to predict the dynamic characteristics of hydromounts based on the parameters which are determinable in the design stage, so that the research results can be directly used in designing the hydromounts. The theory should explain hydromount features mathematically. The contribution of the proposed research is to change the trial and error method that is used in current hydromount development to a scientifically guided design theory.

Scope of Research

To achieve the stated goal, the following objectives have to be accomplished:

To identify a set of practical parameters that characterize hydromounts;

To develop a mathematical model that accurately describes the behavior of hydromounts. From this, to derive the equations of dynamic stiffness and phase angle;

To validate the theoretical model experimentally.

Dissertation Organization

This dissertation is organized into six chapters. Chapter I has provided the motivation for the proposed research, described relevant technical aspects, and outlined the scope of the research. Chapter II concentrates on hydromount fundamentals, such as the definition of dynamic stiffness and phase angle, rubber dynamic properties etc.,

which are relevant to the hydromount modeling. An experimental study on rubber dynamic properties is conducted within this chapter. Chapter III introduces a mathematical model of the hydromount with the lumped inertia track fluid damping coefficient. The equations of the dynamic properties of the hydromount are derived. The phenomena of the hydromount locking mechanism, the frequency at the maximum loss angle and the stiffness dip are investigated. Chapter IV includes the hydromount with multiple inertia tracks. The effect of the number of inertia tracks on the fluid resonant frequency, the fluid displacement in the inertia track, the equivalent piston displacement, the fluid pressure difference, the dynamic stiffness and loss angle are discussed. In Chapter V the inertia track damping mechanism is studied based on the assumption that the flow inside the inertia track is an oscillating laminar flow. The equation of the fluid damping coefficient is developed. At the end of the chapter, experimental validation of the hydromount model is performed. The summary and conclusions of this dissertation are presented in Chapter VI.

CHAPTER II

HYDROMOUNT FUNDAMENTALS

This chapter deals with hydromount fundamentals. The definitions of the dynamic stiffness, loss angle and damping coefficient are revisited. Because a generic hydromount is composed of a rubber element and a damping generating mechanism (inertia track), the rubber dynamic properties are also studied.

Dynamic Stiffness and Loss Angle

To define the dynamic stiffness and loss angle, a spring mass system shown in Figure 2.1 is employed, where M, k_s and c are the mass, static stiffness and damping coefficient respectively. F_t is the force disturbance. The equation of motion is

$$M\ddot{x} + c\dot{x} + k_s x = F_t \tag{2.1}$$

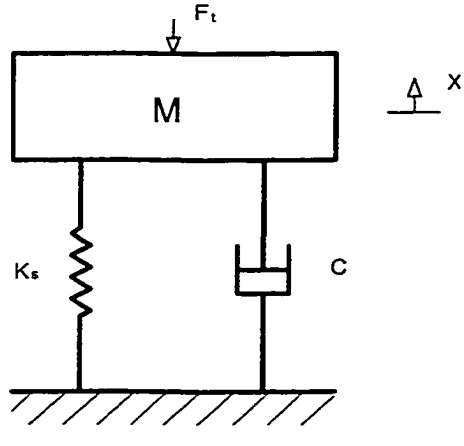

Figure 2.1. A Spring Mass System

The displacement solution of the form

$$x = X_0 e^{i\omega t} \tag{2.2}$$

is used. X_0 is the displacement amplitude for the applied oscillating load

$$F_t = F_0 e^{i(\omega t+\phi)} \tag{2.3}$$

where F_0 and ϕ are the load magnitude and phase angle.

Evaluating the first and second derivatives of equation 2.2 and substituting them along with equation 2.3 into equation 2.1 yields:

$$\left(-m\omega^2 + ic\omega + k_s\right)X_0 e^{i\omega t} = F_o e^{i(\omega t+\phi)} \tag{2.4}$$

Let

$$\overline{X} = X_0 e^{-i\phi} \tag{2.5}$$

then

$$\frac{F_0}{\overline{X}} = \frac{F_0}{X_0} e^{i\phi} = (k_s - m\omega^2 + ic\omega) \tag{2.6}$$

Equation 2.6 can be written in the general form

$$\frac{F_0}{\overline{X}} = \frac{F_0}{X_0} e^{i\phi} = k' + ik'' \tag{2.7}$$

where $k^{'}$ and $k^{''}$ are the real and imaginary parts of the equation, which are known as the storage and loss stiffnesses respectively.

Equation 2.7 is the vector form of the dynamic stiffness of a system. The magnitude of the dynamic stiffness k_d is defined as:

$$k_d = \frac{F_0}{X_0} \tag{2.8}$$

For a spring mass system, it is

$$k_d = \sqrt{\left(k_s - m\omega^2\right)^2 + \left(c\omega\right)^2} \tag{2.9}$$

The phase between the load F and displacement X is called loss angle, which is

$$\phi = \tan^{-1}\left(\frac{k^{''}}{k^{'}}\right) \tag{2.10}$$

For a spring mass system:

$$\tan\phi = \frac{c\omega}{k_s - m\omega^2} \tag{2.11}$$

Damping Coefficient

If one rewriting equation 2.4 as:

$$k_s - m\omega^2 + ic\omega = k_d(\cos\phi + i\sin\phi) \tag{2.12}$$

and equating the factors of the imaginary parts in both sides of equation 2.12, the damping coefficient becomes

$$c = \frac{k_d \sin\phi}{\omega} \tag{2.13}$$

Rubber Model

Traditionally, the rubber is modeled by Voigt as shown in Figure 2.2. In such a model, the resultant force F_t by the displacement input x is

$$F_t = k_s x + c\dot{x} \tag{2.14}$$

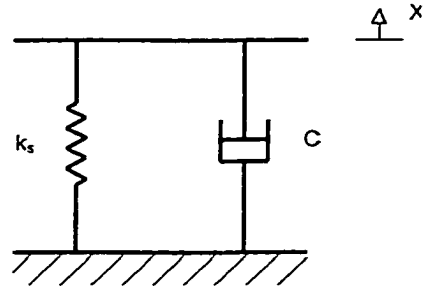

Figure 2.2. Voigt Model

Assuming

$$x = X_0 e^{i\omega t} \tag{2.15}$$

$$F_t = F_0 e^{i(\omega t+\phi)} \tag{2.16}$$

where X_0 and F_0 are the displacement and force amplitude, and ϕ is the loss angle. Defining the displacement as:

$$\overline{X}_0 = X_0 e^{-i\phi} \tag{2.17}$$

the vector form of the dynamic stiffness is obtained as

$$k_d = \frac{F_0}{\overline{X}_0} = k_s + ic\omega \tag{2.18}$$

Therefore, the magnitude of the dynamic stiffness k_d for the rubber is:

$$k_d = \sqrt{k_s^2 + (c\omega)^2} \tag{2.19}$$

and the loss angle is

$$\phi = \tan^{-1}\left(\frac{c\omega}{k_s}\right) \tag{2.20}$$

The plots of the measured dynamic stiffness and phase angle as function of frequency for a rubber component for various displacement amplitudes are shown in Figures 2.3 and 2.4, whose amplitudes are specified by the term called peak to peak displacement (*p/p*). The peak to peak displacement is in fact twice the displacement amplitude. The plots show that rubber dynamic properties are displacement amplitude dependent, such that the higher is the displacement amplitude, the lower the dynamic stiffness. However, the relative changes of the dynamic properties are not significant, hence rubber is treated as displacement amplitude independent in this research. The cusp at 18 Hz may be caused by the test fixture, which does not represent the rubber properties.

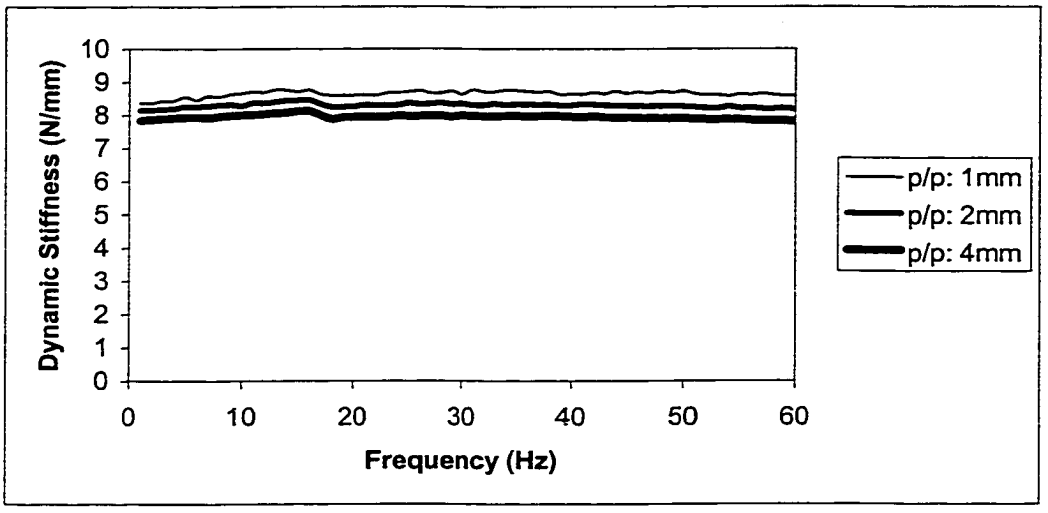

Figure 2.3. Dynamic Stiffness of a Rubber Component for Various Displacement Amplitudes

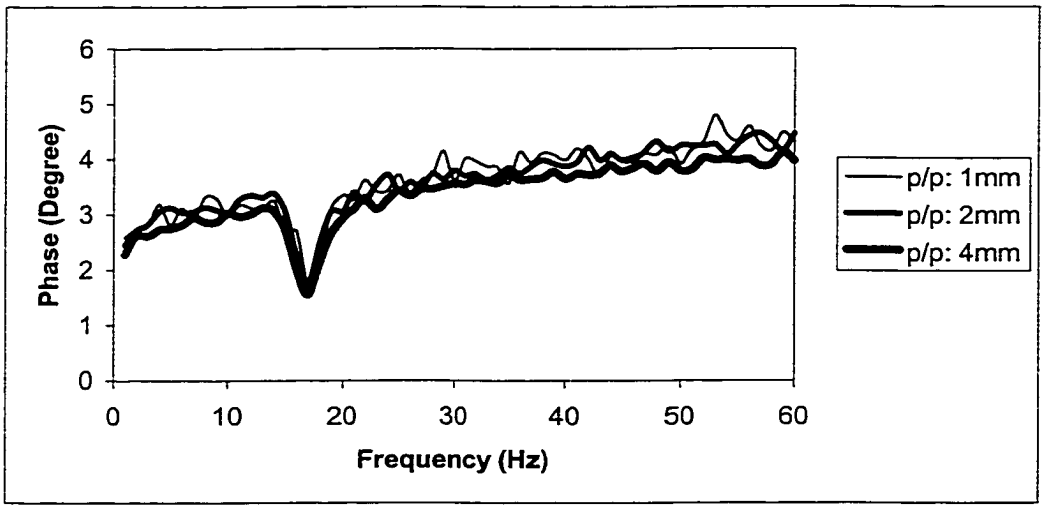

Figure 2.4. Phase Angle of a Rubber Component for Various Displacement Amplitudes

Experimental Study of Rubber Dynamic Properties

The rubber static stiffness, k_s, is predictable through commercially available software such as ABAQUS, but there are still three other unknown properties in equations 2.19 and 2.20. Since no theory is available to obtain those three unknowns, experiment is employed in this research to find the phase angle.

MTS Tester

The test machine used in the experimental study is MTS 831 dynamic tester (see Figure 2.5). A compressive preload is applied to the test specimen through the hydraulic actuator. The actuator is excited with a sinusoidal stroke x,

$$x = X_0 \sin \omega t \tag{2.21}$$

The load cell in the bottom of the MTS machine records the load magnitude and the phase lag (loss angle). The dynamic properties are then obtained through the data conversion program in the test machine.

The frequency range of the tests for the rubber specimen in this research is 0-20 Hz, which is well enough to capture the rubber dynamic characteristics. Because the tunable frequency range of the hydromount dynamic properties is smaller than 40 Hz, it is customized to test the hydromounts up to 40 Hz.

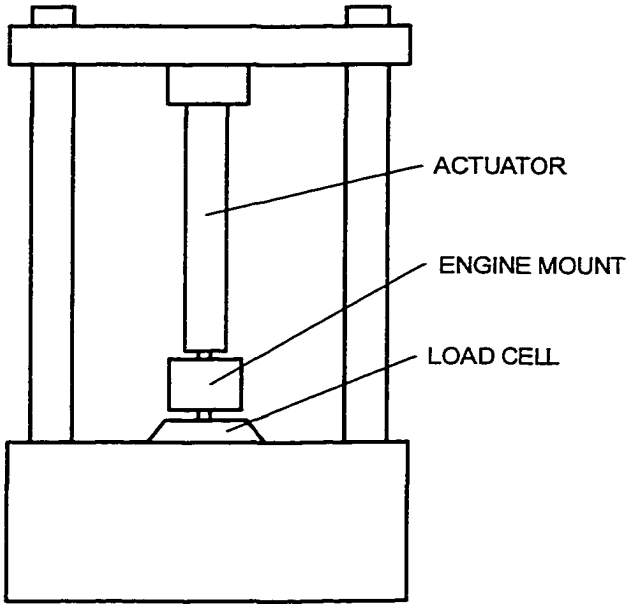

Figure 2.5. MTS Dynamic Tester

Test Specimen

By the fact that numerous tests have been conducted through the course of product development work and those tested data are readily available in the lab of Cooper-Standard Automotive at Auburn Indiana, only one specimen was specially designed for the present study as shown in Figure 2.6. It is a circular button with an outer diameter of 38 mm, an inner diameter of 12.7 mm and a height of 19 mm. Three pieces each of Duro 40, 50, 60, and 70 natural rubber were made.

Duro is short for durometer, which is commonly referred to as the Shore durometer after its original maker. Different Shore durometers are designed to cover the

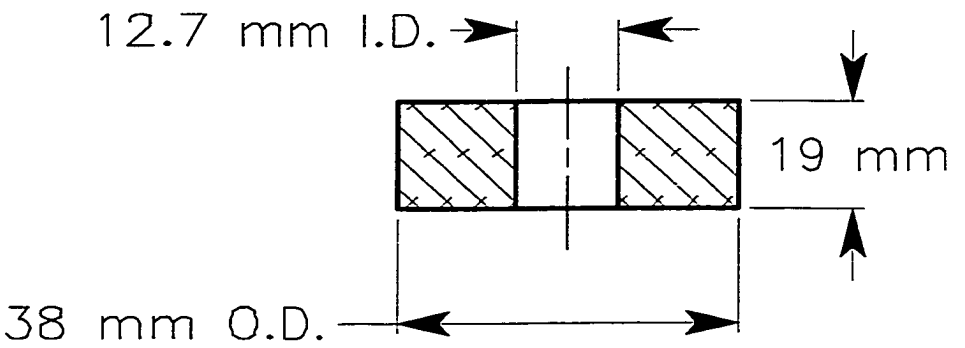

Figure 2.6. Button Specimen Layout

wide range of hardness encountered in rubbers, but Shore A scale, which scales from 0-100 from softest to the hardest, is the most appropriate for rubber compounds commonly used in engineering. Rubber compounds commonly used in engine mount application is in the range of 40 –70 Shore A (Duro 40-70).

Rubber Dynamic Properties for Various Hardnesses

The variation of the measured dynamic stiffness versus frequency for the button specimens with Duro 40, 50, 60 and 70 natural rubbers is shown in Figure 2.7. It shows that the dynamic stiffness is almost constant with the frequency, but it increases with the increase of the rubber hardness.

The variation of the measured damping coefficient versus frequency for the button specimens with Duro 40, 50, 60 and 70 natural rubbers is shown in Figure 2.8. It shows that damping coefficient is highly nonlinear with frequency, and it increases with the increase of the rubber hardness.

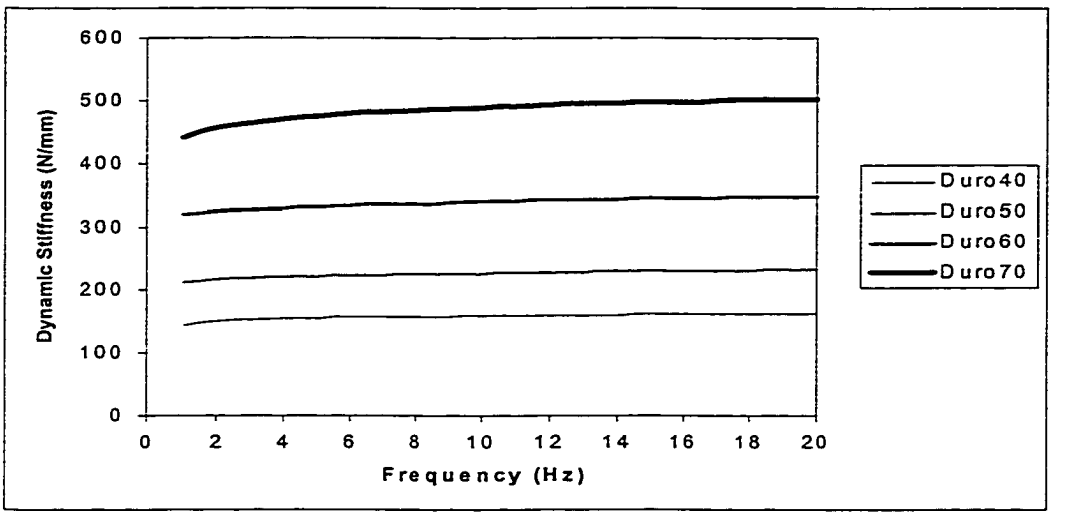

Figure 2.7. Dynamic Stiffness of Button Specimen for Various Hardness Compounds

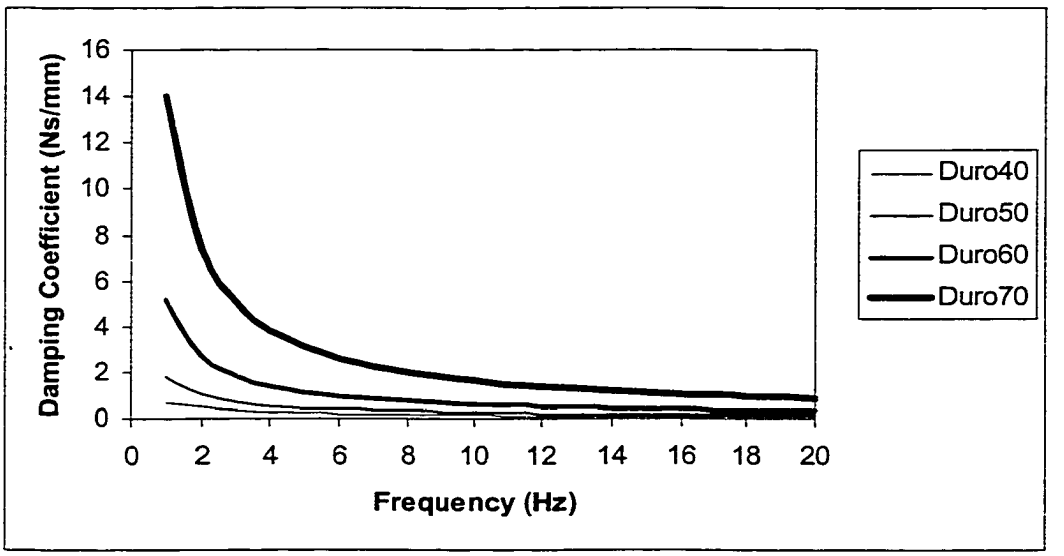

Figure 2.8. Damping Coefficient of Button Specimen for Various Hardness Compounds

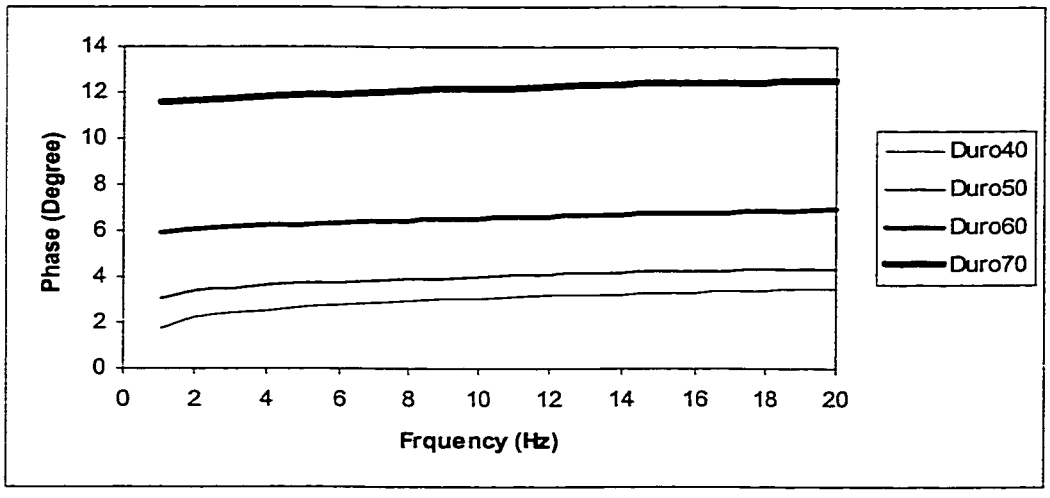

Figure 2.9. Phase Angle of Button Specimen for Various Hardness Compounds

The variation of the measured phase angle versus frequency for the button specimens with Duro 40, 50, 60 and 70 natural rubbers is shown in Figure 2.9. It shows that the phase angle is almost constant with frequency, but it increases with the increase of the rubber hardness.

Rubber Dynamic Properties for Various Geometries

Three sets of data are compared in order to understand the effect of geometry on the rubber dynamic properties: one from the test specimen shown in Figure 2.6, which is designated as specimen 1 for all tests in this section, and two others randomly collected from the lab database. The randomly selected specimens, specimens 2 and 3, are those with various sized bushings, strut mounts and engine mounts. If a bushing and an engine mount are chosen as specimens 2 and 3 for one test, then different products are chosen as specimen 2 and specimen 3 for another test. Therefore, in total, eight different Cooper

products (A to G) are used in the comparison of dynamic properties of the rubber for Duro 40, 50, 60 and 70 in this research (see Table 2.1 for clarity). In fact, that no product at Cooper is identical in geometry, therefore, all eight Cooper products chosen for dynamic property comparison have eight various geometries.

The variation of the dynamic stiffness versus frequency for three various specimens with Duro 40 rubber is shown in Figure 2.10. It shows that three specimens have three different dynamic stiffnesses, which indicates that dynamic stiffness is geometry dependent.

Table 2.1

Experimental Design of Test Specimens for Various Geometries

	Duro 40	Duro 50	Duro 60	Duro 70
Specimen 1	Button Specimen (Figure 2.6)	Button Specimen (Figure 2.6)	Button Specimen (Figure 2.6)	Button Specimen (Figure 2.6)
Specimen 2	Cooper Product A	Cooper Product C	Cooper Product E	Cooper Product G
Specimen 3	Cooper Product B	Cooper Product D	Cooper Product F	Cooper Product H

The variation of the damping coefficient versus frequency for three various specimens with Duro 40 rubber is shown in Figure 2.11. It shows that the damping coefficient is a geometry dependent parameter.

The variation of phase angle versus frequency for three various specimens with Duro 40 rubber is shown in Figure 2.12. It shows that the phase angle changes slightly with geometry. The change is so small that it can be treated as relatively geometry independent.

Sounds good in Figure 2.11 that the damping coefficients of specimens 2 and 3 are quite close. In addition to the almost constant phase angles for all three specimens

(Figure 2.12), the dynamic stiffnesses of specimen 2 and 3 are close according to Figure 2.10, therefore, the damping coefficients for Specimens 2 and 3 should be close according to equation 2.13.

The same conclusions are drawn from the Duro 50, 60 and 70 rubber test data, whose plots are shown in Figures 2.13 to 2.21.

Conclusions

It is concluded from the above experiment that:

Dynamic stiffness is almost linear with frequency; it is geometry dependent;

Damping coefficient is highly nonlinear with frequency, it is geometry dependent as well;

Phase angle is approximately geometry independent.

Phase Angles of Rubber Compounds

In the previous section it was concluded that the phase angle of a rubber component varies within a relatively small range for various geometries. This small phase variation makes very little difference in the rubber dynamic property calculations so it is reasonable to treat the phase angle as constant. These results that are averaged from three test specimens are shown in Table 2.2.

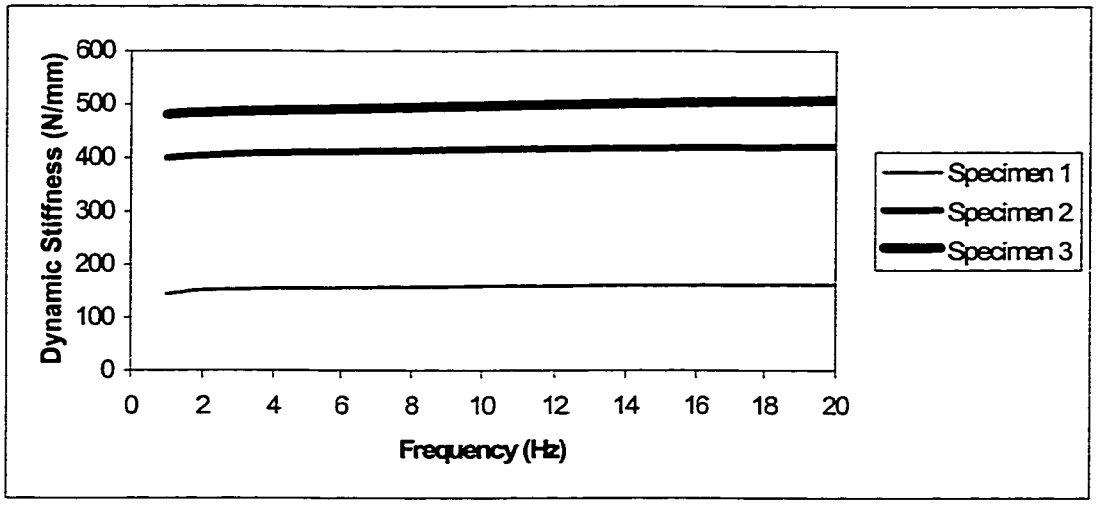

Figure 2.10. Dynamic Stiffness of Duro 40 Specimens for Various Geometries

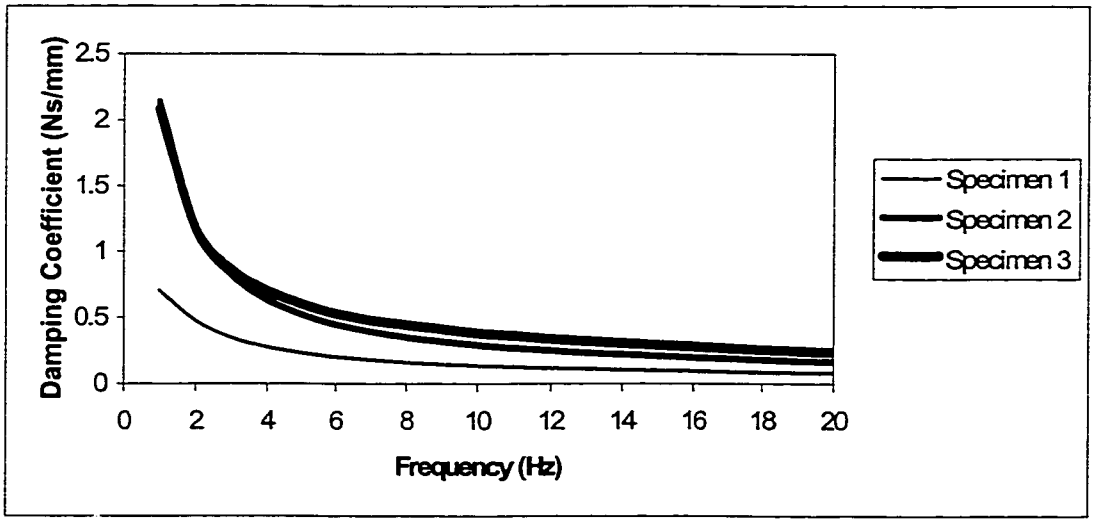

Figure 2.11. Damping Coefficient of Duro 40 Specimens for Various Geometries

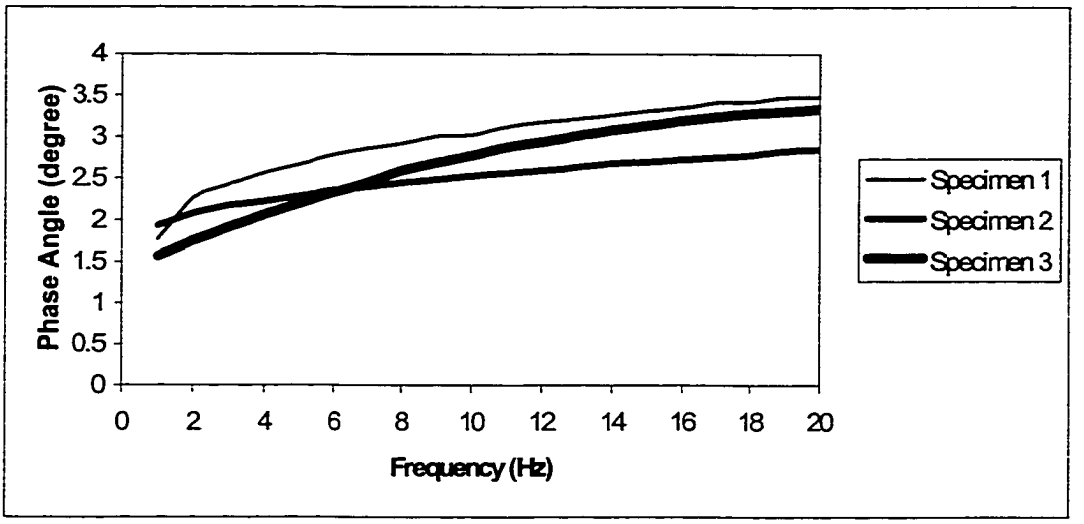

Figure 2.12. Phase Angle of Duro 40 Specimens for Various Geometries

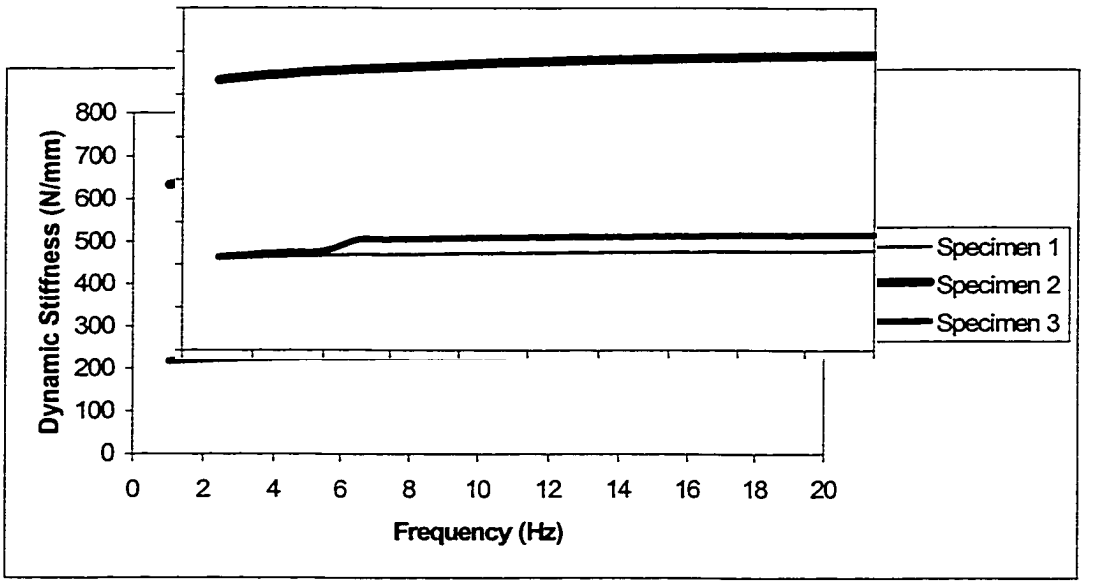

Figure 2.13. Dynamic Stiffness of Duro 50 Specimens for Various Geometries

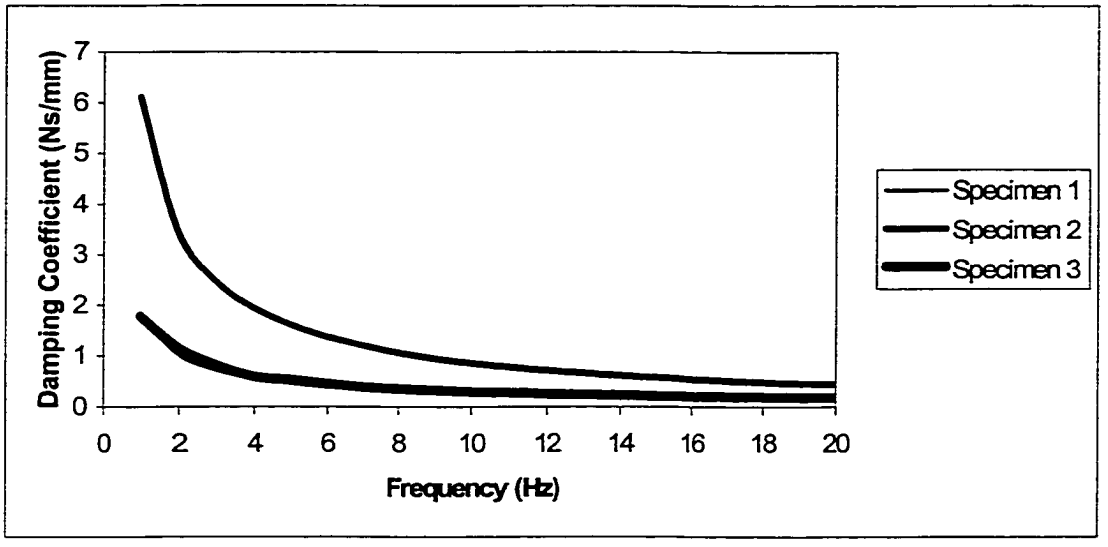

Figure 2.14. Damping Coefficient of Duro 50 Specimens for Various Geometries

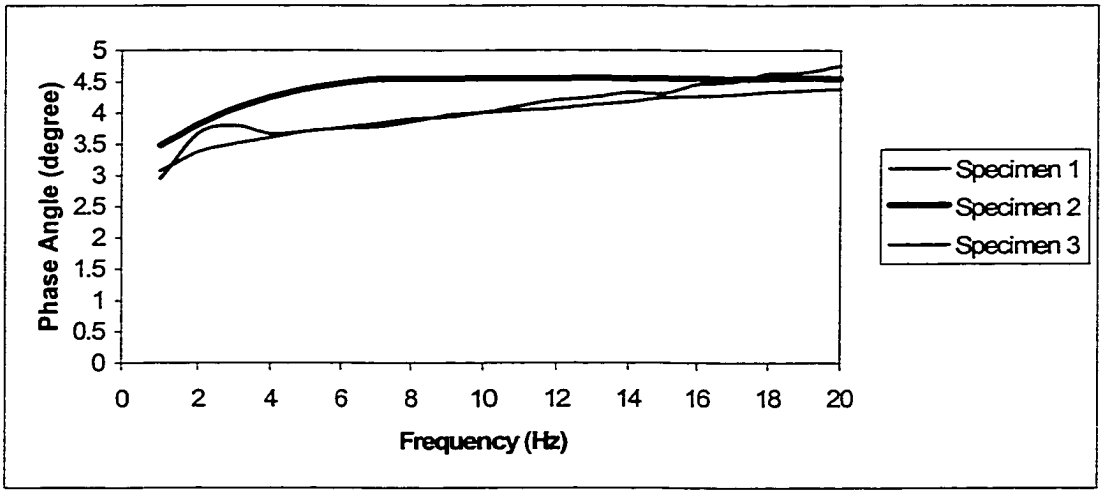

Figure 2.15. Phase Angle of Duro 50 Specimens for Various Geometries

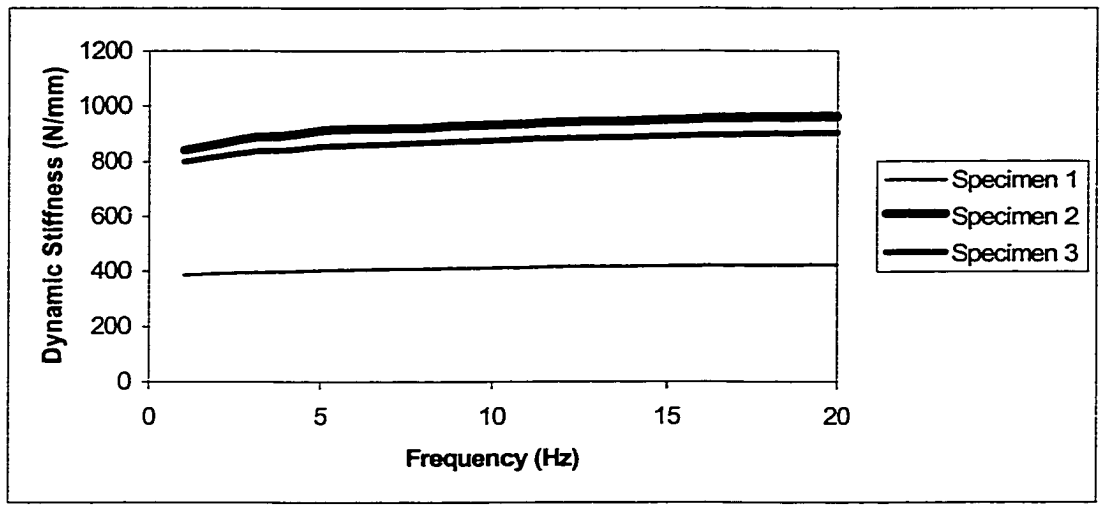

Figure 2.16. Dynamic Stiffness of Duro 60 Specimens for Various Geometries

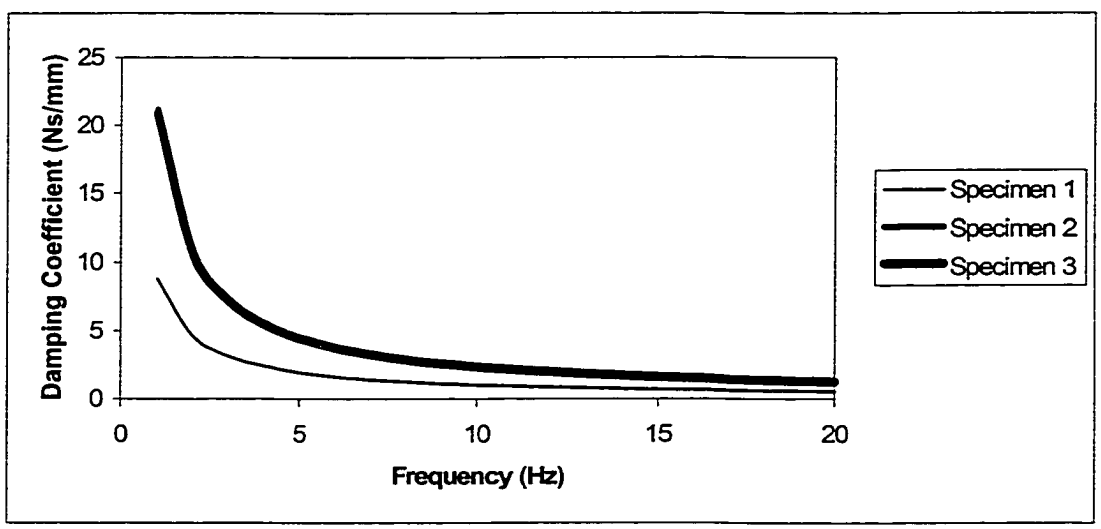

Figure 2.17. Damping Coefficient of Duro 60 Specimens for Various Geometries

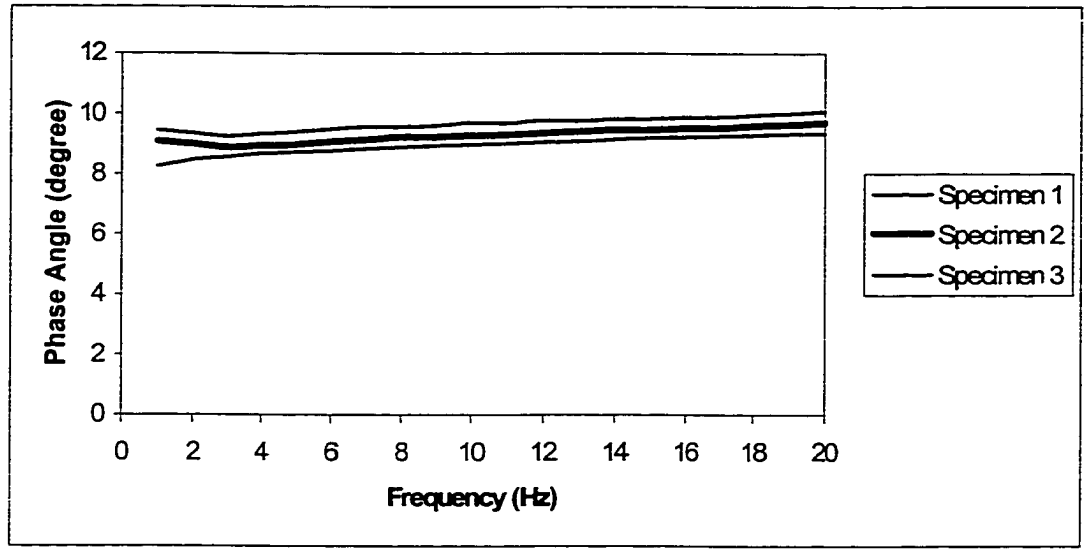

Figure 2.18. Phase Angle of Duro 60 Specimens for Various Geometries

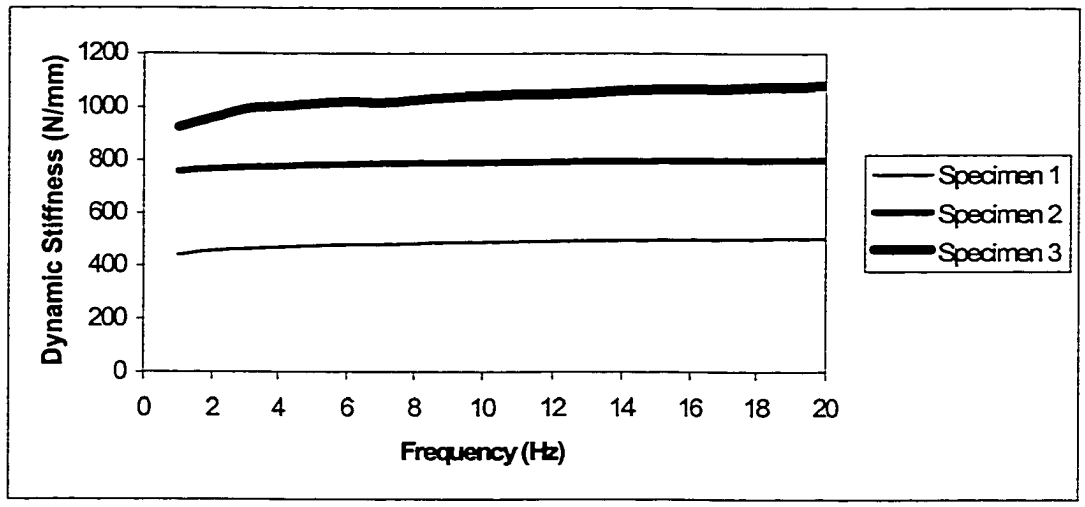

Figure 2.19. Dynamic Stiffness of Duro 70 Specimens for Various Geometries

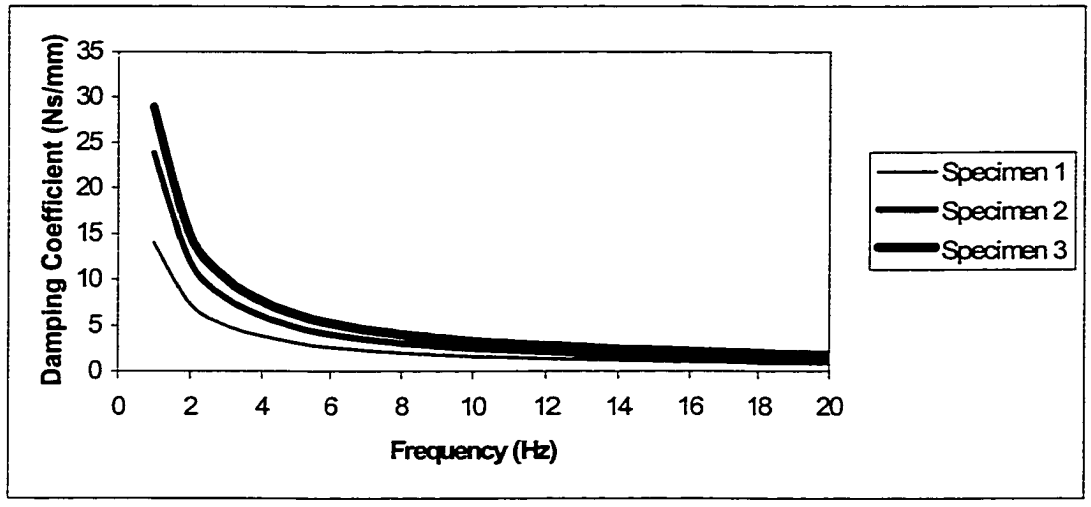

Figure 2.20. Damping Coefficient of Duro 70 Specimens for Various Geometries

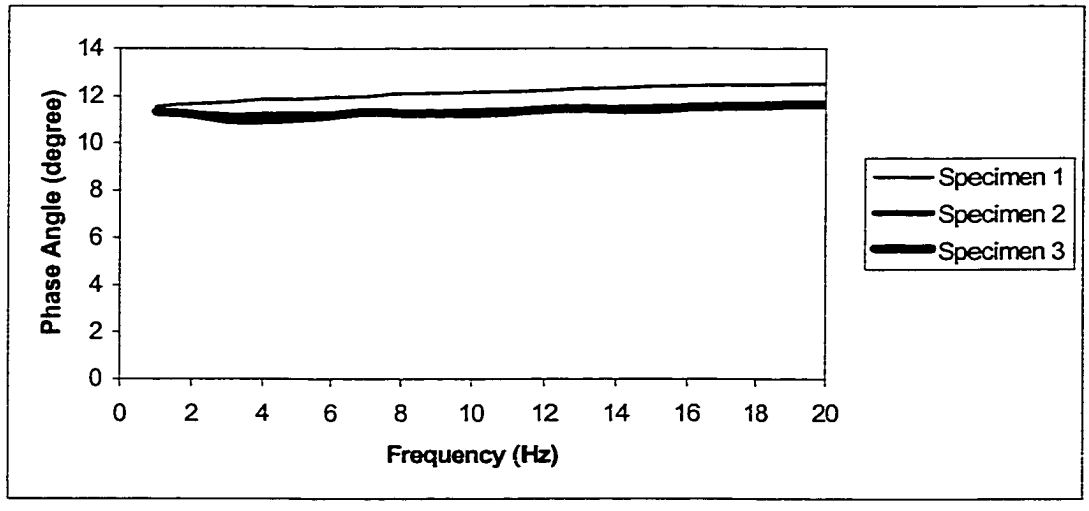

Figure 2.21. Phase Angle of Duro 70 Specimens for Various Geometries

Table 2.2

Average Phase Angles Corresponding to Rubber Hardness

Hardness (shore A)	40	50	60	70
Phase Angle (degree)	2.71	4.14	9.30	11.63

Calculation of Dynamic Stiffness

Seen earlier that the dynamic stiffness of rubber is a function of the static stiffness k_s and damping coefficient c (equation 2.19). The damping coefficient c, however, can be calculated by using equation 2.10 and the phase angles listed in Table 2.2 through

$$c = \frac{k_s \tan\phi}{\omega} \tag{2.22}$$

Then, the dynamic stiffness becomes

$$k_d = \sqrt{k_s^2 + (c\omega)^2} = \sqrt{k_s^2 + k_s^2 \tan^2\phi} = \frac{k_s}{\cos\phi} \tag{2.23}$$

To verify the theory, a comparison of the measured and calculated dynamic stiffness versus frequency for Duro 70 rubber is illustrated in Figure 2.22. It is seen that equation 2.23 is an approximation which is acceptable for practical applications.

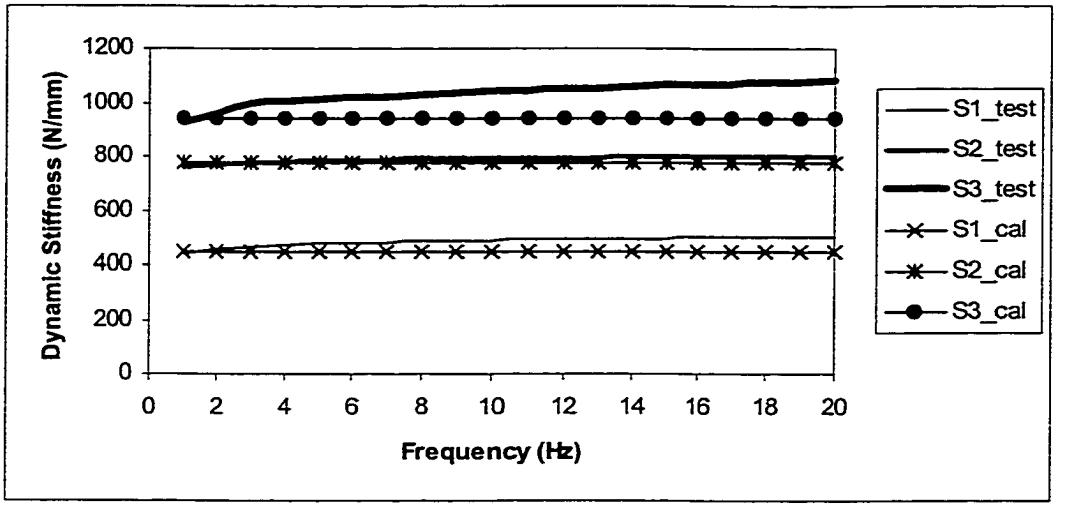

Figure 2.22. Comparison of Measured and Calculated Dynamic Stiffness for Duro 70 Rubber Specimens

Calculation of Damping Coefficient

The damping coefficient can be calculated by using equation 2.10 after knowing the dynamic stiffness. To verify the theory, the comparison between the measured and calculated damping coefficient for Duro 70 rubber is shown in Figure 2.23. It shows an excellent match between the calculated and measured results.

Calculation of Transmissibility

In the dynamic test setup a compressive preload is applied, which is considered as an equivalent mass (see Figure 2.24). Therefore, transmissibility can be expressed by (Thomson, 1988)

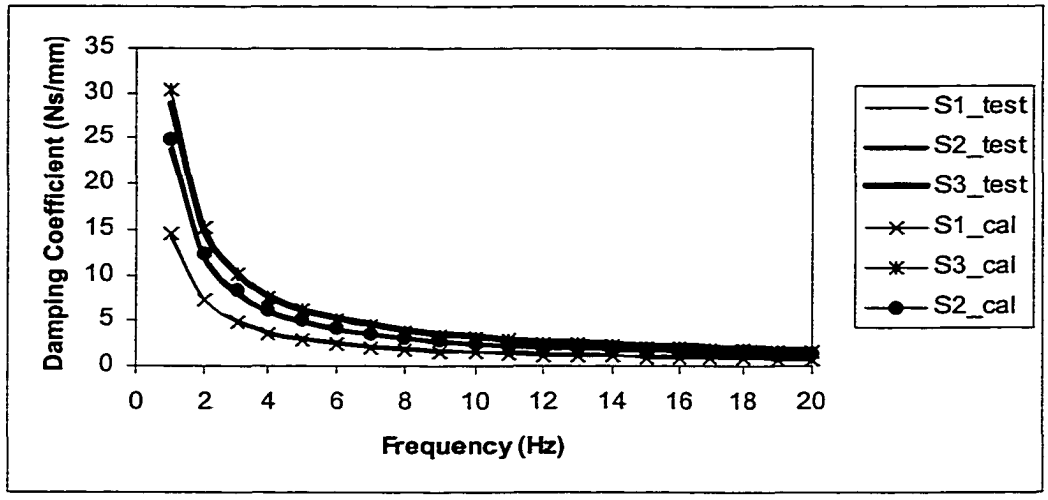

Figure 2.23. Comparison of Measured and Calculated Damping Coefficient for Duro 70 Rubber Specimens

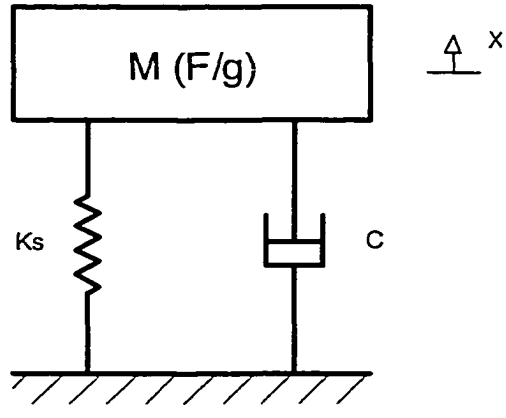

Figure 2.24. Voigt Model with Equivalent Mass

$$TR = \left|\frac{F_T}{F_0}\right| = \sqrt{\frac{k_s{}^2 + (c\omega)^2}{\left(k_s - m\omega^2\right)^2 + (c\omega)^2}} \tag{2.24}$$

Figure 2.25 presents a comparison of the measured and calculated transmissibility for Duro 40 rubber. It shows that they agree well.

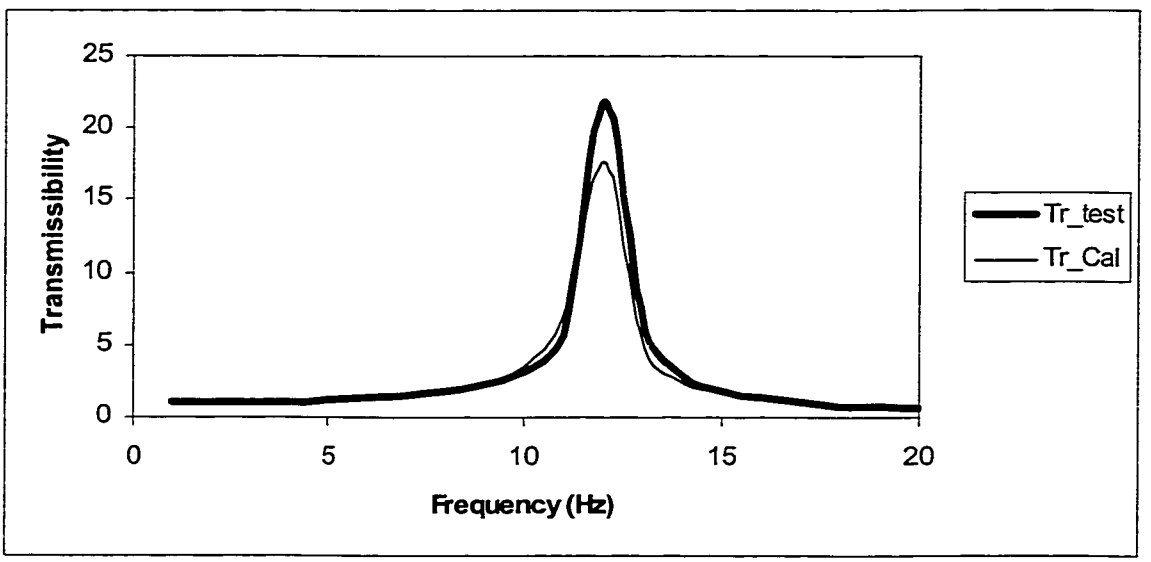

Figure 2.25. Comparison of Measured and Calculated Transmissibility for a Rubber Component

Summary

The dynamic stiffness of a system is defined as the ratio of the load amplitude to the displacement amplitude. The loss angle is defined as the phase difference between the load and displacement. Experimental studies of rubber dynamic properties indicated that the dynamic stiffness and damping coefficient of rubber are geometry dependent, but the loss angle can be treated as geometry independent parameter. Using the tested phase

angle, the dynamic stiffness, damping coefficient and transmissibility of a rubber specimen can be predicted theoretically, by employing a procedure shown in Figure 2.26.

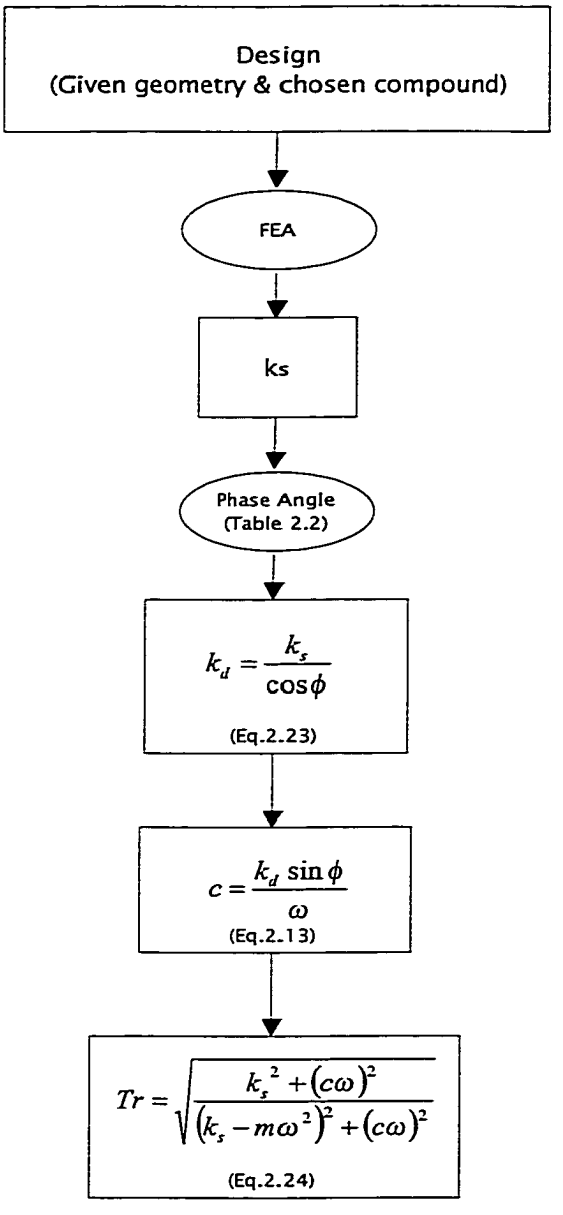

Figure 2.26. Rubber Dynamic Property Prediction Procedure Flow Chart

CHAPTER III

HYDROMOUNT MODEL WITH LUMPED INERTIA TRACK DAMPING COEFFICIENT

In this chapter a mathematical model of the hydromount with the lumped fluid damping coefficient will be proposed. The equations of the hydromount dynamic stiffness and loss angle are developed. The phenomena of the hydromount locking mechanism, the frequency at the maximum loss angle, and the stiffness dip are investigated. At the end of this chapter, a hybrid hydromount, hydrobushing, is introduced.

Mathematical Model

A hydromount is composed of a main rubber element and a damping generating mechanism, called the inertia track. It is essential to have a good hydromount model in order to understand its mechanism. The proposed hydromount model in this research is shown in Figure 3.1. It is comprised of an inner metal, an outer metal, two fluid chambers with pressure difference p, and an inertia track with cross-sectional area a and length l. The rubber section is modeled as a static stiffness k_s and damping C_r. When the inner metal is subjected to a sinusoidal displacement input X, the fluid (density ρ) in the chambers is pumped by an equivalent piston (area A), and it flows back and forth through the inertia track (x is the fluid displacement in the inertia track) while the rubber bulges because of the fluid pressure.

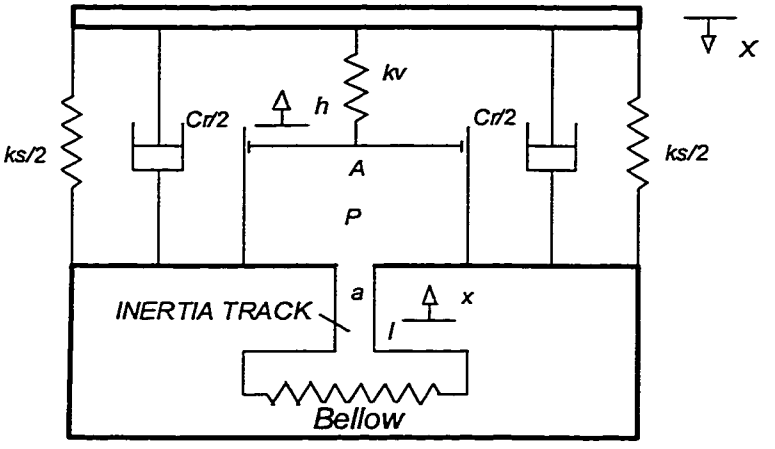

Figure 3.1. Hydromount Model

The Mount Displacement X

The hydromount is subjected to a compressive preload resulting from the powertrain static weight. Assuming an oscillating dynamic load is applied over this preload, such a load is simulated by a sinusoidal displacement X in its dynamic characteristic testing given by

$$X = X_0 e^{i\omega t} \tag{3.1}$$

where X_0 is the displacement amplitude, and it is often associated with peak to peak displacement (X_0 equals to half of the peak to peak displacement).

Static Stiffness k_s

The static stiffness k_s in the hydromount model is defined as the stiffness at zero exciting frequency, or the stiffness under the mount displacement X_0.

This stiffness is equivalent to the rubber static stiffness because there is no resistance of the fluid transformation from the top to the lower chamber under this displacement input. Prediction of rubber stiffness is achievable through commercially available software such as ABAQUS.

Rubber Damping Coefficient C_r

An in-depth investigation of the rubber damping coefficient was conducted in Chapter II. It was concluded that the damping coefficient C_r can be evaluated approximately by the measured loss angle, which is a rubber hardness dependent parameter, and the stiffness, which is a geometry dependent parameter expressed by equation 2.13.

Volumetric Stiffness k_v

When the hydromount is compressed, the rubber element deforms. It also bulges because of the internal fluid pressure. The stiffness caused by the rubber bulge effect is called volumetric stiffness.

At high frequencies the inertia track of the hydromount is locked, due to a mechanism which will be studied later. As a result, the stiffness of the hydromount at high frequencies is the sum of the static stiffness and the volumetric stiffness. This makes it possible to predict the volumetric stiffness theoretically. To illustrate the volumetric stiffness prediction using finite element method, an axisymmetric model of a hydromount is modeled as shown in Figure 3.2. The metal elements (Young's modulus: 210 GPa; Poisson's ratio: 0.3) represent the steel stud, which connects the mount to the engine. A

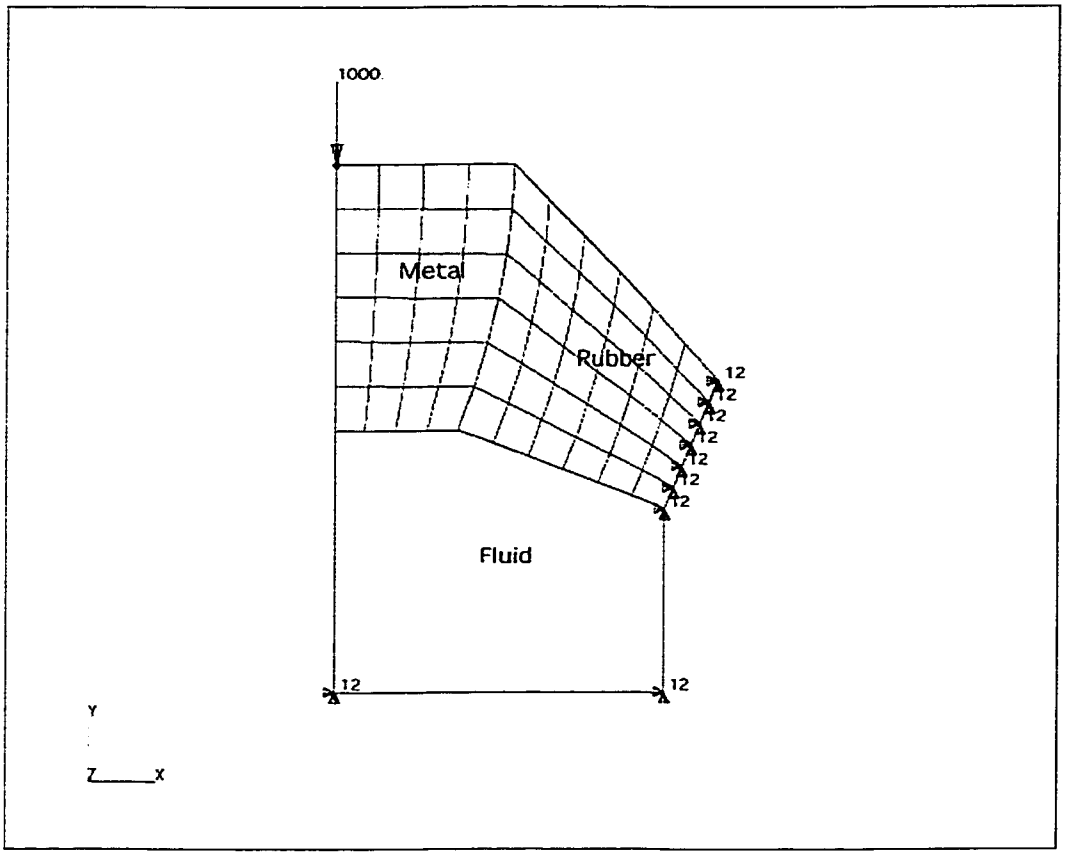

Figure 3.2. An Axisymmetric Model of a Hydromount

1000 N load is applied at the center node of the top stud. A Duro 50 natural rubber is used for the conical shaped main rubber element, and Mooney-Rilvin rubber model (Mooney, 1940) is employed

$$W = C_{10}(I_1 - 3) + C_{01}(I_2 - 3) \tag{3.2}$$

where W is the strain energy, and I_1 and I_2 are the principal invariants of the strain tensor. Table 3.1 lists the Mooney coefficients for the various hardness natural rubbers Cooper-Standard Automotive is using. The method used to obtain those coefficients is described in detail by Charlton and Yang (1993) or by Finney and Humar (1988). The fluid at the

Table 3.1

Mooney Coefficients for Various Hardness Compounds

Hardness	C_{10} (MPa)	C_{01} (MPa)
40	0.195	0.0162
50	0.2969	0.0584
60	0.4947	0.0639
70	0.7691	0.0199

top chamber has a density of 1000 kg/m^3. The translational degrees of freedom for the lower outer side of the rubber elements are set to zero. It is assumed that the inertia track locks at high frequencies, and the chamber volume is therefore set to remain constant, whereas the rubber elements bulge because of the pressurized fluid caused by the applied load at the top of the metal stud. This finite element model is solved by ABAQUS with two different cases: one with the fluid element deactivated, which simulates the hydromount at zero frequency, and the other with activated fluid elements which simulates the "locked" hydromount at high frequencies. Figure 3.3 shows the load versus deflection curves for the finite element models with and without fluid element activated. It is seen that the stiffness from the FEA model without the fluid element activated is 164 N/mm, which is the static stiffness of the hydromount k_s. The stiffness with fluid element activated is 504 N/mm, which is the sum of the static stiffness and volumetric stiffness. Therefore, the volumetric stiffness k_v is 340 N/mm.

The magnitude of the volumetric stiffness predicted by using this method is usually higher than the measured result because of the fluid "leak" (a small amount of fluid passing through the inertia track at high frequencies). But the finite element model assumes that the inertia track is perfectly locked, which means there is no fluid passing

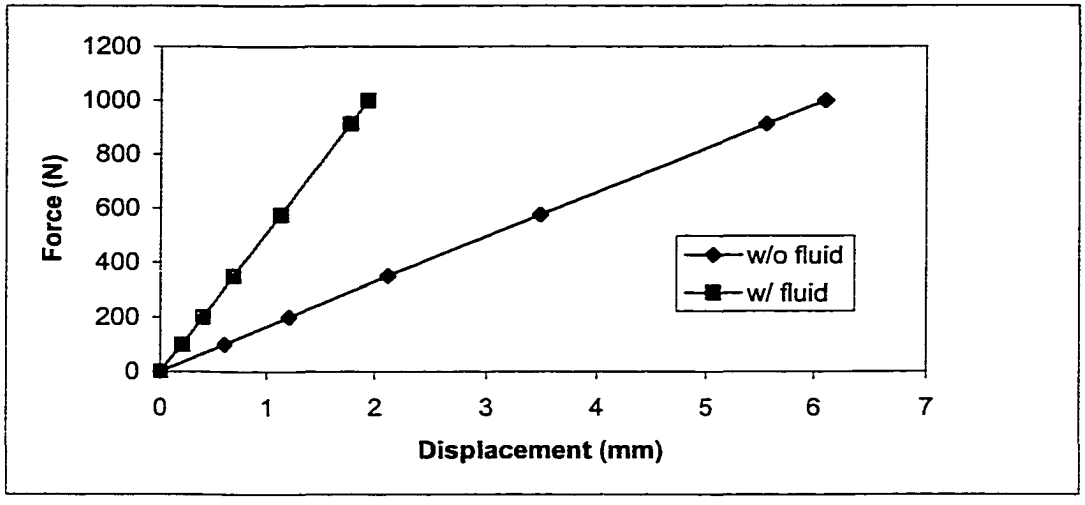

Figure 3.3. Load Deflection Curves

through the inertia track at high frequencies. Therefore, a correlation factor, which ranges around 0.7~0.8 based on experience, is applied.

Another important issue is that the volumetric stiffness is displacement amplitude dependent. Intuitively, the higher amplitude of the mount displacement forces more fluid "leaks" through the inertia track, which would result in a softer volumetric stiffness. Indeed, a test proves this phenomenon (Figure 3.4). Because of this displacement amplitude dependence, the accurate prediction of the volumetric stiffness becomes more difficult, which deserves further research in the future.

The Piston Parameters

Under sinusoidal displacement input at the top of the mount, the volumetric stiffness resulting from the bulged rubber pushes the fluid through the inertia track, which functions similar to a piston. The parameters to describe this piston are the equivalent piston displacement h and equivalent piston area A. The value of h is

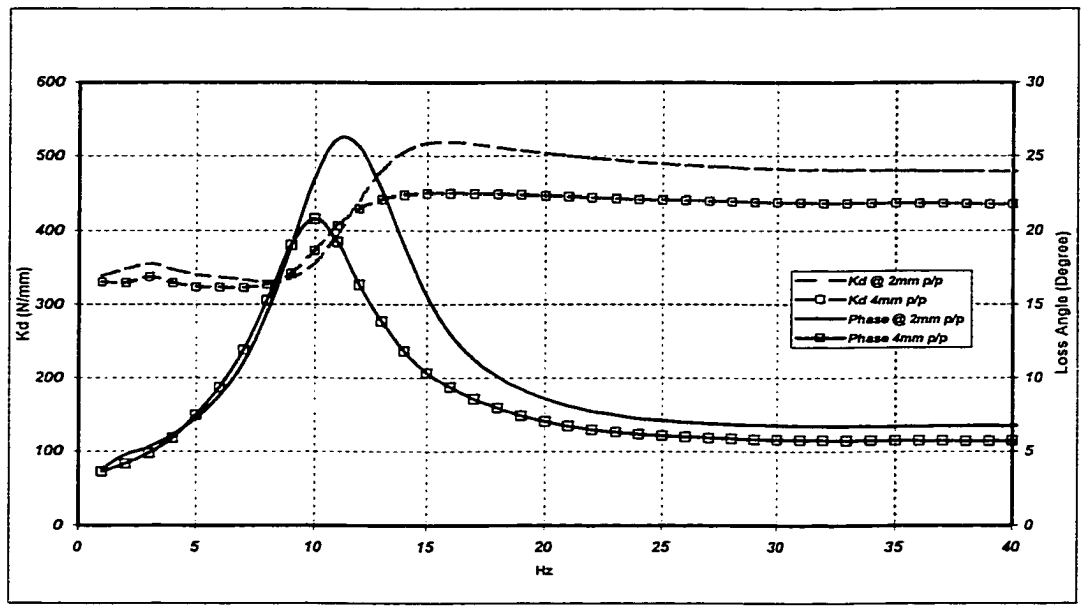

Figure 3.4. Amplitude Effect on Volumetric Stiffness

complicated and will be discussed separately later. The equivalent piston area is the projected area of the chamber, since the pressure of the fluid is perpendicular to the surface (see Figure 3.5).

Quite often a travel limit mechanism, which controls the maximum travel of the mount, is installed in the upper chamber as shown in Figure 3.6. Because of this travel limit, the fluid pumping efficiency declines, which results in a smaller equivalent piston area. If η is denoted as the effectiveness factor, then the equivalent piston area of the hydromount with travel limit in its upper chamber is

$$A_{eq} = \eta A \tag{3.3}$$

where $\eta<1$ is determined experimentally.

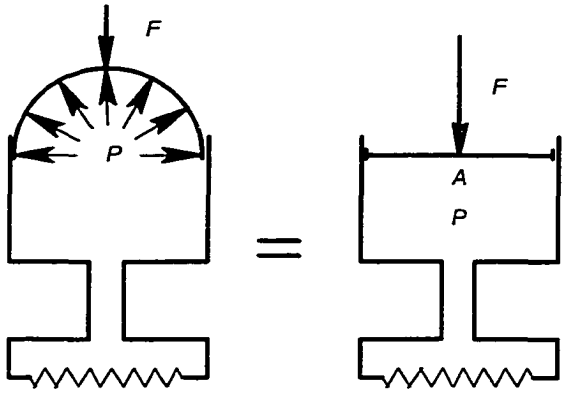

Figure 3.5. Illustration of Equivalent Piston Area

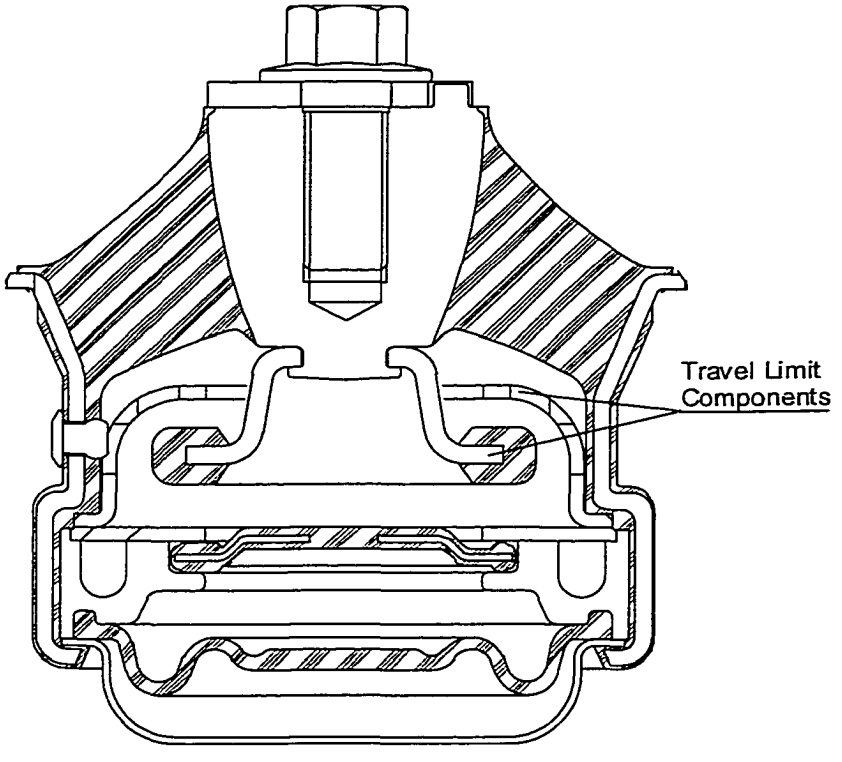

Figure 3.6. Schematic of Travel Limit

Inertia Track Fluid Displacement, Fluid Pressure and Other Parameters

The sinusoidal mount displacement X generates the fluid pressure in the chambers which results in the fluid pumping action back and forth through the inertia track. The displaced fluid in the inertia track is denoted as x. The fluid pressure difference between the top and bottom chambers is denoted as P.

The other parameters in the hydromount model are the fluid properties (density ρ and viscosity) and the inertia track geometrical parameters (length l and the cross-sectional area a).

A Physical Hydromount

A physical hydromount with the following parameters is used throughout the entire research:

$$k_s = 180 \text{ kN/m};$$

$$k_v = 230 \text{ kN/m};$$

$$C_I = 0.4 \text{ Ns/m};$$

$$l = 0.2 \text{ m};$$

$$a = 5 \times 10^{-5} \text{ m}^2;$$

$$A = 3.15 \times 10^{-3} \text{ m}^2;$$

$$\rho = 1000 \text{ kg/m}^3.$$

where C_I value is an estimate at this point and will be studied later in Chapter V.

Figure 3.7 shows the measured dynamic stiffness and loss angle versus frequency from MTS dynamic tester for this hydromount. The test method, procedure and setup are described by Kim (1991), Graf (1987) and Geisberger (1999) in detail. At zero frequency, this hydromount has stiffness 180 KN/mm, which is the rubber static stiffness. The maximum loss angle (62 degrees) occurs at a frequency of 9 Hz.

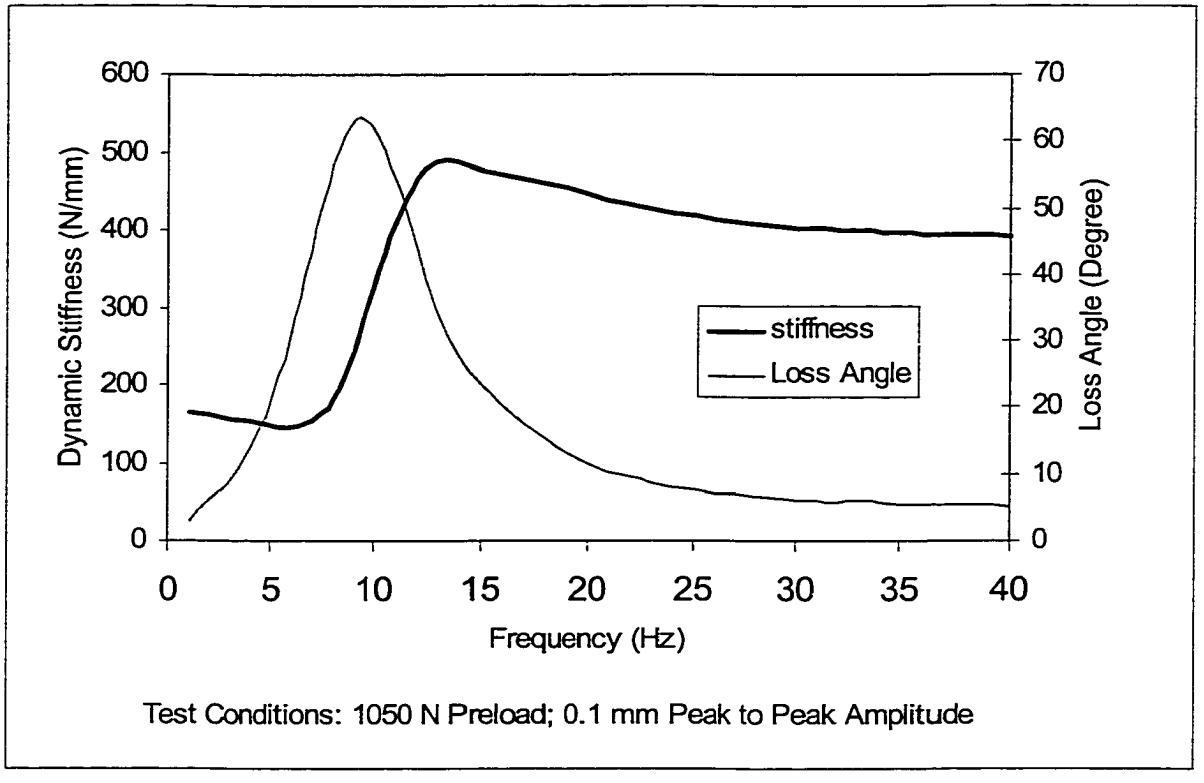

Figure 3.7. The Measured Dynamic Characteristics of the Hydromount

Fundamental Equations

For the hydromount model shown in Figure 3.1, the equation of motion of the inertia track fluid is expressed by

$$la\rho\frac{d^2x}{dt^2}+C_I\frac{dx}{dt}=pa \tag{3.4}$$

The volume conservation equation is

$$hA=xa \tag{3.5}$$

The equivalent piston balance equation based on the assumption that the flow is incompressible is

$$k_v(X-h)=pA \tag{3.6}$$

Assuming that the stiffness k_s is linear over the operating range and the damping C_r is viscous, then the resultant force F on the outer metal is

$$F=k_sX+C_r\frac{dX}{dt}+pA \tag{3.7}$$

Equations 3.4-3.7 are the fundamental equations needed in developing the hydromount dynamic properties.

Inertia Track Fluid Resonant Frequency

Substituting h from equation 3.5 into equation 3.6, the pressure difference becomes

$$p = \frac{k_v}{A}\left(X - \frac{xa}{A}\right) \tag{3.8}$$

Substituting equation 3.8 into equation 3.4 gives

$$la\rho\frac{d^2x}{dt^2} + C_I\frac{dx}{dt} + k_v\left(\frac{a}{A}\right)^2 x = k_v\left(\frac{a}{A}\right)X \tag{3.9}$$

The above equation is the system differential equation of the fluid in the inertia track. Therefore, the resulting resonant frequency of the fluid is

$$\omega_n = \frac{a}{A}\sqrt{\frac{k_v}{la\rho}} \tag{3.10}$$

For the physical hydromount with the parameters given earlier, the calculated inertia track resonant frequency based on equation 3.10 is 12.12 Hz.

If the effectiveness factor of the equivalent piston area η for the hydromount with travel limit is considered (see equation 3.3), equation 3.10 becomes

$$\omega_n = \frac{a}{\eta A}\sqrt{\frac{k_v}{la\rho}} \tag{3.11}$$

Therefore, the frequency test of a hydromount can be used to determine η.

Fluid Displacement in Inertia Track

The solution of equation 3.9 gives

$$x = \frac{k_v\left(\frac{a}{A}\right)X}{\left[k_v\left(\frac{a}{A}\right)^2 - la\rho\omega^2\right] + iC_I\omega} \tag{3.12}$$

Let x be

$$x = x_0 e^{i(\omega t + \phi_x)} \tag{3.13}$$

where ϕ_x is the phase difference between x and X.

Then,

$$x_0 e^{i\phi_x} = \left\{ \frac{k_v\left(\frac{a}{A}\right)^2 - la\rho\omega^2}{\left[k_v\left(\frac{a}{A}\right)^2 - la\rho\omega^2\right]^2 + (C_I\omega)^2} - \frac{iC_I\omega}{\left[k_v\left(\frac{a}{A}\right)^2 - la\rho\omega^2\right]^2 + (C_I\omega)^2} \right\} \left[k_v\left(\frac{a}{A}\right)X_0\right] \tag{3.14}$$

Hence

$$x_0 = \frac{k_v\left(\frac{a}{A}\right)X_0}{\sqrt{\left[k_v\left(\frac{a}{A}\right)^2 - la\rho\omega^2\right]^2 + (C_I\omega)^2}} \tag{3.15}$$

and phase angle ϕ_x is

$$\phi_x = \arctan\left(-\frac{C_f\omega}{k_v\left(\frac{a}{A}\right)^2 - la\rho\omega^2}\right) \tag{3.16}$$

The variation of the fluid displacement and the phase angle versus frequency is shown in Figures 3.8 and 3.9. It is seen that x_0/X_0 peaks at the resonant frequency of the inertia track (12.12 Hz). At this resonant frequency, there is a phase shift from –90° to 90°.

Equivalent Piston Displacement h

Substituting equation 3.12 into equation 3.5, the equivalent piston displacement h becomes

$$h = \frac{k_v\left(\frac{a}{A}\right)^2 X}{\left[k_v\left(\frac{a}{A}\right)^2 - la\rho\omega^2\right] + iC_f\omega} \tag{3.17}$$

Let h be

$$h = h_0 e^{i(\omega t + \phi_h)} \tag{3.18}$$

where ϕ_h is the phase difference between h and X.

Then,

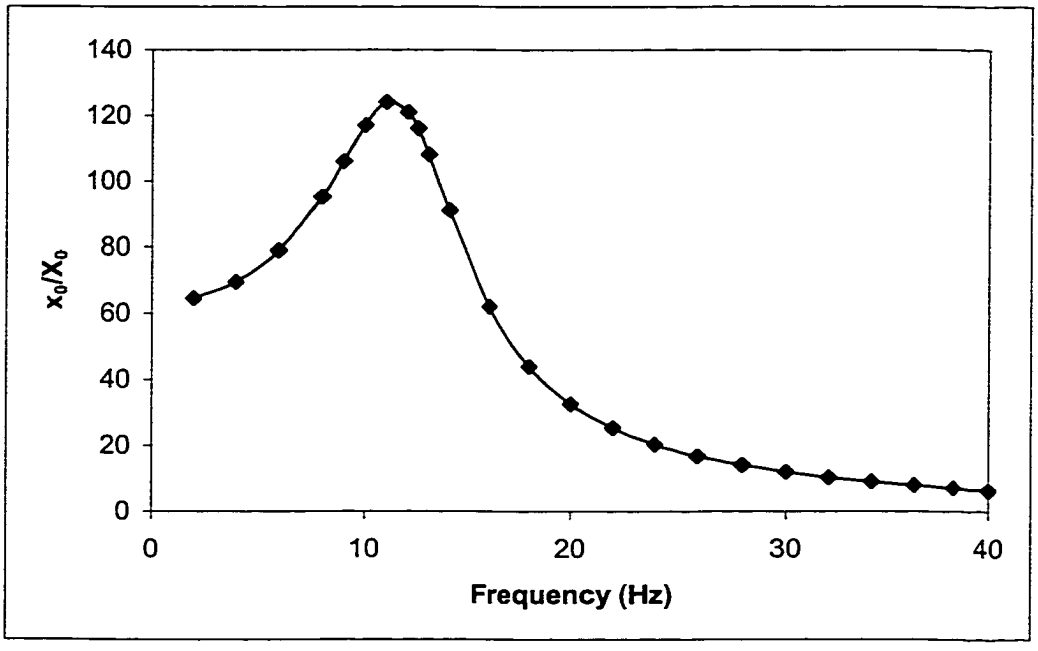

Figure 3.8. Plot of x_0/X_0 Versus Frequency

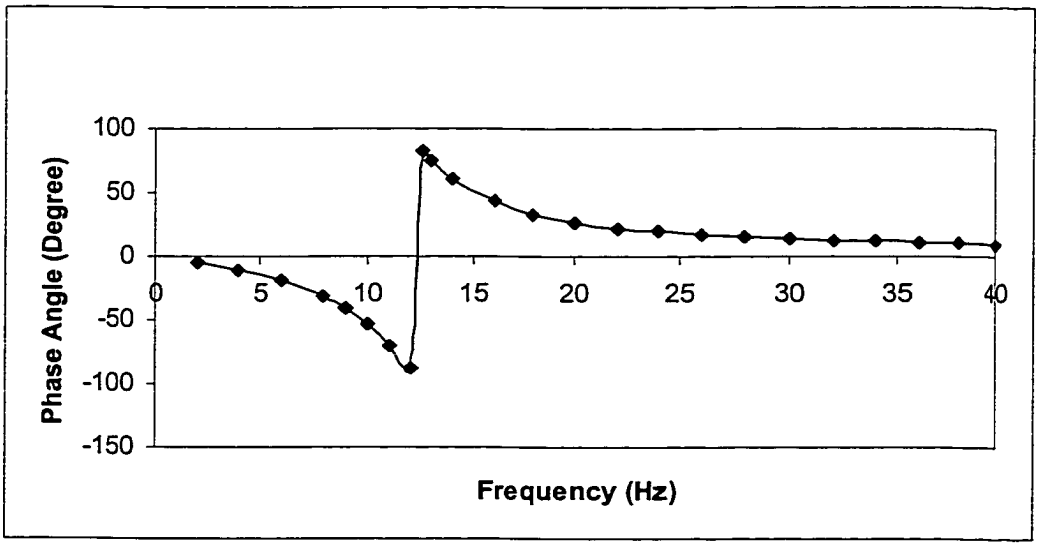

Figure 3.9. Phase Angle Between x and X Versus Frequency

$$h_0 e^{i\phi_x} = \left\{ \frac{k_v\left(\frac{a}{A}\right)^2 - la\rho\omega^2}{\left[k_v\left(\frac{a}{A}\right)^2 - la\rho\omega^2\right]^2 + (C_l\omega)^2} - \frac{iC_l\omega}{\left[k_v\left(\frac{a}{A}\right)^2 - la\rho\omega^2\right]^2 + (C_l\omega)^2} \right\} \left[k_v\left(\frac{a}{A}\right)^2 X_0 \right] \quad (3.19)$$

Hence

$$h_0 = \frac{k_v\left(\frac{a}{A}\right)^2 X_0}{\sqrt{\left[k_v\left(\frac{a}{A}\right)^2 - la\rho\omega^2\right]^2 + (C_l\omega)^2}} \quad (3.20)$$

and the phase angle ϕ_h is

$$\phi_h = \arctan\left(-\frac{C_l\omega}{k_v\left(\frac{a}{A}\right)^2 - la\rho\omega^2} \right) \quad (3.21)$$

It is seen that

$$\phi_x = \phi_h \quad (3.22)$$

which means x and h are in phase.

Figure 3.10 presents a plot of h_0/X_0 versus frequency for the physical hydromount parameters given earlier. Again, h_0/X_0 peaks at the inertia track fluid resonant frequency.

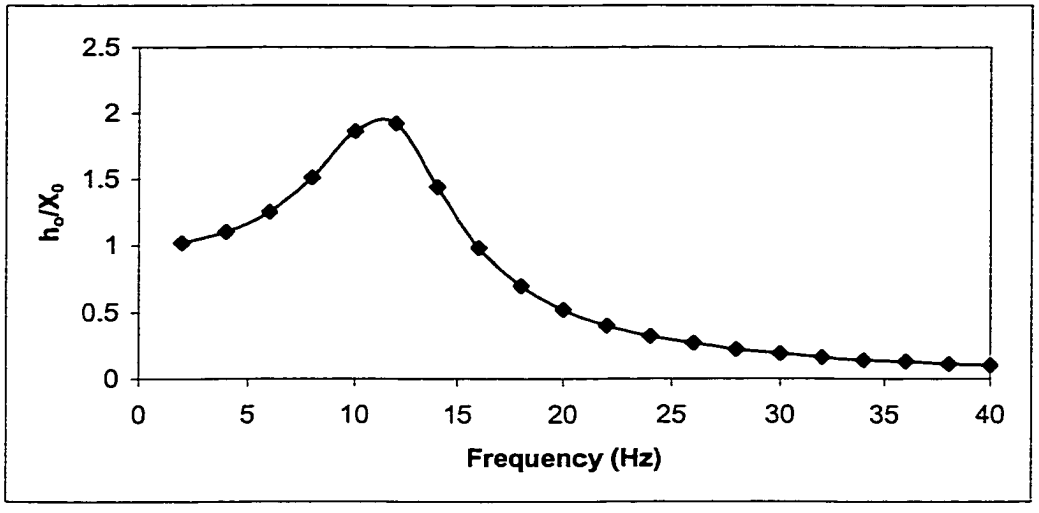

Figure 3.10. Plot of h_0/X_0 Versus Frequency

Fluid Pressure Difference

Substituting equation 3.12 into equation 3.8, the expression for the pressure difference p becomes

$$p = \left[\frac{k_v}{A} - \frac{k_v^2 \left(\frac{a^2}{A^3} \right)}{k_v \left(\frac{a}{A} \right)^2 - la\rho\omega^2 + iC_f\omega} \right] X_0 e^{i\omega t} \tag{3.23}$$

Let

$$P(\omega, X_0) = \left[\frac{k_v}{A} - \frac{k_v^2 \left(\frac{a^2}{A^3} \right)}{k_v \left(\frac{a}{A} \right)^2 - la\rho\omega^2 + iC_l\omega} \right] X_0 \tag{3.24}$$

Then

$$p = P(\omega, X_0) e^{i\omega t} \tag{3.25}$$

where $P(\omega,X_0)$ is the pressure amplitude.

It is seen that the fluid pressure is a function of the frequency. It also depends on the volumetric stiffness, mount displacement amplitude, equivalent piston area, fluid density, inertia track length, cross-sectional area and damping coefficient. The static stiffness does not affect the fluid pressure. Figure 3.11 presents a plot of the pressure versus frequency for the physical hydromount given earlier but with mount displacement amplitudes of 0.5, 1.0 and 1.5 mm. It is seen that the pressure difference increases with the increase of mount displacement amplitude.

Dynamic Stiffness and Loss Angle

Substituting equation 3.23 and the time derivative of equation 3.1 into equation 3.7, the complex form of the dynamic stiffness becomes

$$k_d = k_s + iC_r\omega + k_v - \frac{k_v^2 \left(\frac{a}{A} \right)^2}{k_v \left(\frac{a}{A} \right)^2 - la\rho\omega^2 + iC_l\omega} \tag{3.26}$$

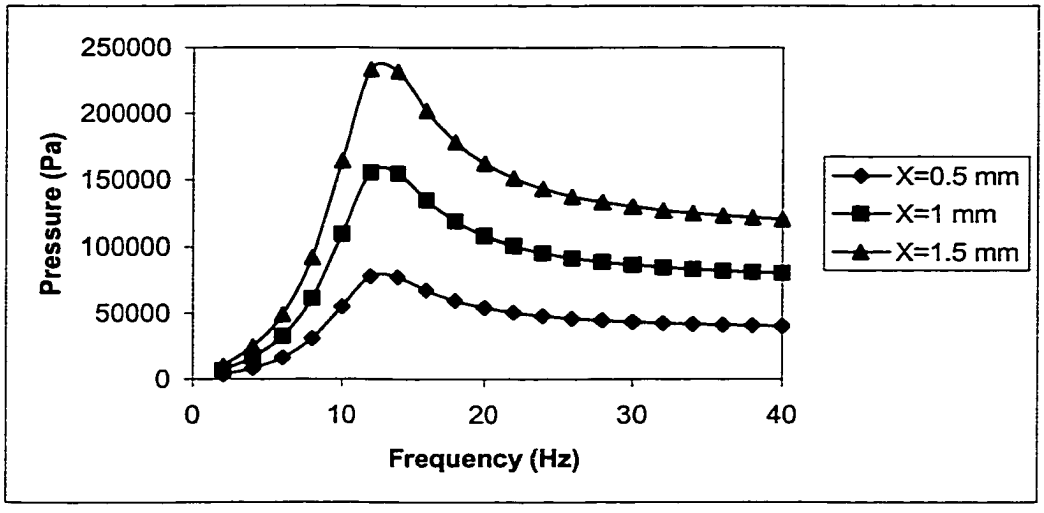

Figure 3.11. Pressure Difference of the Hydromount for Various Displacement Amplitudes

Using the terms of the storage and loss stiffnesses as defined by equation 2.7, then the storage stiffness k' is

$$k' = k_s + k_v - \frac{k_v^2\left(\frac{a}{A}\right)^2\left[k_v\left(\frac{a}{A}\right)^2 - la\rho\omega^2\right]}{\left[k_v\left(\frac{a}{A}\right)^2 - la\rho\omega^2\right]^2 + (C_l\omega)^2} \tag{3.27}$$

and the loss stiffness k'' is

$$k'' = \frac{k_v^2\left(\frac{a}{A}\right)^2 C_l\omega}{\left[k_v\left(\frac{a}{A}\right)^2 - la\rho\omega^2\right]^2 + (C_l\omega)^2} + C_r\omega \tag{3.28}$$

The loss angle ϕ can then be obtained by

$$\phi = \tan^{-1}(\frac{k''}{k'}) \tag{3.29}$$

Equation 3.29 indicates that the dynamic properties of a hydromount are related to the rubber static stiffness, rubber damping, rubber bulge affected stiffness (volumetric stiffness) and the oscillatory fluid effect.

Rubber Damping Effect on the Dynamic Properties

The contribution to the hydromount dynamic properties by the rubber damping C_r is indicated in the second term on the right side of equation 3.29. Its effect is negligible since $k_s + iC_r\omega$ is actually the dynamic stiffness of the rubber, which, as shown earlier, increases slowly over the frequency range (see Figure 1.2). The almost constant value of its dynamic stiffness indicates that the influence of the damping term is minimal. The numerical example given next proves this point.

Assuming that Duro 50 natural rubber is used, whose loss angle is 4.14 degrees (see Table 2.2), for the physical hydromount given earlier. Following the procedure described in Chapter II, the rubber damping coefficient C_r versus frequency curve is drawn as shown in Figure 3.12.

Using the parameters described, the hydromount dynamic properties both with and without rubber damping considered were calculated and plotted in Figure 3.13. It is shown that the dynamic properties are almost identical for both cases: with and without the rubber damping coefficient considered. It is concluded that the rubber damping has a very limited effect on the hydromount dynamic properties.

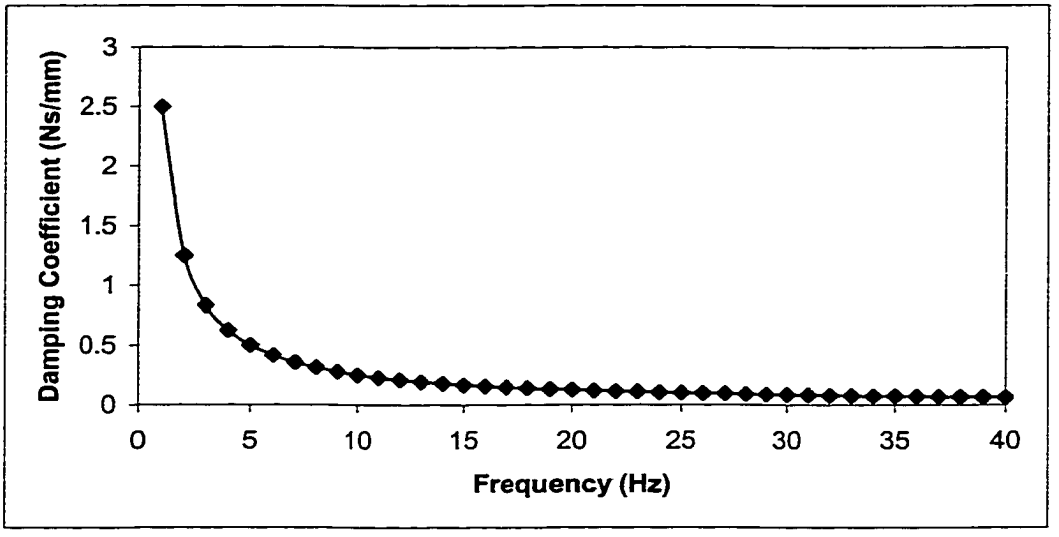

Figure 3.12. Rubber Damping Coefficient of the Hydromount

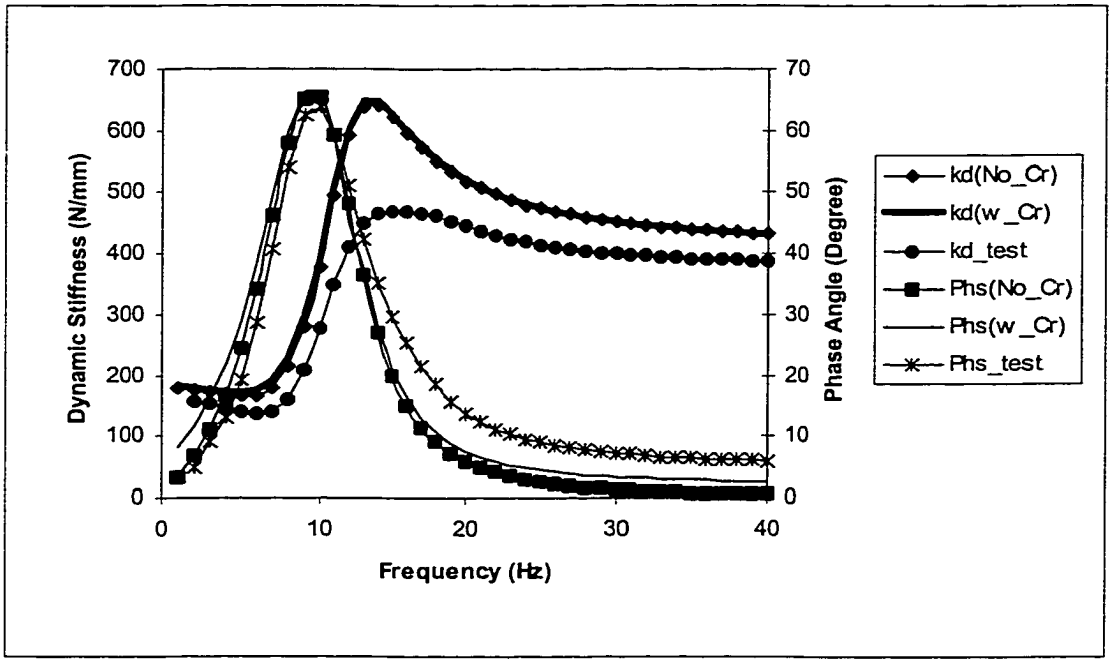

Figure 3.13. Comparison of Dynamic Properties of A Hydromount With and Without Rubber Damping Coefficient Considered

Hence equation 3.26 can be rewritten as:

$$k_d = k_s + k_v - \frac{k_v^2\left(\frac{a}{A}\right)^2}{k_v\left(\frac{a}{A}\right)^2 - la\rho\omega^2 + iC_l\omega} \tag{3.30}$$

For verification, the experimental dynamic stiffness and loss angle values were also plotted in Figure 3.13. It is evident that the calculated dynamic stiffness is higher than the tested value, especially the peak stiffness. The calculated and tested loss angles match well except for the higher frequency range, in which the tested loss angle is higher than the predicted. This comparison proves that the theory is reasonably valid based on the assumed inertia track damping coefficient.

Hydromount Damping Coefficient

With the known dynamic stiffness and loss angle from equations 3.26 and 3.29, the damping coefficient of the hydromount according to equation 2.10 is then

$$c = \frac{\sqrt{k'^2 + k''^2}\sin\phi}{\omega} \tag{3.31}$$

It is obvious that the damping coefficient of the hydromount c and the inertia track fluid damping coefficient C_I are two different concepts, where C_I is a component of c.

Figure 3.14 presents a plot of the hydromount damping coefficient versus frequency for the physical hydromount given earlier. Again the measured damping coefficient curve is also plotted for comparison. It shows that both the calculated and the

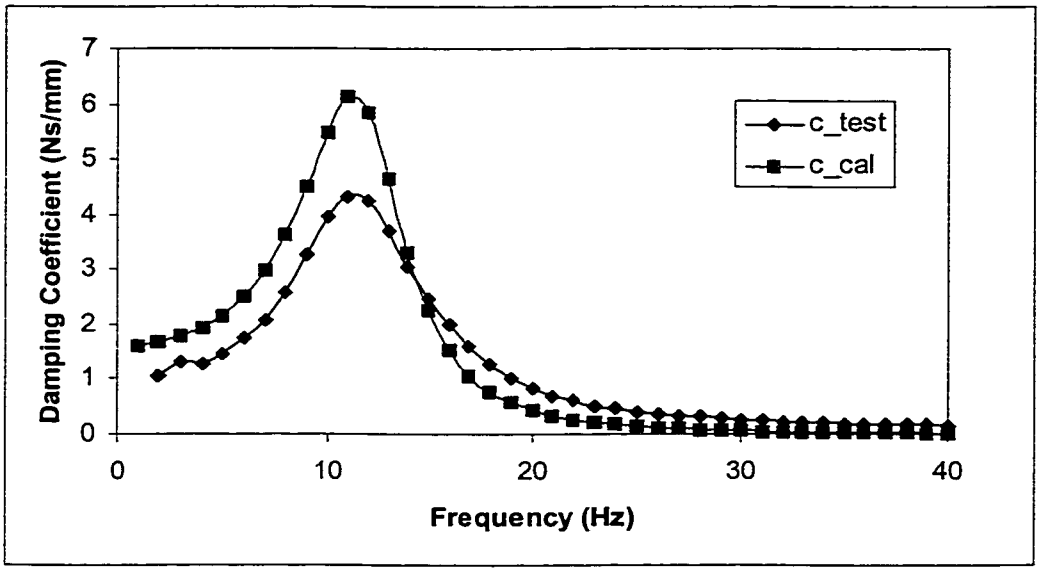

Figure 3.14. Damping Coefficient of the Hydromount

measured results peak at the same frequency, but the peak damping coefficient from the prediction is higher than the experimental values.

Parametric Study

Parameters such as the static stiffness, volumetric stiffness, inertia track length and its cross-sectional area and fluid density, affect the dynamic characteristics of a hydromount. Also, these parameters may be related to each other, such that the change of one parameter might inevitably bring in another parameter change. But it is assumed for simplicity that all the parameters are independent in this study.

Effect of Static Stiffness

It is obvious that an increase of the static stiffness k_s results in an increase of the dynamic stiffness k_d according to equation 3.30. Since the static stiffness does not affect the loss stiffness k'', it results in the decrease of the loss angle while increasing k_s. Figures 3.15 and 3.16 illustrate the changes in dynamic properties for various static stiffnesses. But the hydromount damping coefficient is independent of the static stiffness (see Figure 3.17).

Effect of Volumetric Stiffness

Figure 3.18 presents plots of the dynamic stiffness versus frequency for various volumetric stiffnesses. The peak dynamic stiffness increases with the increase of volumetric stiffness. Figure 3.19 presents plots of loss angle versus frequency for various volumetric stiffnesses. It is seen that the increased volumetric stiffness increases the peak loss angle. Figure 3.20 presents the damping coefficient versus frequency for various volumetric stiffnesses. An increase in volumetric stiffness increases the peak damping coefficient. Also the frequencies at the points of the maximum loss angle and maximum damping coefficient increase with the increase of the volumetric stiffness.

Effect of Equivalent Piston Area

Figure 3.21 presents plots of dynamic stiffness versus frequency for various equivalent piston areas. The peak dynamic stiffness decreases with the increase of the equivalent piston area. Figure 3.22 presents plots of loss angle versus frequency for various equivalent piston areas. The increased equivalent piston area reduces the peak

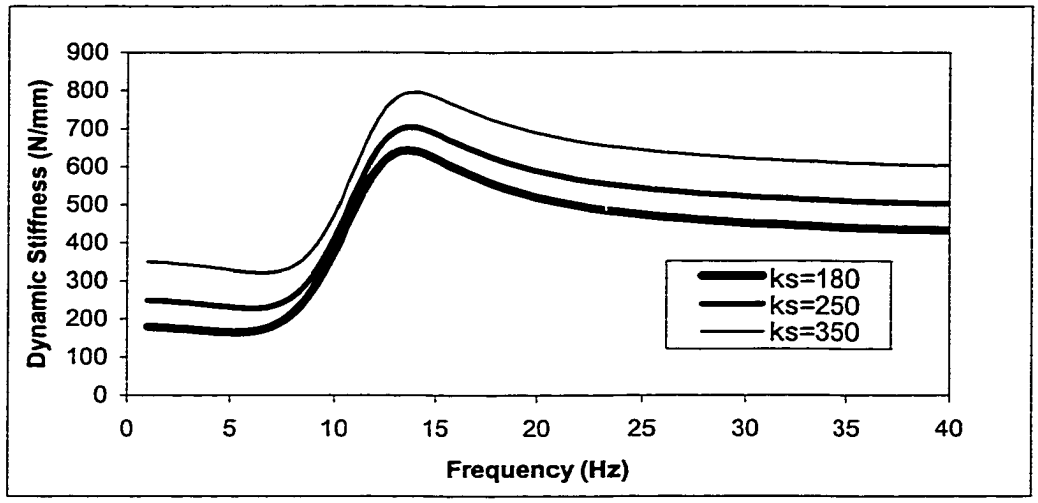

Figure 3.15. Dynamic Stiffness of the Hydromount for Various Static Stiffnesses

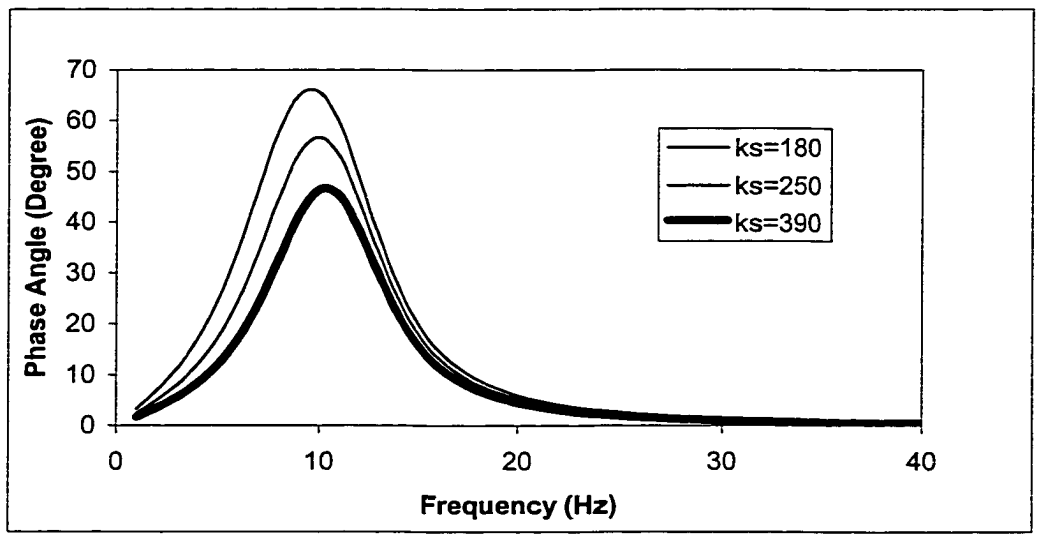

Figure 3.16. Phase Angle of the Hydromount for Various Static Stiffnesses

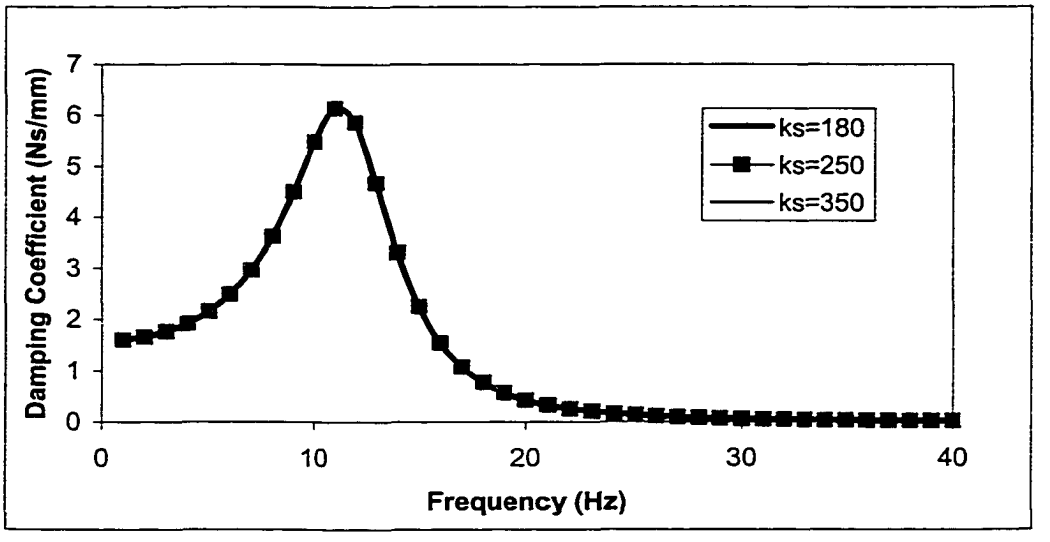

Figure 3.17. Damping Coefficient of the Hydromount for Various Static Stiffnesses

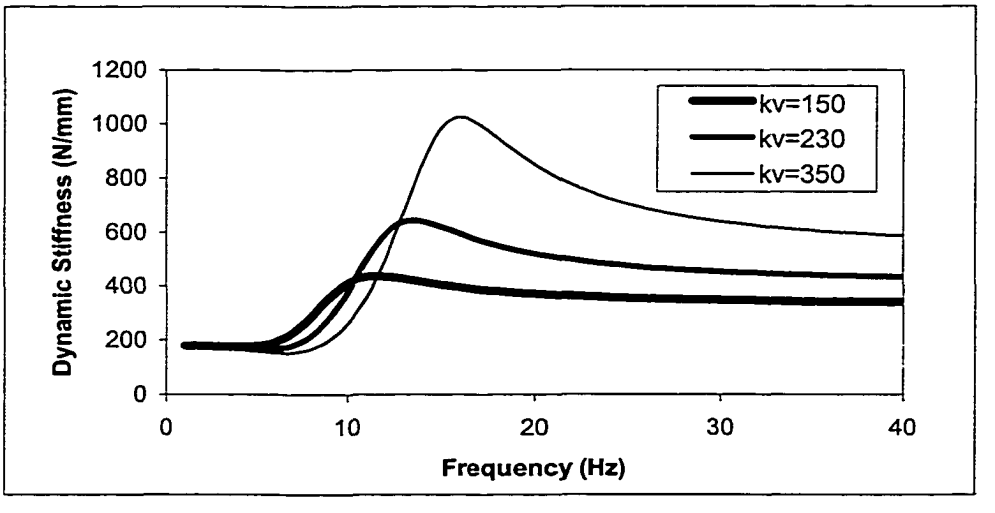

Figure 3.18. Dynamic Stiffness of the Hydromount for Various Volumetric Stiffnesses

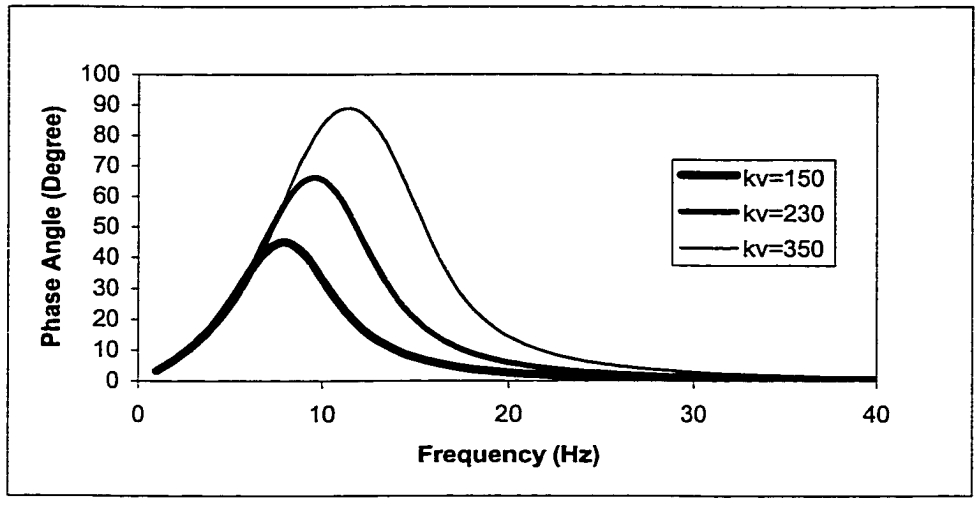

Figure 3.19. Phase Angle of the Hydromount for Various Volumetric Stiffnesses

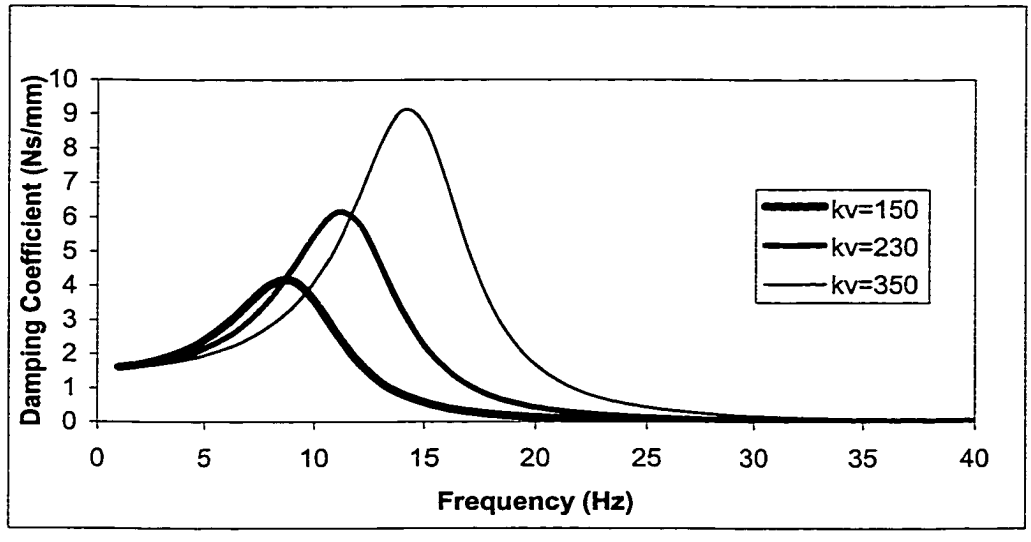

Figure 3.20. Damping Coefficient of the Hydromount for Various Volumetric Stiffnesses

loss angle. Figure 3.23 presents plots of the damping coefficient versus frequency for various equivalent piston areas. It is seen that the peak damping coefficient increases slightly with the increase of the equivalent piston area. The frequencies at the points of the maximum loss angle and maximum damping coefficient increase with the decrease of the equivalent piston area.

Effect of Inertia Track Cross-sectional Area

The variations of dynamic stiffness versus frequency, loss angle versus frequency and damping coefficient versus frequency for various inertia track cross-sectional areas are shown in Figures 3.24, 3.25 and 3.26. The peak dynamic stiffness increases with increasing inertia track cross-sectional area. The peak loss angle increases with increasing inertia track cross-sectional area.

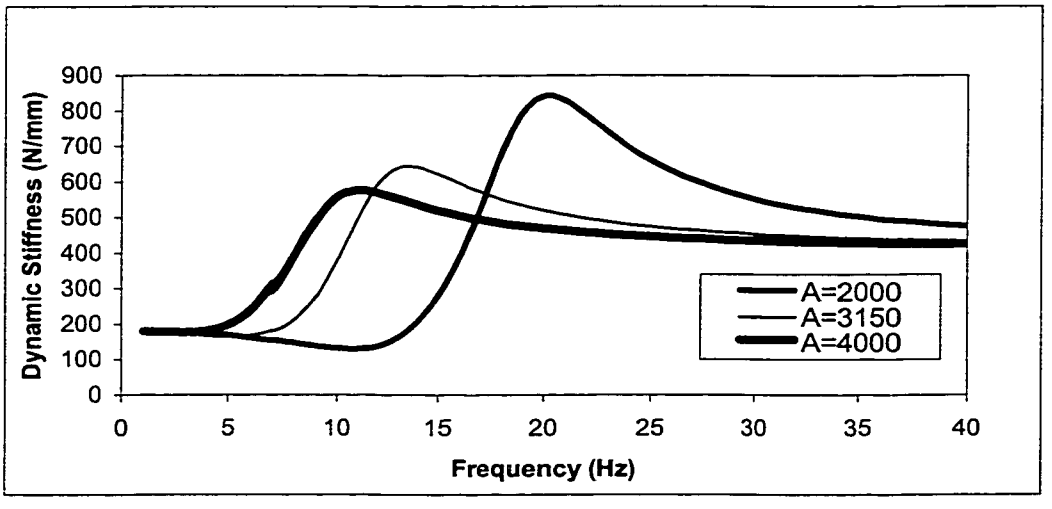

Figure 3.21. Dynamic Stiffness of the Hydromount for Various Equivalent Piston Areas

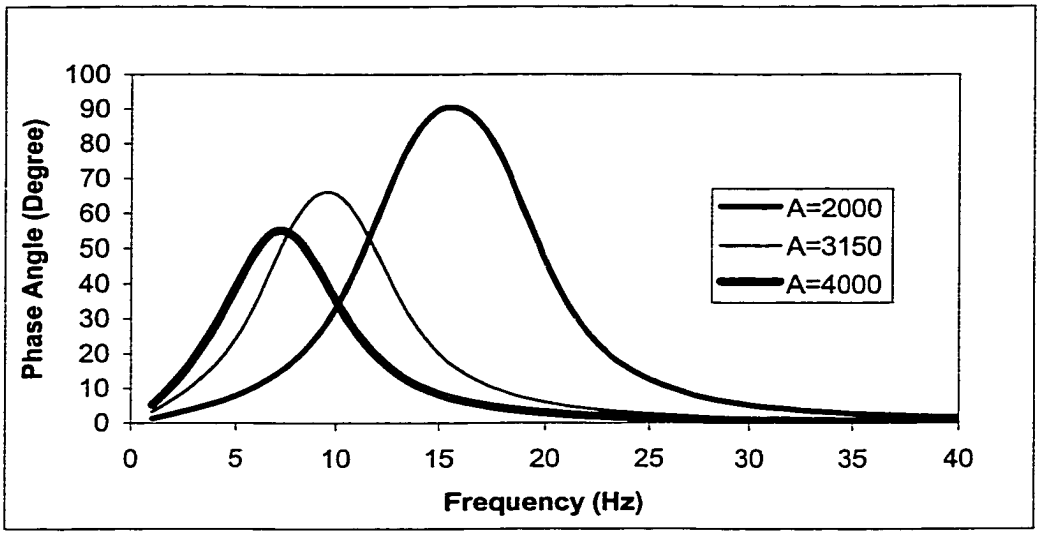

Figure 3.22. Phase Angle of the Hydromount for Various Equivalent Piston Areas

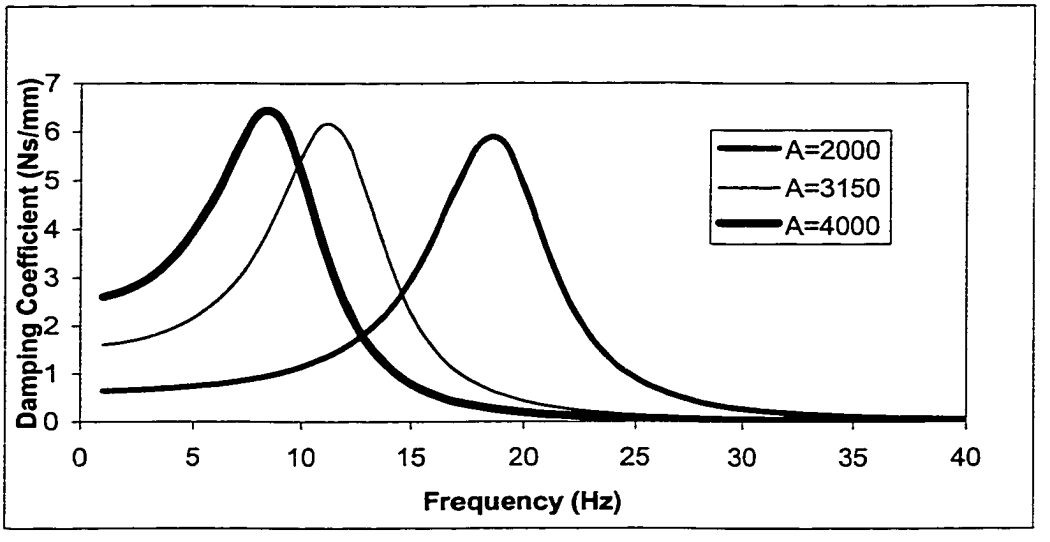

Figure 3.23. Damping Coefficient of the Hydromount for Various Equivalent Piston Areas

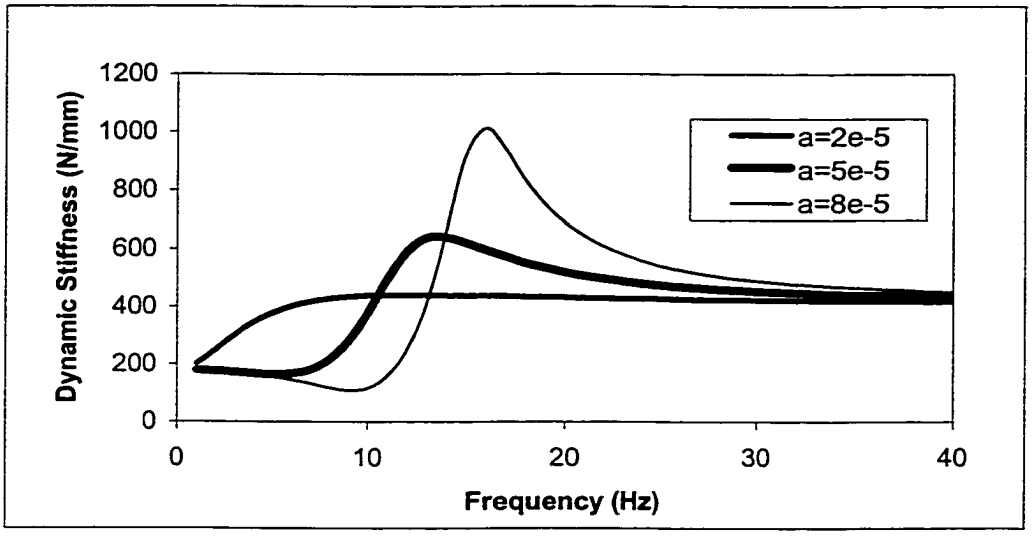

Figure 3.24. Dynamic Stiffness of the Hydromount for Various Inertia Track Cross-sectional Areas

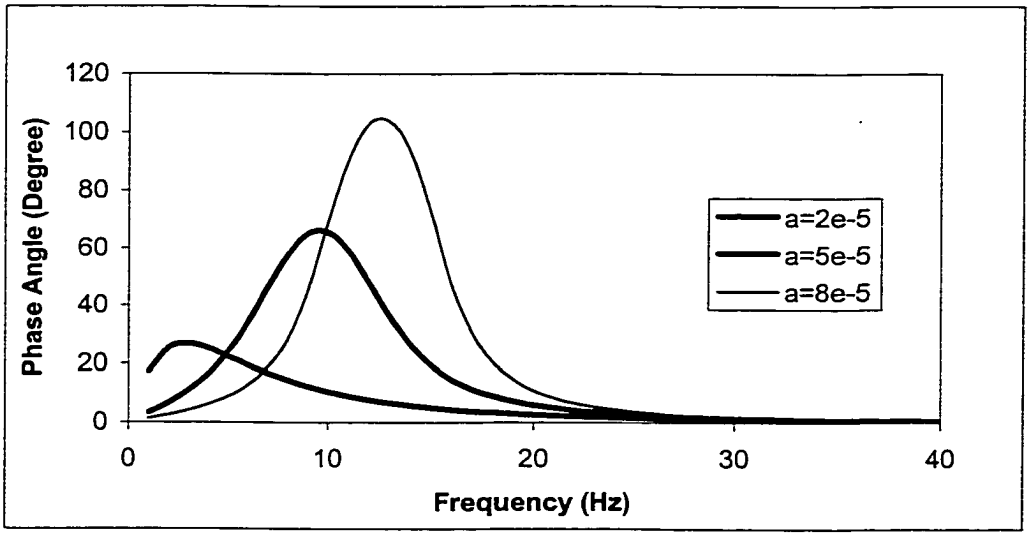

Figure 3.25. Phase Angle of the Hydromount for Various Inertia Track Cross-sectional Areas

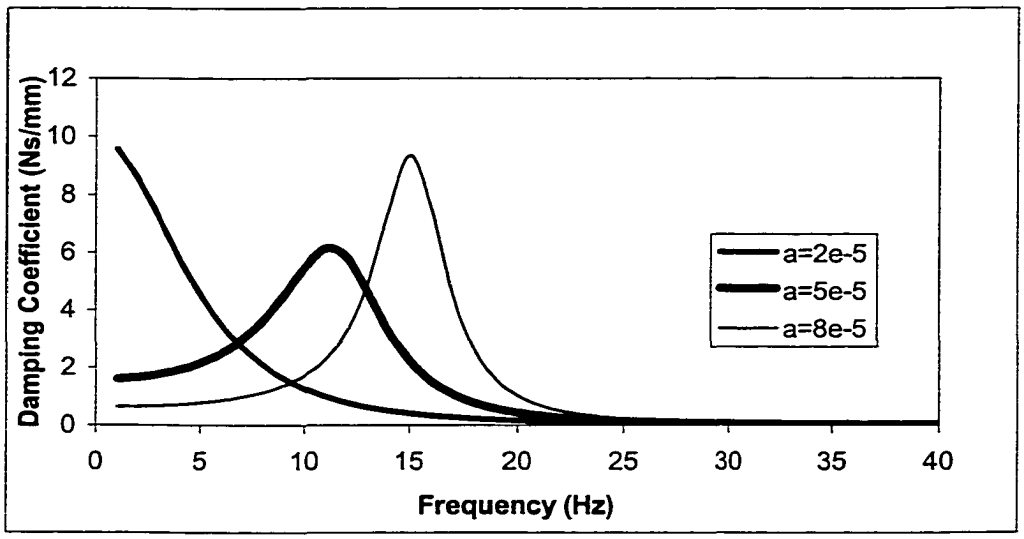

Figure 3.26. Damping Coefficient of the Hydromount for Various Inertia Track Cross-sectional Areas

It is seen that the increased inertia track cross-sectional area increases the peak damping coefficient. The frequencies at the points of the maximum phase angle and damping coefficient increase with the increase of the inertia track cross-sectional area.

Effect of Inertia Track Length

Figure 3.27 presents plots of dynamic stiffness versus frequency for various inertia track lengths. The peak dynamic stiffness increases with the increase of the inertia track length. Figure 3.28 presents plots of loss angle versus frequency with various inertia track lengths. The peak loss angle increases with the increase of the inertia track length. Figure 3.29 presents plots of the damping coefficient versus frequency for various inertia track lengths. It is seen that the peak damping coefficient increases with the increase of

the inertia track lengths. The frequencies at the points of the maximum loss angle and damping coefficient decrease with the increase of the inertia track length.

Effect of Fluid Density

Figure 3.30 presents plots of dynamic stiffness versus frequency for various densities. The peak dynamic stiffness increases with the increase of density. Figure 3.31 presents plots of loss angle versus frequency for various densities. It is seen that the increased density increases the peak loss angle. Figure 3.32 presents plots of the damping coefficient versus frequency for various densities. The peak damping coefficient increases with the increase of the density. The frequencies at the points of the maximum loss angle and damping coefficient decrease with the increase of density.

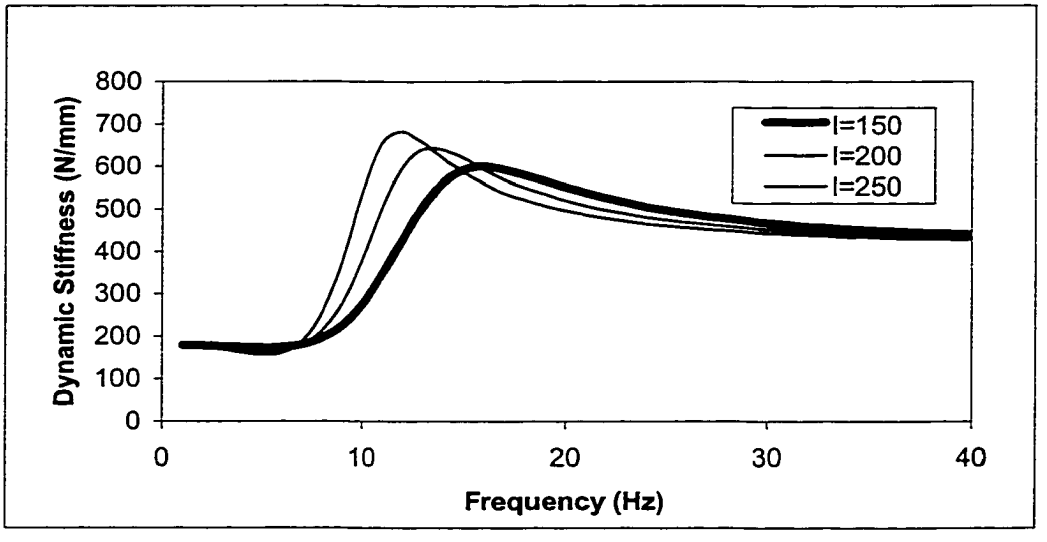

Figure 3.27. Dynamic Stiffness of the Hydromount for Various Inertia Track Lengths

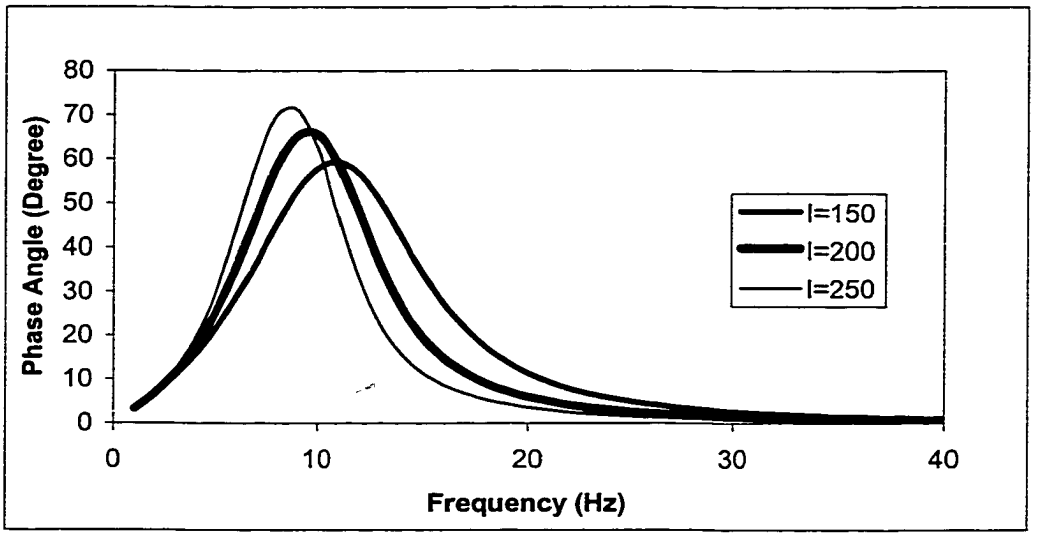

Figure 3.28. Phase Angle of the Hydromount for Various Inertia Track Lengths

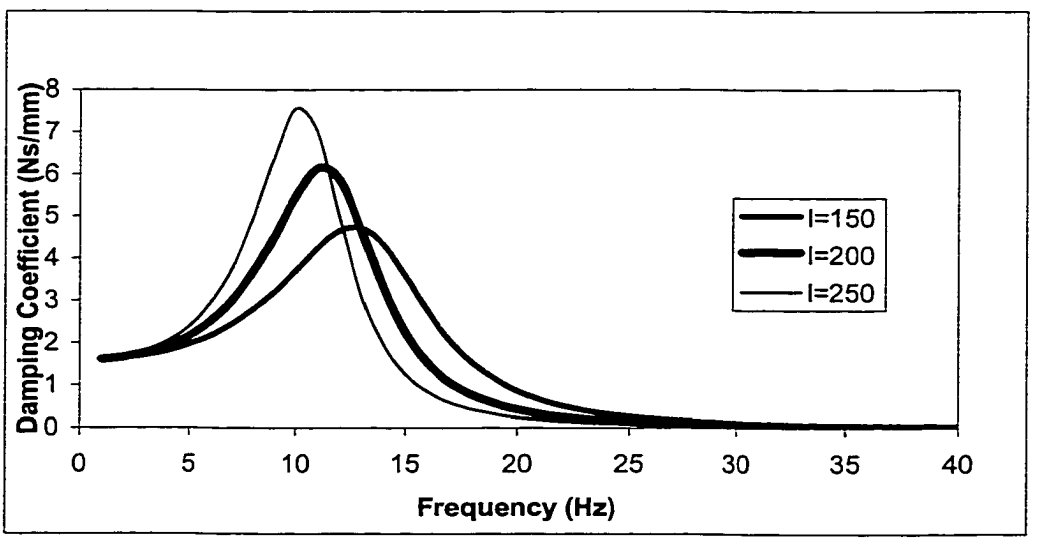

Figure 3.29. Damping Coefficient of the Hydromount for Various Inertia Track Lengths

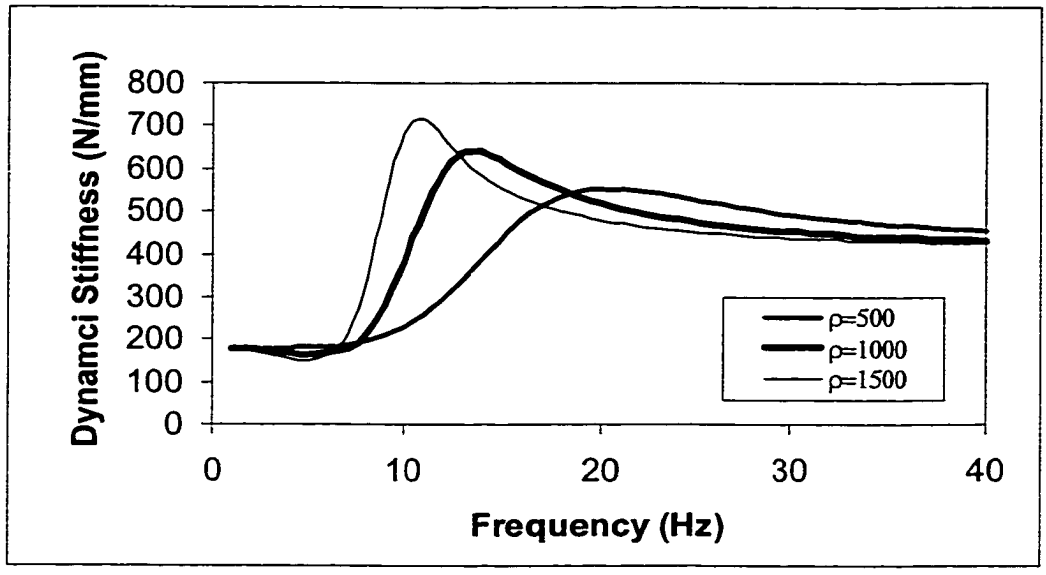

Figure 3.30. Dynamic Stiffness of the Hydromount for Various Densities

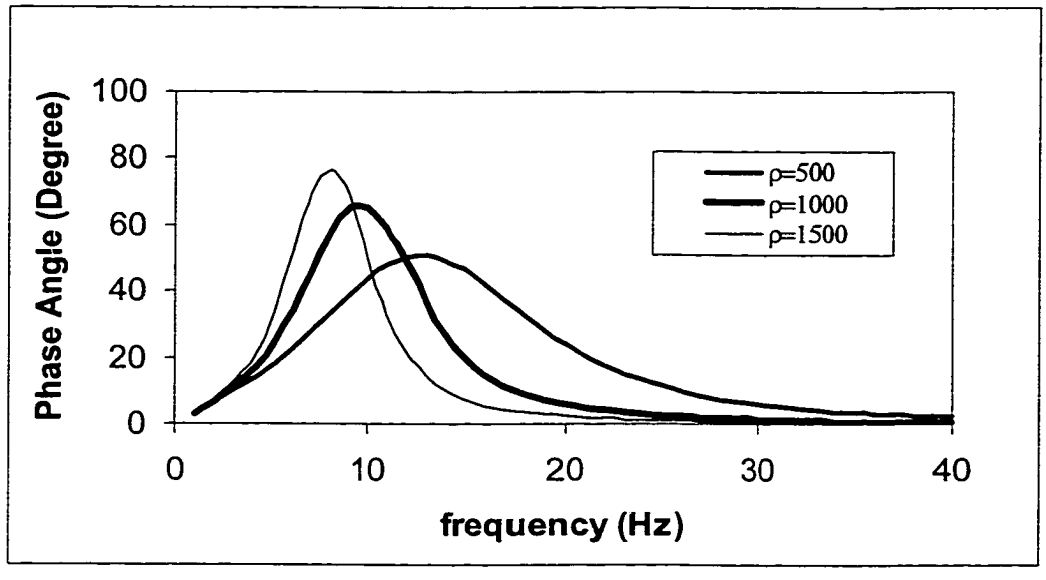

Figure 3.31. Phase Angle of the Hydromount for Various Densities

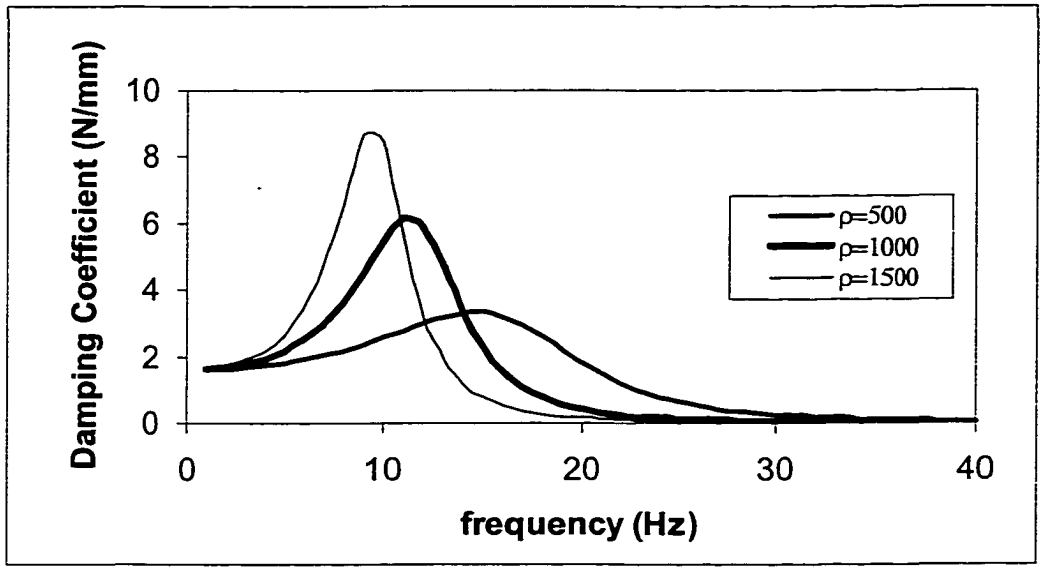

Figure 3.32. Damping Coefficient of the Hydromount for Various Densities

Conclusion

The conclusions from the parametric study are tabulated in Table 3.2. The results agree experimental study by Gau and Cotton (1995).

Table 3.2

Peak Dynamic Property Changes due to Increased Parameter Values

Parameter Increased	k_d	ϕ	C	f
C_r	No Effect	No Effect	No Effect	No Effect
k_s	Increase	Decrease	No Change	No Change
k_v	Increase	Increase	Increase	Increase
A	Decrease	Decrease	Increase	Decrease
a	Increase	Increase	Increase	Increase
l	Increase	Increase	Increase	Decrease
ρ	Increase	Increase	Increase	Decrease

Inertia Track Locks at High Frequency

The third term on the right hand side of equation 3.30 represents the inertia track effect on the dynamic properties. Using the physical hydromount given earlier, it is found that both its real and imaginary parts approach zero for high values of frequency (Figure 3.33). This indicates that the inertia track effectiveness diminishes at high frequencies, due to a practically locked inertia track.

It is interesting to note that at high frequencies the dynamic stiffness reduces to the sum of static stiffness and volumetric stiffness, as the third term of equation 3.30 vanishes. This phenomenon makes it possible to measure the volumetric stiffness experimentally. And this phenomenon also lays the foundation for the theoretical prediction of volumetric stiffness as discussed earlier.

Because of the locked inertia track at high frequencies, the hydromount model becomes as simple as two parallel springs and a dashpot as shown in Figure 3.34.

Frequency at Maximum Loss Angle

From Equations 3.9 and 3.11, the damping ratio ζ of the inertia track is

$$\zeta = \frac{C_I \omega_n}{2k_v}\left(\frac{A}{a}\right)^2 \tag{3.32}$$

Let β be the frequency ratio

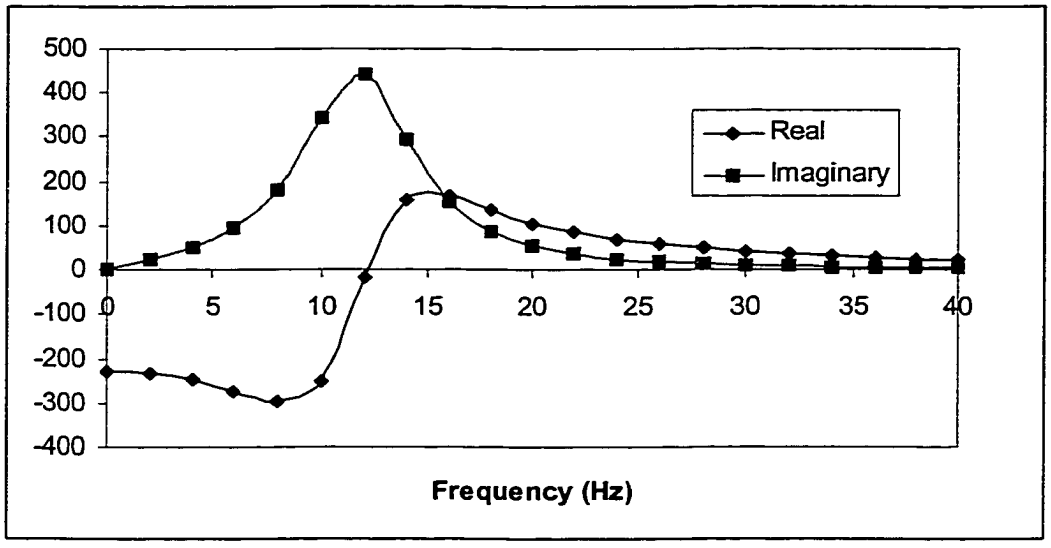

Figure 3.33. Real and Imaginary Parts of Inertia Track Stiffness Term

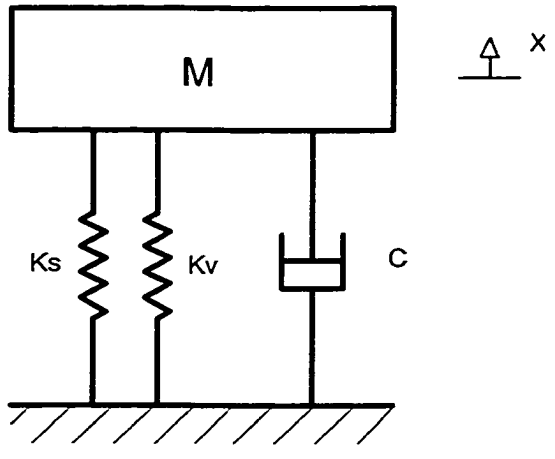

Figure 3.34. High Frequency Hydromount Model

$$\beta = \frac{\omega}{\omega_n} \tag{3.33}$$

The dimensionless form of equation 3.30 is then expressed by

$$\frac{k_d}{k_v} = \frac{1}{k} - \frac{1-\beta^2}{(1-\beta^2)^2 + (2\zeta\beta)^2} + \frac{2\zeta\beta}{(1-\beta^2)^2 + (2\zeta\beta)^2} i \tag{3.34}$$

where k is the dynamic stiffness ratio:

$$k = \frac{k_v}{k_s + k_v} \tag{3.35}$$

The loss angle ϕ can be obtained by

$$\tan\phi = \frac{2k\zeta\beta}{(1-\beta^2)^2 + (2\zeta\beta)^2 - k(1-\beta^2)} \tag{3.36}$$

To maximize the loss angle, ϕ, the derivative of equation 3.36 with respect to the frequency ratio β must be zero, which leads to

$$3\beta^4 + (k - 2 + 4\zeta^2)\beta^2 + k - 1 = 0 \tag{3.37}$$

The solution of equation 3.37, which is illustrated in Figure 3.35, is dependent on the dynamic stiffness ratio k and damping ratio ζ. The decrease in stiffness and damping ratios, the frequency at the maximum damping point is more close to the fluid resonant frequency.

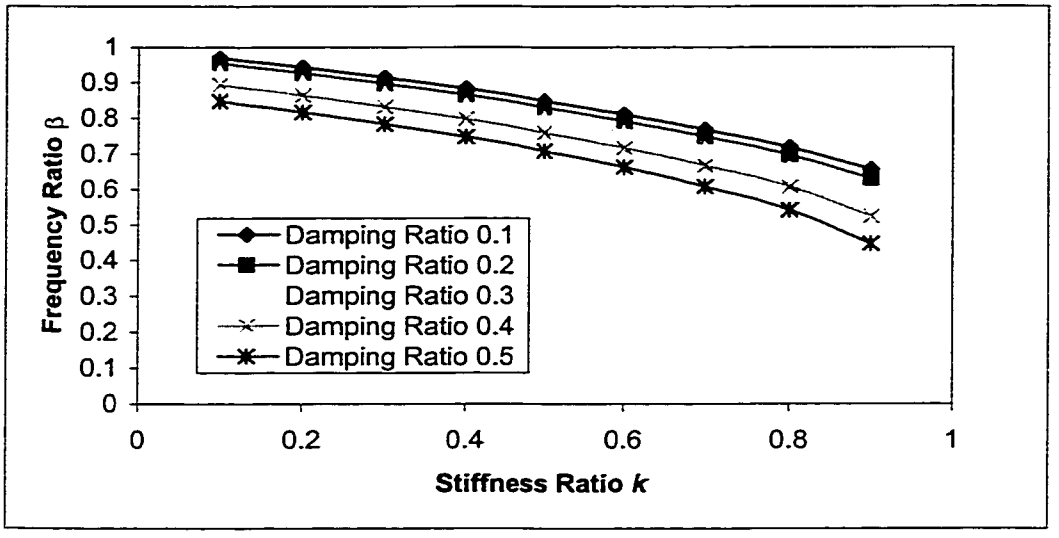

Figure 3.35. Plot of Frequency Ratio β Versus Stiffness Ratio k

Using the physical hydromount example given earlier, with a theoretical fluid resonant frequency 12.12 Hz (according to equation 3.10), the theoretical damping ratio ζ of this hydromount is 0.26 (according to equation 3.32), and its dynamic stiffness ratio is 0.44 (according to equation 3.35). From Figure 3.35, the frequency at the maximum loss angle is calculated as 9.7 Hz. It agrees well with the measured result (9 Hz, see Figure 3.7).

Dynamic Stiffness Ratio Effect on the Dynamic Characteristics

Figures 3.36 and 3.37 represent plots of k_d/k_v and loss angle versus the frequency ratio f/f_n for various values of the dynamic stiffness ratio k. It is seen that an increase of stiffness ratio k results in a decrease of k_d/k_v, with an increase of the loss angle. It also shows that the lower the stiffness ratio k, the closer the maximum loss angle occurs to the frequency ratio of 1, which agrees with the previous finding. As will be discussed in the next section, the lower the loss angle of a hydromount, the higher the damping

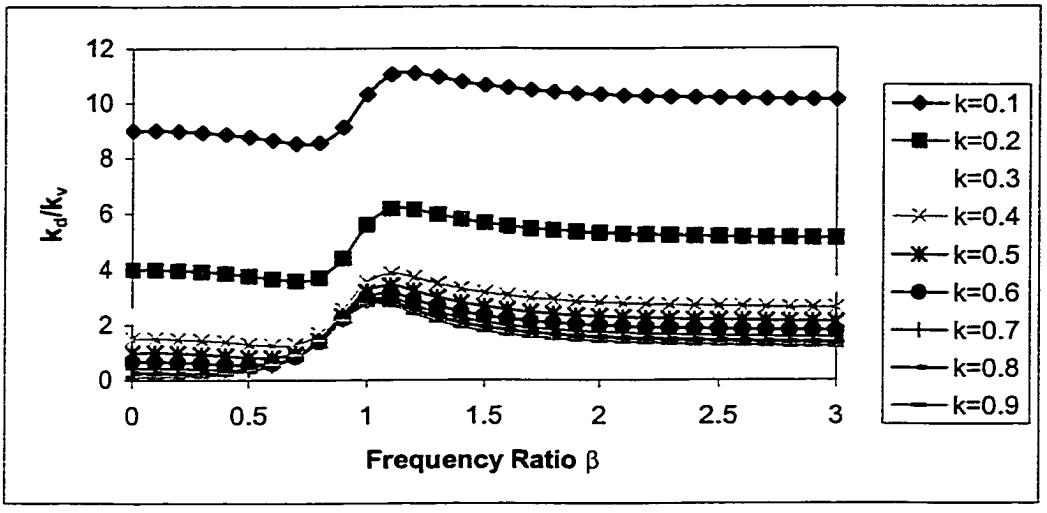

Figure 3.36. Plots of K_d/k_v Versus Frequency Ratio β for Various Stiffness Ratios k ($\zeta = 0.2$)

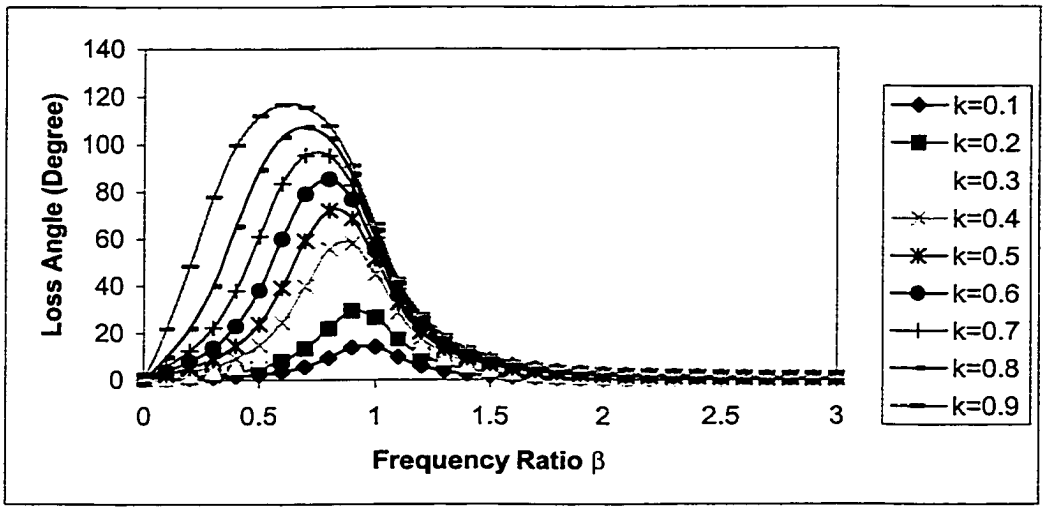

Figure 3.37. Plots of Loss Angle Versus Frequency Ratio β for Various Stiffness Ratio k ($\zeta = 0.2$)

coefficient. Therefore, with the low stiffness ratio k, the mount generates the high damping in the tuned frequency.

Damping Ratio Effect on the Dynamic Characteristics

The variations of k_d/k_v and the loss angle versus the frequency β for various values of the damping ratios are shown in Figures 3.38 and 3.39. It is seen that an increase of damping ratio results in a decrease of the peak value of k_d/k_v, as well as the loss angle.

Stiffness Dip

The dynamic stiffness of some hydromounts at certain frequencies is lower than the static stiffness (see Figure 3.40). This phenomenon is called the stiffness dip. Traditionally, the anti-resonance concept is employed to explain this phenomenon in the qualitative level (Ford, 1997). When the frequency of the exciting force approaches the anti-resonance of the fluid mass spring system, the fluid mass begins to affect the input force required to maintain the fixed amplitude input. At the anti-resonance, the fluid will tend to move near-in-phase with the input force and, therefore, tend to add a force in the same direction as the input force. It results in a stiffness decrease since the input force has to decrease to maintain the fixed displacement due to the fluid mass adding a force in the same direction as the input force.

To find the range where the dynamic stiffness of the hydromount is lower than static stiffness, let equation 3.30 be less than k_s, therefore

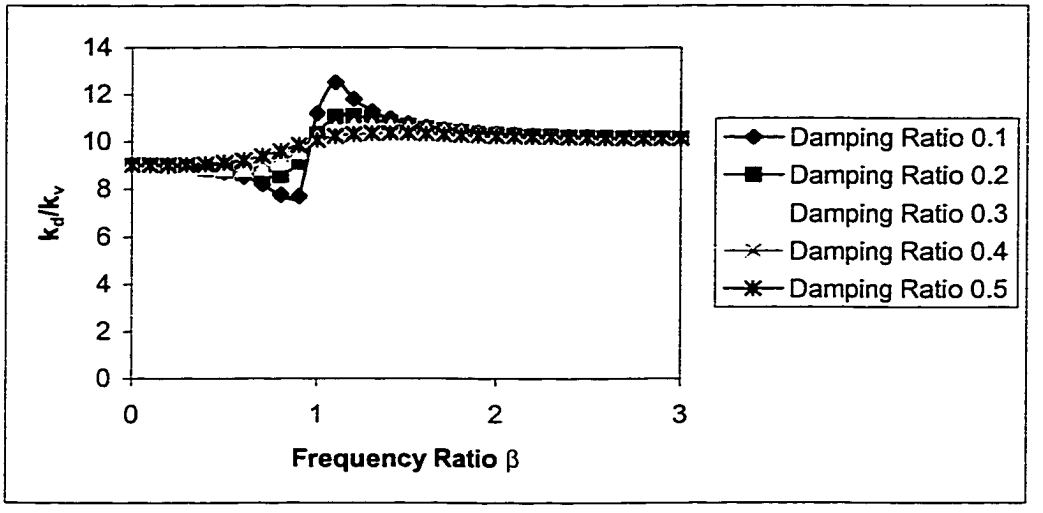

Figure 3.38. Plots of K_d/k_v Versus Frequency Ratio β
($k = 0.1$)

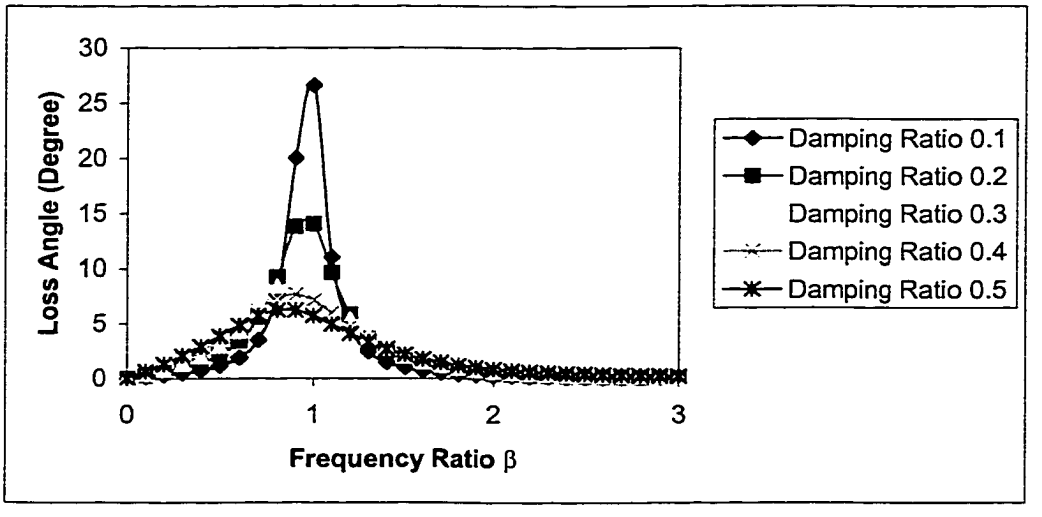

Figure 3.39. Plots of Loss Angle Versus Frequency Ratio β
($k = 0.1$)

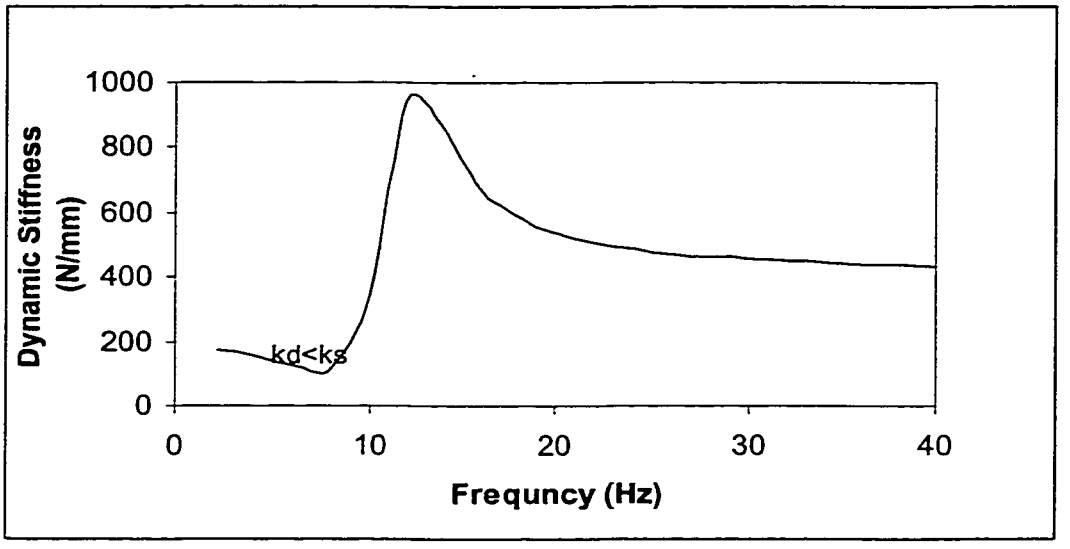

Figure 3.40. Schematic of Stiffness Dip

$$k_v - \frac{k_v^2\left(\frac{a}{A}\right)^2}{k_v\left(\frac{a}{A}\right)^2 - la\rho\omega^2 + iC_f\omega} \leq 0 \tag{3.38}$$

Equation 3.38 can further be expressed as

$$\frac{1}{1-\beta^2+2\zeta\beta i} \geq 1 \tag{3.39}$$

Therefore,

$$\beta^4 + 2(2\zeta^2 - 1)\beta^2 \leq 0 \tag{3.40}$$

which leads to

$$0 \le \beta \le \sqrt{2\left(1-2\zeta^2\right)} \tag{3.41}$$

But

$$1-2\zeta^2 \ge 0 \tag{3.42}$$

which leads to

$$\zeta \le 0.707 \tag{3.43}$$

It is therefore concluded that the "stiffness dip" phenomenon occurs only to a hydromount with the inertia track damping ratio equal to or less than 0.707.

Hydromount System Resonant Frequency

The equivalent spring mass damper system of the hydromount can be illustrated in Figure 3.41 based on the fact that the dynamic stiffness of a hydromount can be expressed by the storage stiffness k' and loss stiffness k'' (equations 3.27 and 3.28), which are both frequency dependent. The in-phase stiffness with force input k' affects the system resonant frequency. Dividing equation 3.27 by k_v, then

$$\frac{k'}{k_v} = \frac{1}{k} - \frac{1-\beta^2}{\left(1-\beta^2\right)^2 + \left(2\zeta\beta\right)^2} \tag{3.44}$$

Notice that

$$k_v = \frac{k}{1-k} k_s \tag{3.45}$$

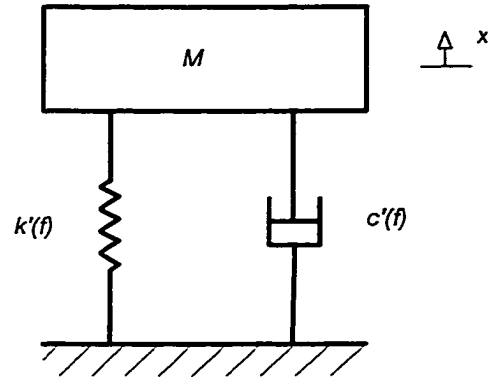

Figure 3.41. Equivalent Hydromount Spring Mass System

Therefore, for the hydromount system shown in Figure 3.41 the resonant frequency is

$$f_n = \frac{1}{2\pi}\sqrt{\frac{\left(\frac{1}{k} - \frac{1-\beta^2}{\left(1-\beta^2\right)^2 + (2\zeta\beta)^2}\right)\left(\frac{k}{1-k}\right)k_s}{m}} \tag{3.46}$$

Denoting the resonant frequency at zero frequency as f_0, then

$$f_n = f_o\sqrt{\left(\frac{1}{k} - \frac{1-\beta^2}{\left(1-\beta^2\right)^2 + (2\zeta\beta)^2}\right)\left(\frac{k}{1-k}\right)} \tag{3.47}$$

The variation of the resonant frequency ratio f_n/f_0 versus the frequency ratio β is shown in Figure 3.43. It is seen that f_n/f_0 decreases at the beginning and then shoots up until the frequency ratio β at some value between 1 to 1.5. It then decreases until it settles down to the value of f_∞, which is

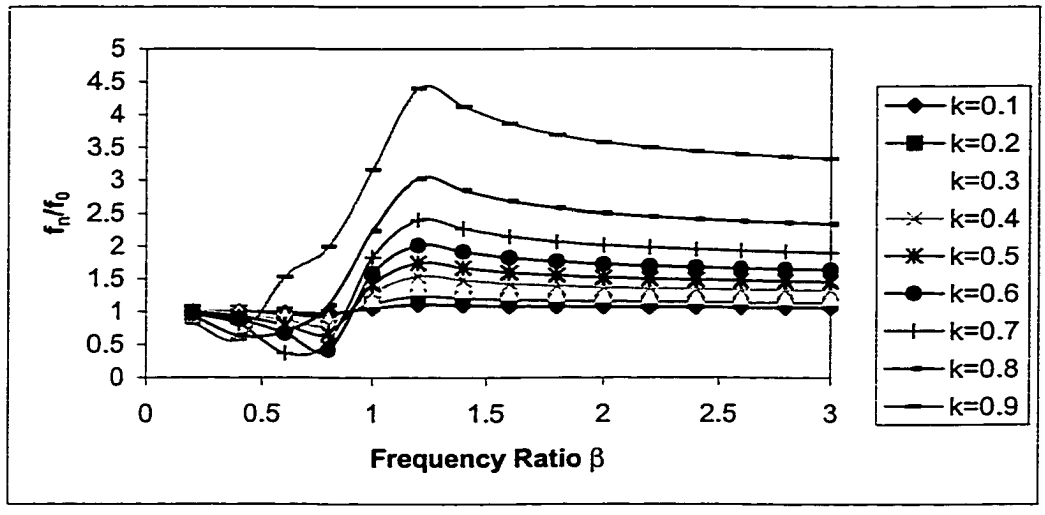

Figure 3.42. Plot of Resonant Frequency Ratio f_n/f_0 Versus Frequency Ratio β (ζ=0.2)

$$f_\infty = \frac{1}{2\pi}\sqrt{\frac{k_s + k_v}{m}} \tag{3.48}$$

or

$$\frac{f_\infty}{f_0} = \sqrt{\frac{1}{1-k}} \tag{3.49}$$

It is interesting to note that when $\beta = 1$, then

$$f_{n(\beta=1)} / f_0 = \sqrt{\frac{1}{1-k}} \tag{3.50}$$

It is concluded that

$$f_\infty = f_{n(\beta=1)} \tag{3.51}$$

Figure 3.43 presents plots of the resonant frequency ratio f_n/f_0 versus the frequency ratio β for the dynamic stiffness ratio $k = 0.5$. It is seen that the lower damping ratio results in a bigger swing of the resonant frequency.

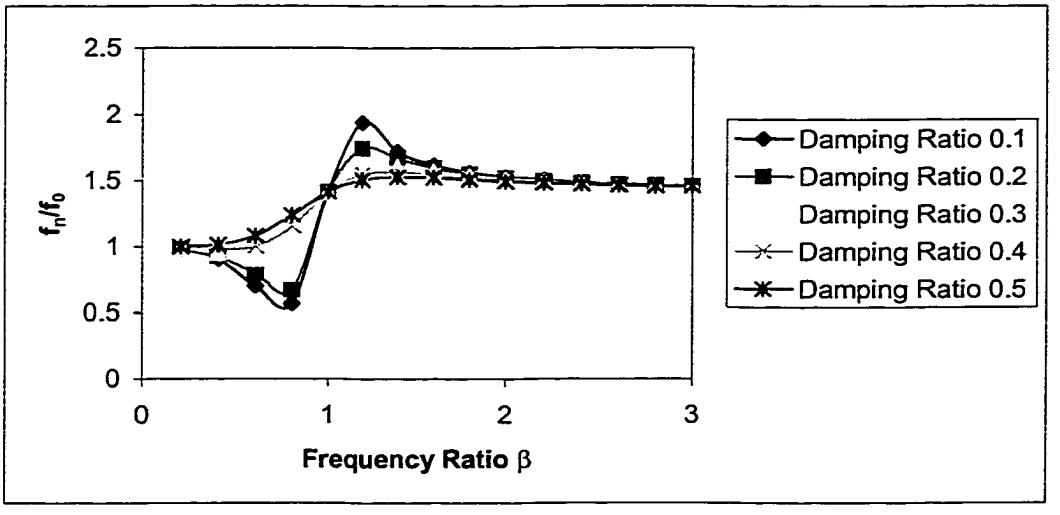

Figure 3.43. Plot of Resonant Frequency Ratio f_n/f_0 Versus Frequency Ratio β ($k = 0.5$)

Hydromount Transmissibility

Based on the equivalent hydromount spring mass system shown in Figure 3.41, the transmissibility (Thomson, 1988) is

$$Tr = \sqrt{\frac{k'^2 + (c\omega)^2}{(k' - m\omega^2)^2 + (c\omega)^2}} \tag{3.52}$$

Figure 3.44 presents plots of the tested and calculated transmissibilities of the physical hydromount given earlier. It is seen that there are two peaks: one is the preload

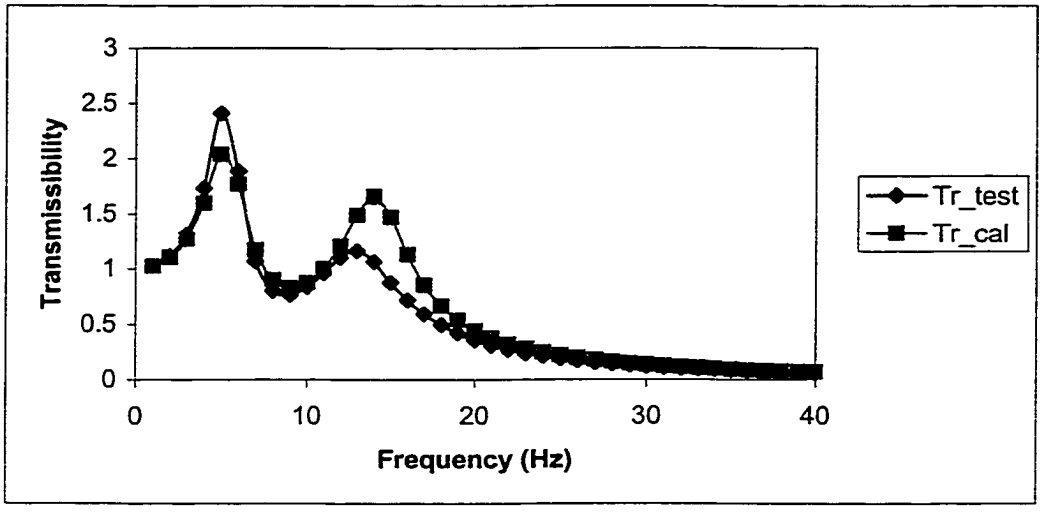

Figure 3.44. Plot of the Measured and Calculated Transmissibility

dependent (the first), the other occurs at the point where the maximum hydromount damping is.

A Hybrid Hydromount—Hydrobushing

As a vibration isolation component in the vehicle suspension and steering wheel assemblies, the bushing includes both the conventional rubber bushing and the more complex hydrobushing. The conventional rubber bushing is composed of a rubber element enclosed by an inner and an outer metal (Figure 3.45). The hydrobushing includes an additional damping generating mechanism consisted of fluid chambers and inertia tracks (Figure 3.46). It is seen that the hydrobushing is a device similar to a hydromount, in which the only difference is that the bottom chamber of the hydromount is sprung by a bellow while the two chambers of the hydrobushing are both pumped by the outer metal. Because of its relatively new technology, there had been no publication before Lu et al (1999, 2000) in the topic of the hydrobushing research.

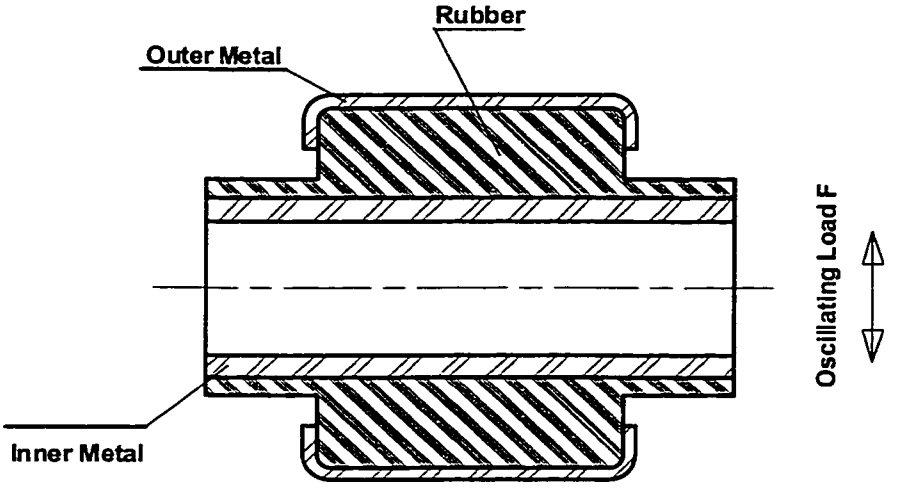

Figure 3.45. Cut-out View of Typical Conventional Rubber Bushing

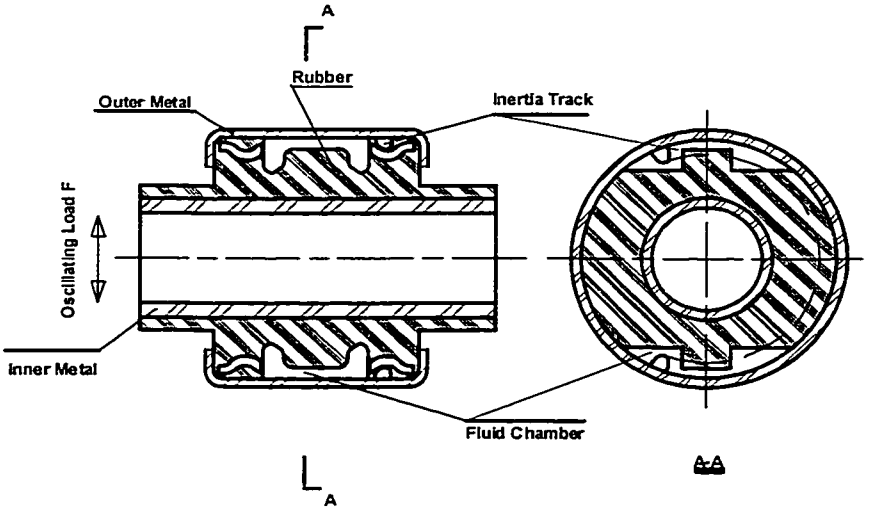

Figure 3.46. Cut-out View of Typical Hydrobushing

Hydrobushing Model

The proposed hydrobushing model is illustrated in Figure 3.47. It is comprised of an inner metal, an outer metal, two fluid chambers with pressures p_1 and p_2 respectively,

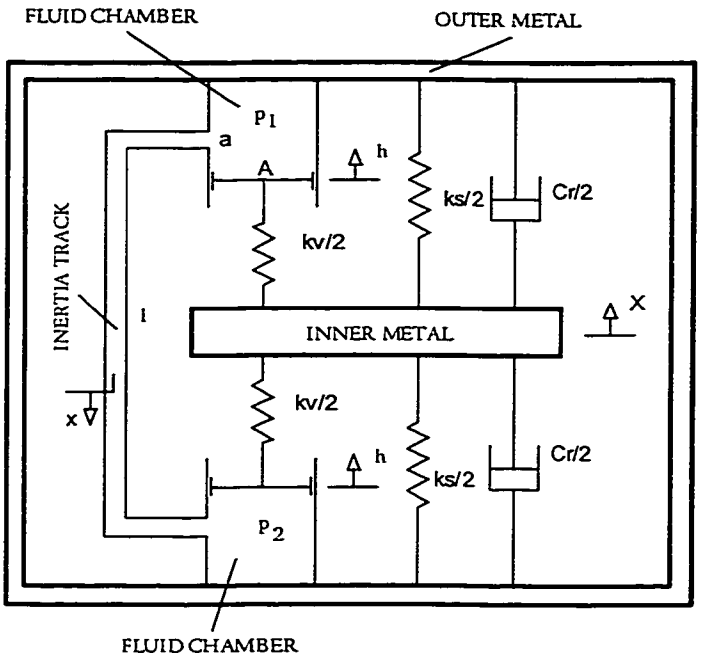

Figure 3.47. Hydrobushing Model

and an inertia track with cross-sectional area a and length l. The rubber section is modeled as rubber static stiffness k_s and damping C_r. When the inner metal is subjected to a sinusoidal displacement input X, the fluid (density ρ) in the chambers is pumped by the equivalent piston (area A). The fluid flows back and forth through the inertia track while the rubber bulges because of the fluid pressure. The stiffness caused by the pressurized fluid is called volumetric stiffness (k_v).

Fundamental Equations

From the hydrobushing model shown in Figure 3.47, the equation of motion of the inertia track fluid is expressed by

$$la\rho\frac{d^2x}{dt^2}+C_I\frac{dx}{dt}=(p_1-p_2)a \tag{3.53}$$

where C_I is the damping coefficient of the inertia track.

The volume conservation equation is

$$hA = xa \tag{3.54}$$

The free body diagrams of two equivalent pistons are illustrated in Figure 3.48. The equilibrium equations are

$$\frac{k_v}{2}(X-h)=p_1A \tag{3.55}$$

And

$$\frac{k_v}{2}(X-h)=p_2A \tag{3.56}$$

Adding equation 3.55 and equation 3.56 gives

$$k_v(X-h)=(p_1-p_2)A \tag{3.57}$$

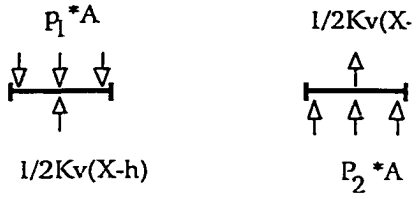

Figure 3.48. Free Body Diagram of Equivalent Pistons

Assuming that the outer metal mass is negligible, the stiffness k_s is linear over the operating range, and the damping C_r is viscous, then the resultant force F on the outer metal is

$$F = k_s X + C_r \frac{dX}{dt} + (p_1 - p_2)A \tag{3.58}$$

It is seen that the fundamental equations of the hydrobushing are the same as those for the hydromount so that it possesses the same properties as the hydromount.

Summary

With the assumption of the lumped damping coefficient, the parameters needed to describe a hydromount are static stiffness (k_s), rubber damping coefficient (C_r), inertia track length (l) and cross-sectional area (a), fluid density (ρ), volumetric stiffness (k_v) and equivalent piston area (A). The inertia track fluid resonant frequency of the hydomount is proportional to the ratio of the cross sectional area of the inertia track to the equivalent piston area. It is also proportional to the square root of volumetric stiffness and is inversely proportional to the square root of the mass of the fluid in the inertia track. The dynamic properties of a hydromount are related to the rubber static stiffness, rubber

damping, rubber bulge affected volumetric stiffness and the oscillating fluid effect (or inertia track effect). But the rubber damping has minimal effect on the hydromount dynamic properties and may be neglected. A parametric study concludes that an increase in rubber static stiffness results in an increase of the peak dynamic stiffness, but a decrease of the peak loss angle. An increase in volumetric stiffness, fluid density, inertia track cross-sectional area and its length result in an increase of both the peak dynamic stiffness and loss angle. At high frequencies, however, the fluid in the inertia track becomes inefficient so that it may be ignored. Therefore, the dynamic stiffness of the hydromount at high frequencies is the sum of the static stiffness and the volumetric stiffness, which laid a foundation to measure the volumetric stiffness experimentally. The maximum loss angle of a hydromount, which corresponds to the maximum damping coefficient, occurs at a frequency close to the fluid resonant frequency. The degree of its closeness depends on the damping ratio and dynamic stiffness ratio. When the inertia track damping ratio is equal to or less than 0.707, the hydromount exhibits a phenomenon called stiffness dip. The resonant frequency of the hydromount system is a function of the frequency too. At the point where the inertia track fluid resonates, the hydromount system resonant frequency is equal to that at very high frequencies. Two peaks are seen in the transmissibility plot, at which one is preload dependent, the other is the hydromount frequency.

The hydromount dynamic characteristics are predictable theoretically with the assumed inertia track damping coefficient C_I as the procedure shown in Figure 3.49. The mechanism of C_I will be studied in Chapter V.

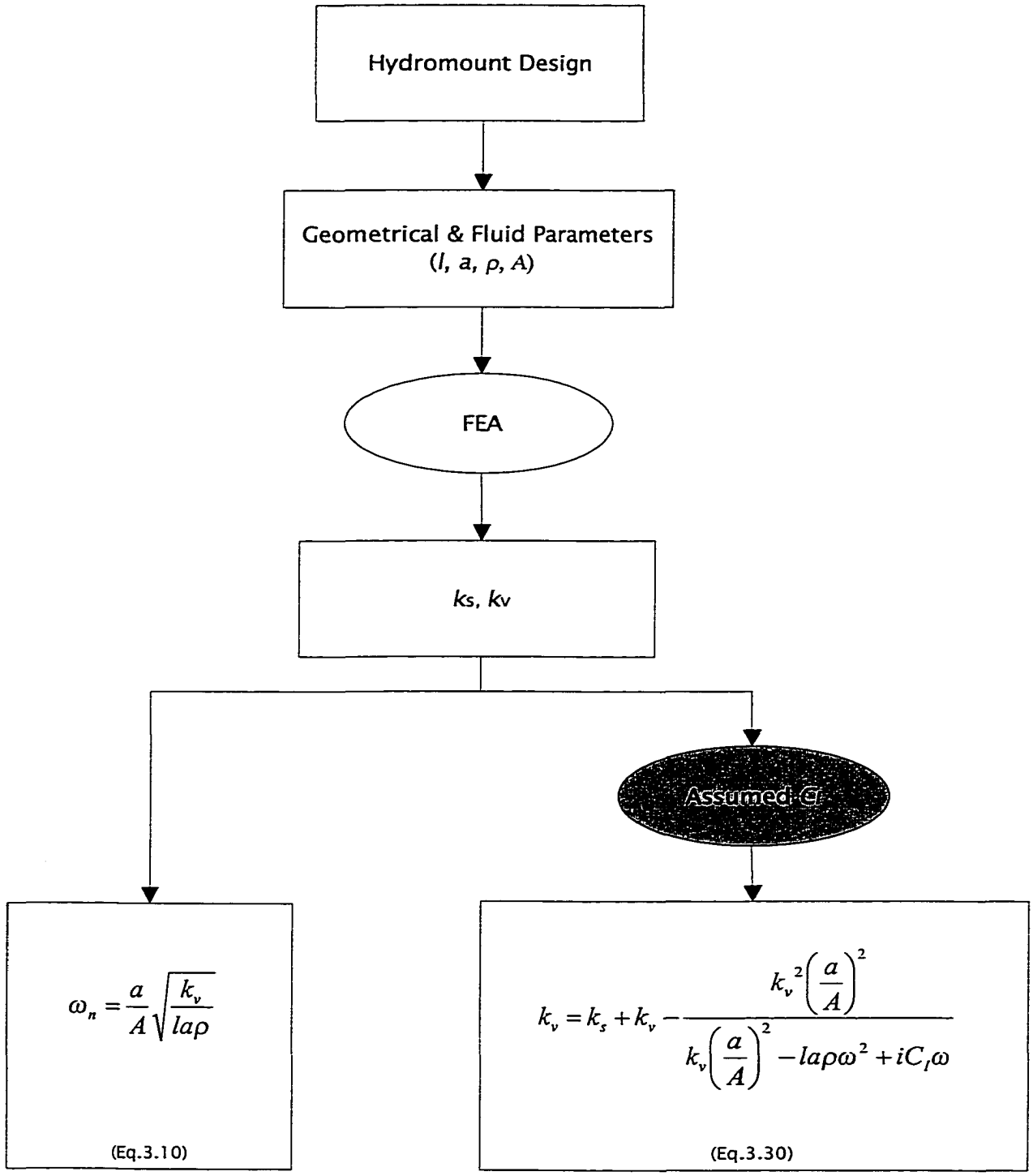

Figure 3.49. Hydromount Dynamic Characteristics Prediction Procedure With Assumed Inertia Track Damping Coefficient

CHAPTER IV

HYDROMOUNT WITH MULTIPLE INERTIA TRACKS

In this chapter the hydromount with multiple inertia tracks is studied. The hydromount models with multiple inertia tracks, either identical or non-identical, are proposed. The effects of the number of the inertia tracks on the fluid resonant frequency, the fluid displacements in the inertia tracks, the equivalent piston displacement, the fluid pressure difference, the dynamic stiffness and the loss angle are investigated.

Hydromount With Identical Inertia Tracks

The proposed hydromount model with two identical inertia tracks is shown in Figure 4.1.

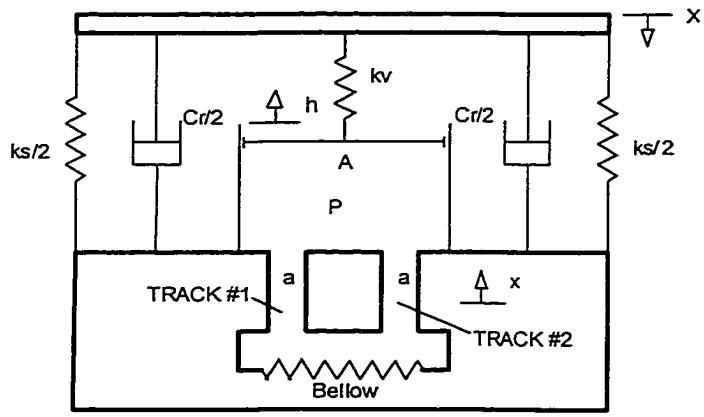

Figure 4.1. Hydromount Model With Two Identical Inertia Tracks

The equation of motion of the fluid in each inertia track is the same as equation 3.4. The volume conservation equation is

$$hA = nxa \tag{4.1}$$

where n is the track numbers.

The equivalent piston balance equation and the resultant force F on the outer metal are expressed by equations 3.6 and 3.7.

Inertia Track Fluid System Equation

Substituting h from equation 4.1 into equation 3.6, the pressure difference becomes

$$p = \frac{k_v}{A}\left(X - \frac{nxa}{A}\right) \tag{4.2}$$

Substituting equation 4.2 into equation 3.4 gives

$$la\rho\frac{d^2x}{dt^2} + C_I\frac{dx}{dt} + nk_v\left(\frac{a}{A}\right)^2 x = k_v\left(\frac{a}{A}\right)X \tag{4.3}$$

Equation 4.3 is the system differential equation of the fluid in the inertia track.

n-Effect on the Inertia Track Resonant Frequency

The resulting resonant frequency of the fluid in the inertia tracks from equation 4.3 is

$$\omega_n = \frac{a}{A}\sqrt{\frac{nk_v}{la\rho}} \tag{4.4}$$

It is seen that the inertia track fluid resonant frequency of the hydromount with the multiple identical inertia tracks is the square root of n times the fluid resonant frequency with the single inertia track. To illustrate the effect of the number of inertia tracks on the fluid resonant frequency, the numerical results based on the physical hydromount given in Chapter III are presented in Table 4.1.

Table 4.1

Track Number Effect on the Fluid Resonant Frequency

	$n=1$	$n=2$	$n=3$
f (Hz)	12.12	17.14	20.99

It will be shown later that the maximum loss angle of the multiple track hydromount occurs near the point of the fluid resonance, as in the case of the single track device. Therefore, the measured frequency at the maximum loss angle indicates the magnitude of the fluid resonant frequency. The measured dynamic characteristics of the hydromount with two inertia tracks is shown in Figure 4.2, for which two test cases are plotted: one with two open inertia tracks and another with only one open inertia track (sealed one with silicon). It is seen that the ratio of the frequencies at the maximum loss angle between two tracks and one track is about 1.414, which agrees with equation 4.4.

n-Effect on the Fluid Displacement in Inertia Tracks

The solution of equation 4.3 gives

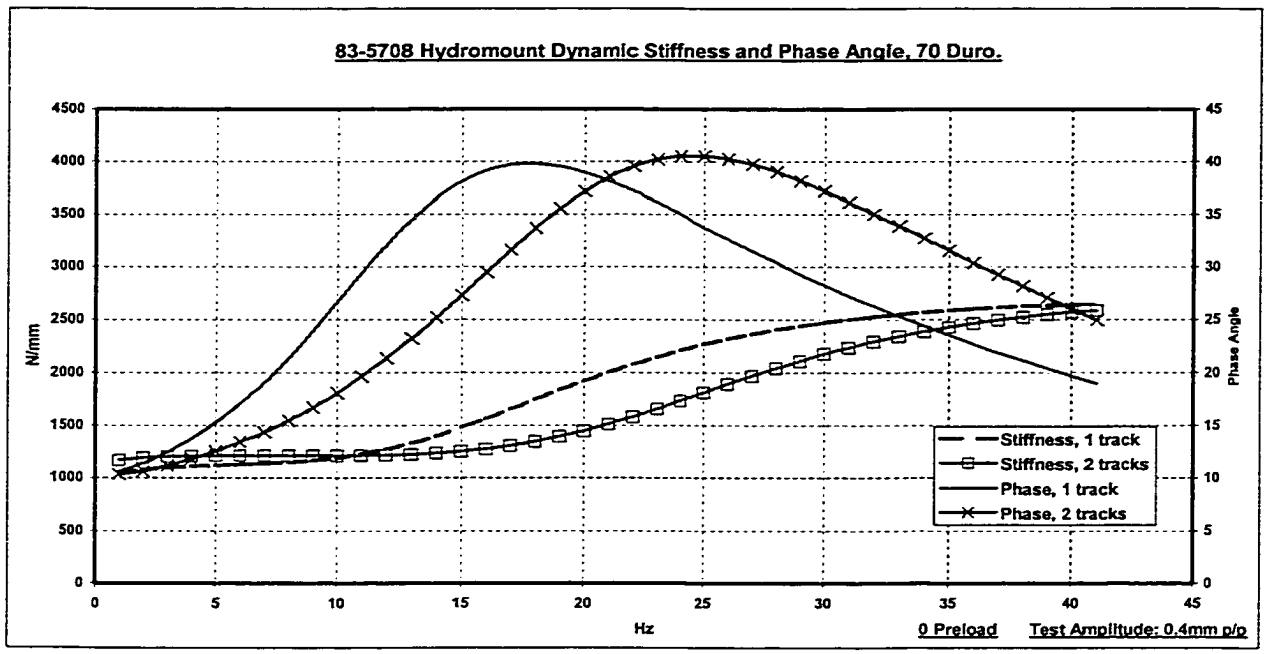

Figure 4.2. Measured Dynamic Characteristics of A Hydromount With One and Two Inertia Tracks

$$x = \frac{k_v\left(\frac{a}{A}\right)X}{\left[nk_v\left(\frac{a}{A}\right)^2 - la\rho\omega^2\right] + iC_I\omega} \tag{4.5}$$

where X is sinusoidal as expressed by equation 3.1. Assuming x is periodical expressed by equation 3.13, then,

$$x_0 e^{i\phi_x} = \left\{ \frac{nk_v\left(\frac{a}{A}\right)^2 - la\rho\omega^2}{\left[nk_v\left(\frac{a}{A}\right)^2 - la\rho\omega^2\right]^2 + (C_I\omega)^2} - \frac{iC_I\omega}{\left[nk_v\left(\frac{a}{A}\right)^2 - la\rho\omega^2\right]^2 + (C_I\omega)^2} \right\} \left[k_v\left(\frac{a}{A}\right)X_0 \right] \tag{4.6}$$

Hence

$$x_0 = \frac{k_v\left(\frac{a}{A}\right)X_0}{\sqrt{\left[nk_v\left(\frac{a}{A}\right)^2 - la\rho\omega^2\right]^2 + (C_l\omega)^2}} \tag{4.7}$$

and the phase angle ϕ_x is

$$\phi_x = \arctan\left(-\frac{C_l\omega}{nk_v\left(\frac{a}{A}\right)^2 - la\rho\omega^2}\right) \tag{4.8}$$

The variations of the fluid displacement and the phase angle versus the forcing frequency with multiple inertia tracks are shown in Figures 4.3 and 4.4. They show that x_0/X_0 peaks at the frequency where the fluid in the inertia track resonates (n = 1 at 12.12 Hz; n = 2 at 17.14 Hz and n = 3 at 21 Hz). The magnitude of x_0/X_0 decreases for higher number n of inertia tracks. At the resonant frequencies, there is a phase shift from –90° to 90°.

n-Effect on the Equivalent Piston Displacement *h*

Substituting equation 4.5 into equation 4.1, the equivalent piston displacement h becomes

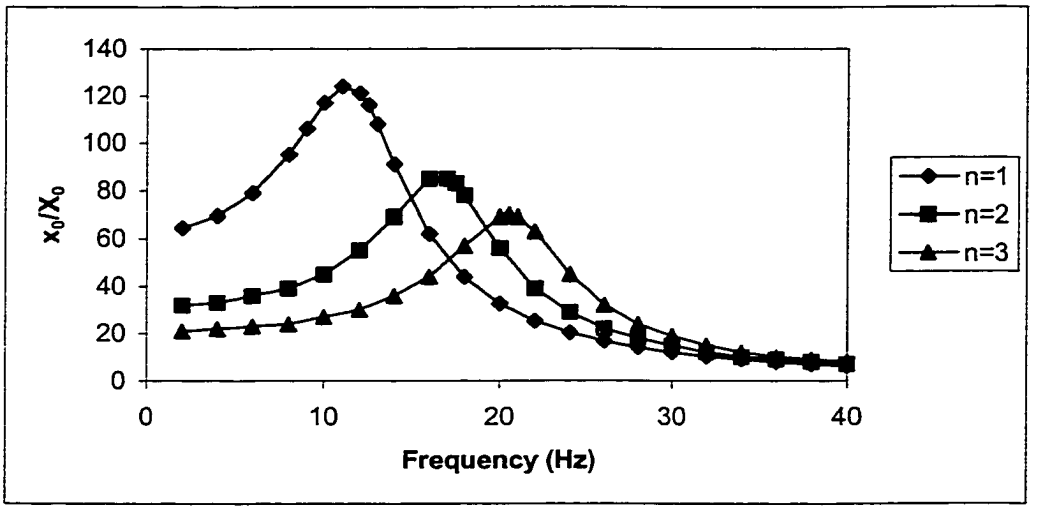

Figure 4.3. x_0/X_0 vs. Frequency for Various Number of Inertia Tracks

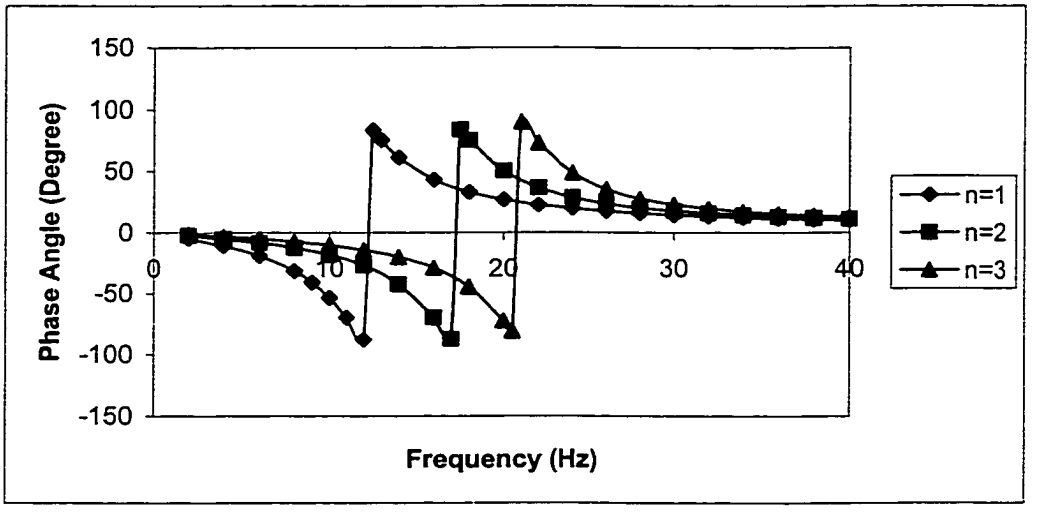

Figure 4.4. Loss Angle vs. Frequency for Various Number of Inertia Tracks

$$h = -\frac{k_v\left(\frac{a}{A}\right)^2 X}{\left[nk_v\left(\frac{a}{A}\right)^2 - la\rho\omega^2\right] + iC_l\omega} \tag{4.9}$$

Let h be

$$h = h_0 e^{i(\omega t+\phi_h)} \tag{4.10}$$

where ϕ_h is the phase difference between h and X.

Then,

$$h_0 e^{i\phi_x} = \left\{\frac{nk_v\left(\frac{a}{A}\right)^2 - la\rho\omega^2}{\left[nk_v\left(\frac{a}{A}\right)^2 - la\rho\omega^2\right]^2 + (C_l\omega)^2} - \frac{iC_l\omega}{\left[nk_v\left(\frac{a}{A}\right)^2 - la\rho\omega^2\right]^2 + (C_l\omega)^2}\right\}\left[k_v\left(\frac{a}{A}\right)^2 X_0\right] \tag{4.11}$$

Hence

$$h_0 = \frac{k_v\left(\frac{a}{A}\right)^2 X_0}{\sqrt{\left[nk_v\left(\frac{a}{A}\right)^2 - la\rho\omega^2\right]^2 + (C_l\omega)^2}} \tag{4.12}$$

and the phase angle ϕ_h is

$$\phi_h = \tan^{-1}\left(-\frac{C_I\omega}{nk_v\left(\frac{a}{A}\right)^2 - la\rho\omega^2}\right) \tag{4.13}$$

It is seen that

$$\phi_x = \phi_h \tag{4.14}$$

which means x and h are in phase.

The variation of h_0/X_0 versus frequency for the hydromount with various inertia track numbers based on the physical hydromount given in Chapter III is shown in Figure 4.5. Again, h_0/X_0 peaks at the fluid resonant frequencies (n = 1 at 12.12 Hz; n = 2 at 17.14 Hz and n = 3 at 21 Hz), and the magnitude of x_0/X_0 decreases for higher n values.

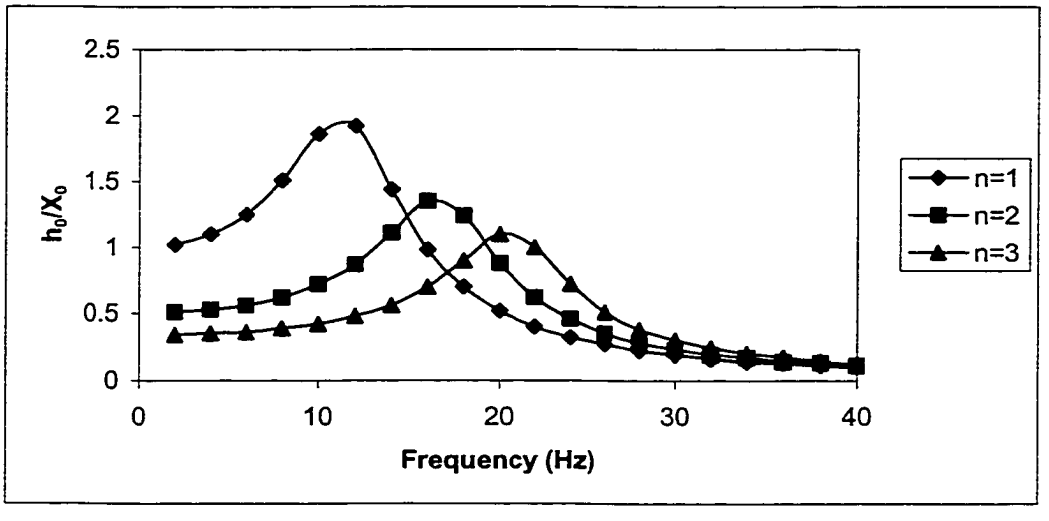

Figure 4.5. h_0/X_0 vs. Frequency for Various Number of Inertia Tracks

n-Effect on the Fluid Pressure Difference

Substituting equation 4.5 into equation 4.2, the expression of the pressure difference P becomes

$$p = \left[\frac{k_v}{A} - \frac{nk_v{}^2 \left(\frac{a^2}{A^3} \right)}{nk_v \left(\frac{a}{A} \right)^2 - la\rho\omega^2 + iC_I\omega} \right] X_0 e^{i\omega t} \tag{4.15}$$

Let

$$P(\omega, X_0) = \left[\frac{k_v}{A} - \frac{nk_v{}^2 \left(\frac{a^2}{A^3} \right)}{nk_v \left(\frac{a}{A} \right)^2 - la\rho\omega^2 + iC_I\omega} \right] X_0 \tag{4.16}$$

Then

$$p = P(\omega, X_0) e^{i\omega t} \tag{4.17}$$

where $P(\omega, X_0)$ is the pressure amplitude.

Figure 4.6 presents plots of the pressure difference versus frequency for a mount displacement amplitude of 1 mm. It shows that the peak fluid pressure increases as the number of the inertia track increases.

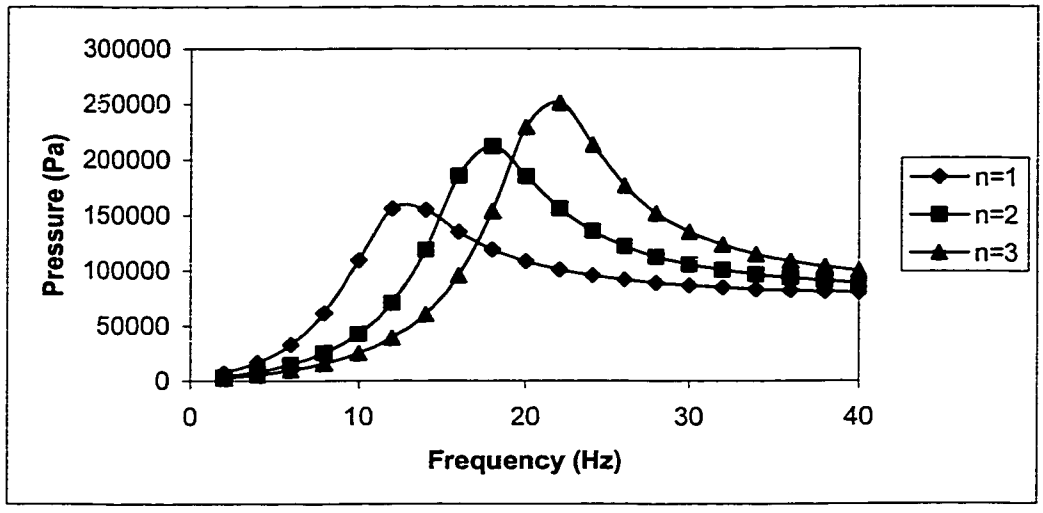

Figure 4.6. Pressure Difference vs. Frequency for Various Number of Inertia Tracks

n-Effect on Dynamic Stiffness and Loss Angle

Substituting equation 4.15 and the time derivative of the displacement input X (equation 3.1) into equation 3.7, the complex form of the dynamic stiffness becomes

$$k_d = k_s + iC_r\omega + k_v - \frac{nk_v^2\left(\frac{a}{A}\right)^2}{nk_v\left(\frac{a}{A}\right)^2 - la\rho\omega^2 + iC_l\omega} \tag{4.18}$$

Again, equation 4.18 can further be expressed as:

$$k_d = k' + ik'' \tag{4.19}$$

where

$$k' = k_s + k_v - \frac{nk_v^2\left(\frac{a}{A}\right)^2\left[nk_v\left(\frac{a}{A}\right)^2 - la\rho\omega^2\right]}{\left[nk_v\left(\frac{a}{A}\right)^2 - la\rho\omega^2\right]^2 + (C_l\omega)^2} \tag{4.20}$$

and

$$k'' = \frac{nk_v^2\left(\frac{a}{A}\right)^2 c_l\omega}{\left[nk_v\left(\frac{a}{A}\right)^2 - la\rho\omega^2\right]^2 + (C_l\omega)^2} + C_r\omega \tag{4.21}$$

The loss angle ϕ can then be obtained by

$$\phi = \tan^{-1}\left(\frac{k''}{k'}\right) \tag{4.22}$$

Figures 4.7 and 4.8 present plots of the dynamic stiffness and loss angle versus frequency for the hydromount with the parameters coming from the physical hydromount given in Chapter III. It shows that both the peak dynamic stiffness and loss angle increase when the number of the inertia tracks increase.

Rubber Damping Effect on Dynamic Properties

It was concluded in Chapter III that rubber damping has limited effect on the hydromount dynamic properties when $n = 1$. Following the same approach, the comparisons of the dynamic properties of the hydromount with and without rubber damping considered for $n = 2$ and 3 are plotted in Figure 4.9 and 4.10. It is seen that

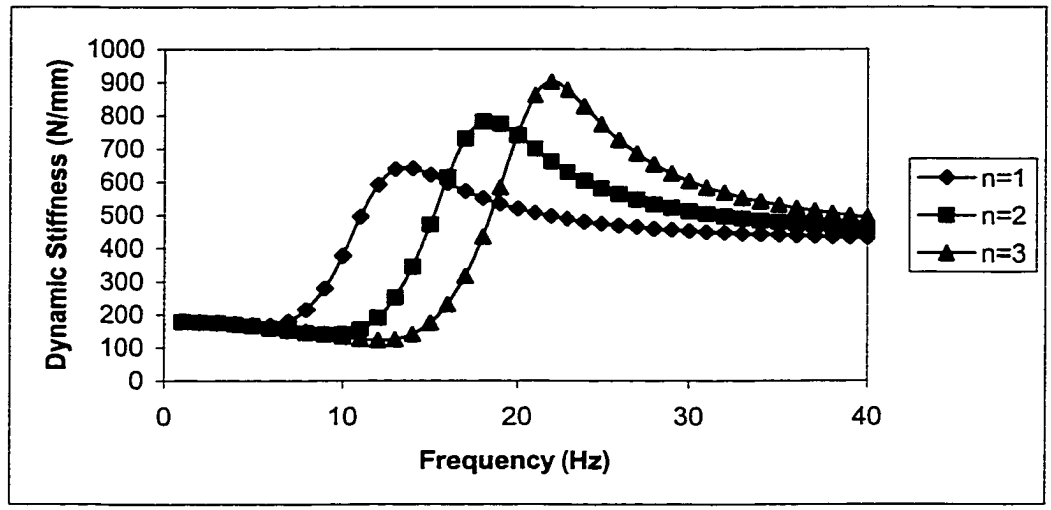

Figure 4.7. Dynamic Stiffness vs. Frequency for Various Number of Inertia Tracks

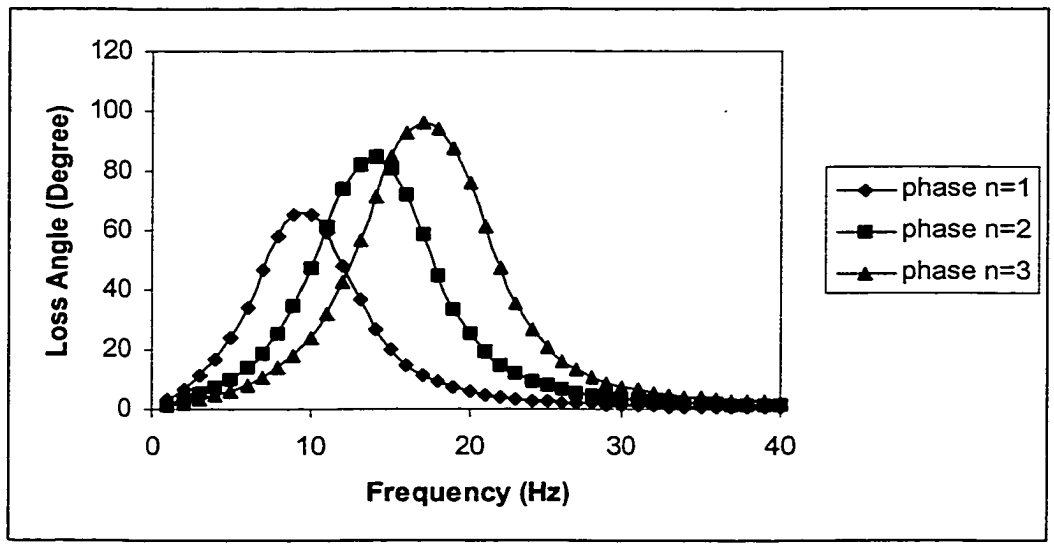

Figure 4.8. Loss Angle vs. Frequency for Various Number of Inertia Tracks

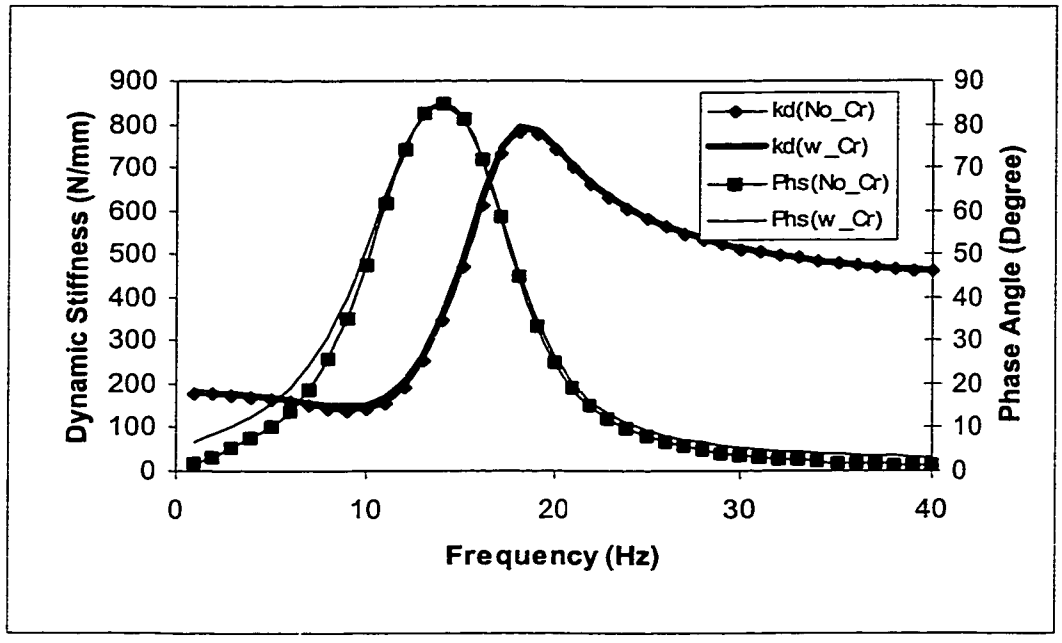

Figure 4.9. Comparison of Dynamic Properties of a Hydromount With and Without Rubber Damping Coefficient Considered ($n = 2$)

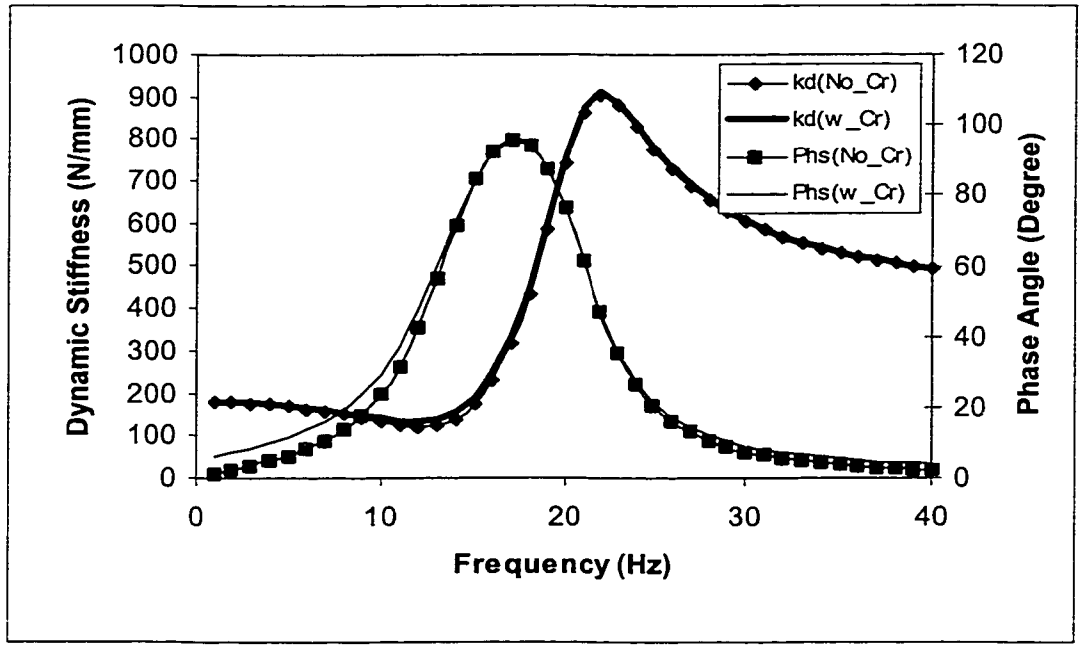

Figure 4.10. Comparison of Dynamic Properties of a Hydromount With and Without Rubber Damping Coefficient Considered ($n = 3$)

rubber damping has a limited effect also on the dynamic properties of the hydromount with two and three inertia tracks. This is true for the hydromounts with more than three inertia tracks as well.

Therefore, equation 4.18 can be re-written as

$$k_d = k_s + k_v - \frac{nk_v^2\left(\frac{a}{A}\right)^2}{nk_v\left(\frac{a}{A}\right)^2 - la\rho\omega^2 + iC_t\omega} \tag{4.23}$$

n-Effect on the Inertia Track Locking Mechanism

The inertia track locks at high frequencies for the hydromount with the single inertia track, which is discussed in Chapter III. Figure 4.11 presents plots of the third

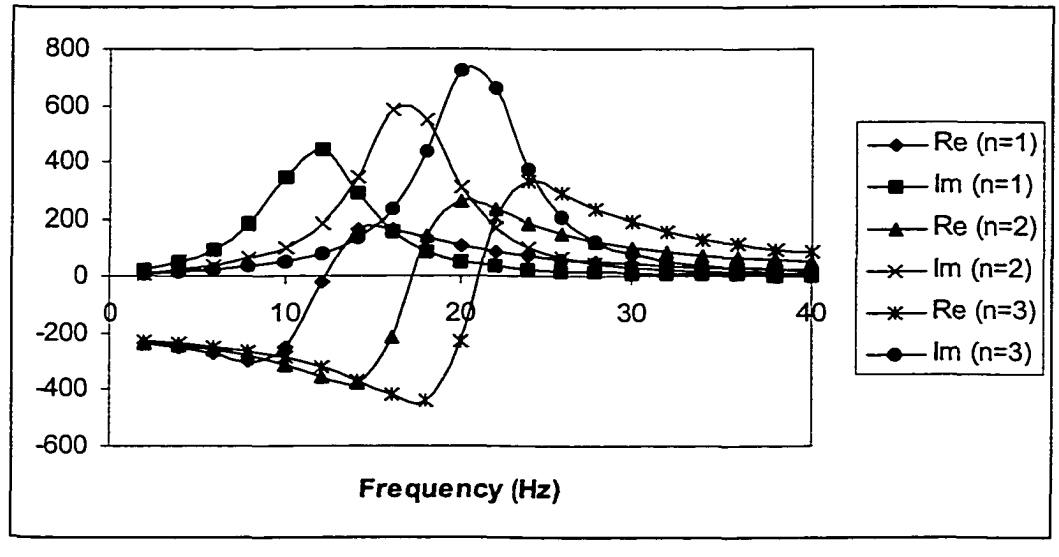

Figure 4.11. Plots of the Real and Imaginary Parts of Inertia Track Term

term on the right hand side of equation 4.29, which represents the inertia track effect on the dynamic properties. It is shown that both its real and imaginary parts approach very small values for high values of frequency. This indicates that the inertia track effectiveness diminishes at high frequencies, due to a practically locked inertia track. But more inertia tracks make the hydromount more difficult to lock, which is indicated by the relatively higher residual values of both the imaginary and real parts at the same frequency level.

n-Effect on the Frequency at Maximum Loss Angle

From equations 4.3 and 4.4, the damping ratio ζ of the inertia tracks is

$$\zeta = \frac{C_I \omega_n}{2nk_v}\left(\frac{A}{a}\right)^2 \tag{4.24}$$

Let β and k be the frequency ratio and the dynamic stiffness ratio as defined by equations 3.36 and 3.38, the dimensionless form of equation 4.23 is then expressed by

$$\frac{k_d}{k_v} = \frac{1}{k} - \frac{1-\beta^2}{\left(1-\beta^2\right)^2 + (2\zeta\beta)^2} + \frac{2\zeta\beta}{\left(1-\beta^2\right)^2 + (2\zeta\beta)^2} i \tag{4.25}$$

Therefore, the loss angle can be expressed by

$$\tan\phi = \frac{2k\zeta\beta}{\left(1-\beta^2\right)^2 + (2\zeta\beta)^2 - k\left(1-\beta^2\right)} \tag{4.26}$$

It is seen that equation 4.26 is the same as equation 3.36, which was derived from the single track hydromount model. Therefore, the conclusion drawn from the single track

hydromount, that the maximum loss angle occurs near the fluid resonance of inertia track, is also valid for the hydromounts with n inertia tracks. However, the inertia track fluid resonant frequency ω_n for the multiple track hydromount equals to the square root of the track number n times the resonant frequency with a single track, therefore, equation 4.24 becomes

$$\xi_{n\,\text{track}} = \frac{\xi_{\text{single\_track}}}{\sqrt{n}} \tag{4.27}$$

It indicates that the damping ratio of a hydromount with n tracks is smaller than the damping ratio of the hydromount with the single track. This results in the fact that the maximum loss angle of the hydromount with multiple tracks is closer to the fluid resonant frequency than the hydromount with the single track (see Figure 3.7).

Conclusion

A hydromount with more than one identical inertia track has an inertia track fluid resonance frequency which is equal to the square roots of the inertia track number n times the fluid resonant frequency of a similar hydromount with a single inertia track. For larger inertia track number n, the magnitudes of the fluid displacement in the inertia track and the equivalent piston displacement decrease. The pressure difference between the chambers increases when the inertia track number increases. Both the peak dynamic stiffness and loss angle increase when the number of the inertia track increases. Rubber damping has a minimal effect on the dynamic properties of hydromounts with multiple tracks. The inertia tracks for the hydromount with multiple tracks also lock at high frequencies, but the locking effectiveness decreases by the increase of the inertia track

numbers. The maximum loss angle occurs near the point where the fluid in the inertia track resonates. The more the inertia tracks, the closer are the frequencies at the maximum loss angle and the fluid resonance.

Hydromount with Two Non-identical Inertia Tracks

It gets more complicated mathematically, even though it is possible, to analyze the non-identical inertia tracks with more than two non-identical inertia tracks. Therefore, the following research is focused on the hydromount with two non-identical inertia tracks.

The hydromount model with two non-identical inertia tracks, at which one has the length l_1 and its cross-sectional area a_1, the other has l_2 and a_2, is shown in Figure 4.12.

For the inertia track #1, the equation of motion is:

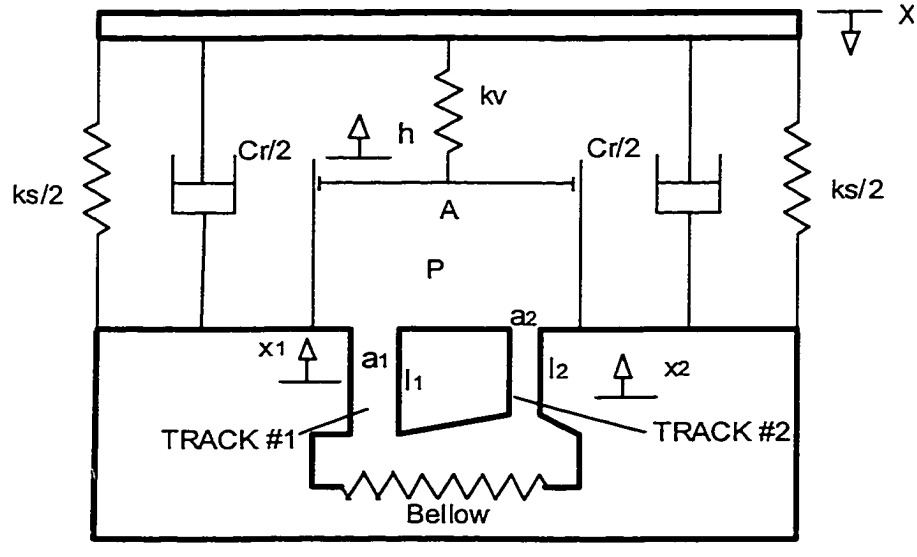

Figure 4.12. Hydromount Model for Two Non-identical Inertia Tracks

$$l_1 a_1 \rho \frac{d^2 x_1}{dt^2} + C_{I1} \frac{dx_1}{dt} = p a_1 \tag{4.28}$$

For the inertia track #2, the equation of motion is:

$$l_2 a_2 \rho \frac{d^2 x_2}{dt^2} + C_{I2} \frac{dx_2}{dt} = p a_2 \tag{4.29}$$

The volume conservation equation is

$$hA = x_1 a_1 + x_2 a_2 \tag{4.30}$$

The equivalent piston balance equation is

$$k_v (X - h) = pA \tag{4.31}$$

The resultant force F on the outer metal is

$$F = k_s X + pA \tag{4.32}$$

It is noticed that rubber damping force is ignored based on the conclusion drawn by the previous chapters, which states that the rubber damping has limited effect on the hdyrmount dynamic properties. It is assumed that this conclusion is also valid for the hydromount with non-identical inertia tracks.

Inertia Track Fluid Governing Equations

From equation 4.30,

$$h = \frac{x_1 a_1 + x_2 a_2}{A} \tag{4.33}$$

Substituting h from equation 4.33 into equation 4.31, the pressure difference becomes

$$p = \frac{k_v}{A}\left(X - \frac{x_1 a_1 + x_2 a_2}{A} \right) \tag{4.34}$$

Substituting equation 4.34 into equation 4.32 gives

$$l_1 a_1 \rho \frac{d^2 x_1}{dt^2} + C_{f1} \frac{dx_1}{dt} + k_v \left(\frac{a_1}{A} \right)^2 x_1 + k_v \left(\frac{a_1 a_2}{A^2} \right) x_2 = k_v \left(\frac{a_1}{A} \right) X \tag{4.35}$$

Equation 4.35 is the governing equation of the fluid in the inertia track #1. Following the same approach, the governing equation of the fluid in the inertia track #2 is:

$$l_2 a_2 \rho \frac{d^2 x_{21}}{dt^2} + C_{f2} \frac{dx_2}{dt} + k_v \left(\frac{a_2}{A} \right)^2 x_2 + k_v \left(\frac{a_1 a_2}{A^2} \right) x_1 = k_v \left(\frac{a_2}{A} \right) X \tag{4.36}$$

Inertia Track Fluid Resonant Frequencies

It is seen that the governing equations of the fluid in two inertia tracks are coupled. It is easier to use the matrix format as

$$[M]\{\ddot{x}\} + [C]\{\dot{x}\} + [K]\{x\} = \{F\} \tag{4.37}$$

where $[M]$, $[C]$, $[K]$ and $\{F\}$ are mass matrix, damping matrix, stiffness matrix and force matrix, whose

$$[M]=\begin{bmatrix} l_1 a_1 \rho & 0 \\ 0 & l_2 a_2 \rho \end{bmatrix} \tag{4.38}$$

$$[C]=\begin{bmatrix} C_{f1} & 0 \\ 0 & C_{f2} \end{bmatrix} \tag{4.39}$$

$$[K]=\begin{bmatrix} k_v\left(\frac{a_1}{A}\right)^2 & k_v\left(\frac{a_1 a_2}{A^2}\right) \\ k_v\left(\frac{a_1 a_2}{A^2}\right) & k_v\left(\frac{a_2}{A}\right)^2 \end{bmatrix} \tag{4.40}$$

$$\{F\}=\begin{bmatrix} k_v\left(\frac{a_1}{A}\right)X \\ k_v\left(\frac{a_2}{A}\right)X \end{bmatrix} \tag{4.41}$$

The characteristic equation can be written as

$$\left|[K]-\omega_n{}^2[M]\right|=0 \tag{4.42}$$

Expansion of equation 4.42 leads to

$$(l_1 a_1 \rho)(l_2 a_2 \rho)\omega_n^4 - \left[k_v\left(\frac{a_1}{A}\right)^2 (l_2 a_2 \rho) + k_v\left(\frac{a_2}{A}\right)^2 (l_1 a_1 \rho)\right]\omega_n^2 = 0 \tag{4.43}$$

The real solution of equation 4.43 is

$$\omega_n = \frac{1}{A}\sqrt{\frac{k_v}{\rho}\frac{(l_1 a_1 + l_2 a_2)}{l_1 l_2}} \tag{4.44}$$

This indicates that only one peak will be seen in the dynamic characteristic curve of the hydromount with non-identical inertia tracks because there is only one non-zero resonant frequency.

When

$$l_1 = l_2 = l \tag{4.45}$$

and

$$a_1 = a_2 = a \tag{4.46}$$

Eq.(4.46) becomes

$$\omega_{n2} = \frac{1}{A}\sqrt{\frac{2k_v a}{l\rho}} \tag{4.47}$$

which is identical to equation 4.7.

Another special case that the two same length inertia tracks have

$$a_1 = 2a_2 \tag{4.48}$$

then there is

$$\omega_{n2} = \frac{1}{A}\sqrt{\frac{3k_v a_2}{l\rho}} \tag{4.49}$$

which is equivalent to the hydromount with three identical inertia tracks according to equation 4.4.

Fluid Displacements in Inertia Tracks

The fluid displacements in inertia tracks x_1 and x_2 are the solutions of equation 4.37, which is

$$\{x\} = \left([K] - \omega^2[M] + i\omega[C]\right)^{-1}\{F\} \tag{4.50}$$

where

$$\{x\} = \begin{Bmatrix} x_1 \\ \\ x_2 \end{Bmatrix} \tag{4.51}$$

Let Z be

$$Z = \left([K] - \omega^2[M] + i\omega[C]\right) \tag{4.52}$$

Therefore,

$$Z = \begin{bmatrix} k_v\left(\frac{a_1}{A}\right)^2 - \frac{k_v a_1}{A^2}\frac{(l_1 a_1 + l_2 a_2)}{l_2} + ic_{l1}\omega & k_v\left(\frac{a_1 a_2}{A^2}\right) \\ k_v\left(\frac{a_1 a_2}{A^2}\right) & k_v\left(\frac{a_2}{A}\right)^2 - \frac{k_v a_2}{A^2}\frac{(l_1 a_1 + l_2 a_2)}{l_1} + ic_{l2}\omega \end{bmatrix} \tag{4.53}$$

and

$$Z^{-1} = \frac{\begin{bmatrix} Z_{11} & Z_{21} \\ Z_{12} & Z_{22} \end{bmatrix}}{|Z|} \tag{4.54}$$

where

$$Z_{11} = k_v\left(\frac{a_2}{A}\right)^2 - \frac{k_v a_2}{A^2}\frac{(l_1 a_1 + l_2 a_2)}{l_1} + ic_{I2}\omega \tag{4.55}$$

$$Z_{12} = Z_{21} = -k_v\left(\frac{a_1 a_2}{A^2}\right) \tag{4.56}$$

$$Z_{22} = k_v\left(\frac{a_1}{A}\right)^2 - \frac{k_v a_1}{A^2}\frac{(l_1 a_1 + l_2 a_2)}{l_2} + ic_{I1}\omega \tag{4.57}$$

$$|Z| = Z' + iZ'' \tag{4.58}$$

and furthermore

$$Z' = -\frac{{k_v}^2 a_1 a_2}{A^4}(l_1 a_1 + l_2 a_2)\left[\frac{a_1}{l_1} + \frac{a_2}{l_2} + \frac{l_1 a_1 + l_2 a_2}{l_1 l_2}\right] - c_{I1}c_{I2}\omega^2 \tag{4.59}$$

$$Z'' = \left[{a_1}^2 - \frac{a_1(l_1 a_1 + l_2 a_2)}{l_2}\right]c_{I2} + \left[{a_2}^2 - \frac{a_2(l_1 a_1 + l_2 a_2)}{l_1}\right]c_{I1} \tag{4.60}$$

Therefore,

$$\{x\} = \frac{1}{|Z|}\begin{Bmatrix} k_v\left(\frac{a_1}{A}\right)Z_{11}X + k_v\left(\frac{a_2}{A}\right)Z_{21}X \\ k_v\left(\frac{a_1}{A}\right)Z_{12}X + k_v\left(\frac{a_2}{A}\right)Z_{22}X \end{Bmatrix} \tag{4.61}$$

or

$$x_1 = \left[\left(\frac{a_1}{A}\right)\frac{Z_{11}}{|Z|} + \left(\frac{a_2}{A}\right)\frac{Z_{21}}{|Z|}\right]k_v X \tag{4.62}$$

and

$$x_2 = \left[\left(\frac{a_1}{A}\right)\frac{Z_{12}}{|Z|} + \left(\frac{a_2}{A}\right)\frac{Z_{22}}{|Z|}\right]k_v X \tag{4.63}$$

Dynamic Properties

Substituting equations 4.62 and 4.63 into equation 4.34

$$p = \frac{k_v}{A}X - \frac{k_v^{\,2}}{A^3}\left[a_1^{\,2}\frac{Z_{11}}{|Z|} + 2a_1a_2\frac{Z_{12}}{|Z|} + a_2^{\,2}\frac{Z_{22}}{|Z|}\right]X \tag{4.64}$$

Substituting equation 4.64 into equation 4.32

$$F = k_s X + k_v X - \frac{k_v^{\,2}}{A^2}\left[a_1^{\,2}\frac{Z_{11}}{|Z|} + 2a_1a_2\frac{Z_{12}}{|Z|} + a_2^{\,2}\frac{Z_{22}}{|Z|}\right]X \tag{4.65}$$

Equation 4.65 is divided by X at both sides,

$$k_d = k_s + k_v - \frac{k_v^2}{A^2}\left[a_1^2 \frac{Z_{11}}{|Z|} + 2a_1 a_2 \frac{Z_{12}}{|Z|} + a_2^2 \frac{Z_{22}}{|Z|}\right] \tag{4.66}$$

Conclusion

The hydromount with two non-identical inertia tracks exhibits one fluid resonant frequency, which is the function of the geometrical parameters of each inertia track (length and cross-sectional area) along with the equivalent piston area, volumetric stiffness and the fluid density. It is possible, even though it is complicated, to calculate the fluid displacements in the inertia tracks and the dynamic properties of the hydromount with two non-identical inertia tracks.

Summary

The hydromount with multiple inertia tracks has been studied. A hydromount with identical inertia tracks exhibits the inertia track fluid resonance frequency equal to the square roots of the inertia track number n times the fluid resonant frequency of the single track hydromount. An increase of the inertia track number n, the magnitude of the fluid displacement in the inertia track and the equivalent piston displacement decrease. The pressure difference between the chambers increases when the inertia track number increases. Both the peak dynamic stiffness and loss angle increase when the number of the inertia track increases. Rubber damping has a minimal effect on the hydromount dynamic properties for those hydromounts with multiple identical tracks. The multiple identical inertia tracks also lock at high frequencies, but the locking effectiveness decreases with the increase of the inertia track number. The maximum loss angle occurs

near the point where the fluid in the inertia track resonates. The more the inertia tracks, the closer the frequency the maximum loss angle and the fluid resonant frequency. The hydromount with non-identical inertia tracks also exhibits one fluid resonant frequency, which is a function of the geometrical parameters of each inertia track along with the equivalent piston area, volumetric stiffness and the fluid density. The dynamic properties of the hydromount with non-identical inertia tracks are mathematically predictable, though complicated.

Figure 4.13 illustrates that the dynamic characteristics of the hydromount with multiple inertia tracks are predictable theoretically with the assumed inertia track damping coefficient.

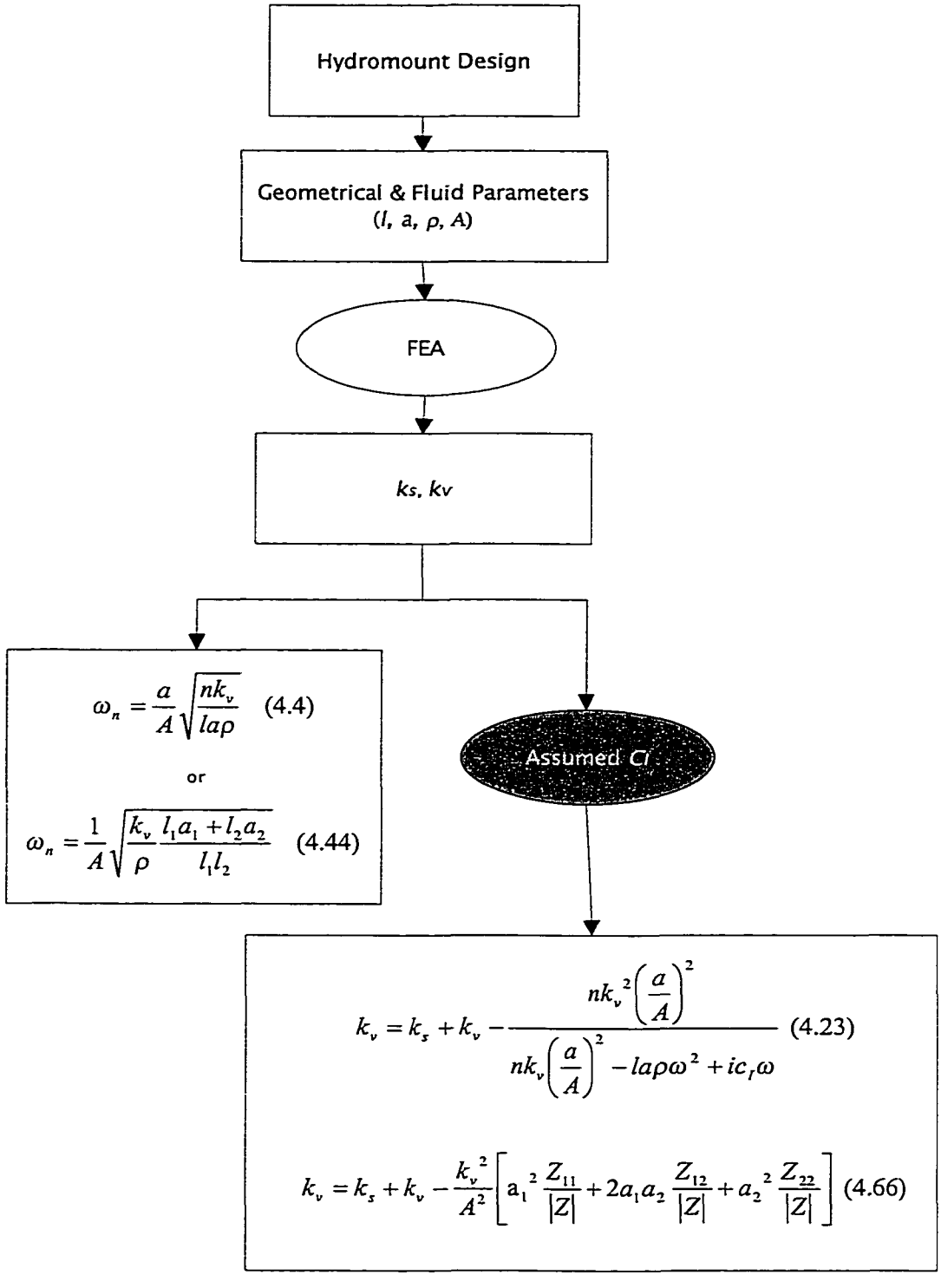

Figure 4.13. The Dynamic Characteristic Prediction Procedure of the Hydromount With Multiple Inertia Tracks

CHAPTER V

INERTIA TRACK DAMPING MECHANISM

The hydromount model with the lumped inertia track damping coefficient (C_I) was studied in the previous chapters. Without knowing the damping mechanism of the inertia track the practical application of the theory is limited. This chapter is devoted to the inertia track damping mechanism study based on the assumption that the flow inside the inertia track is an oscillating laminar flow. At the end of this chapter, the theory is verified by comparing with test results for two hydromounts.

Fundamental Equations

It is assumed that the inertia track is circular with radius R and length l and the pressure difference between the two open ends is p. Denoting the coordinate in the direction of the axis of the inertia track by x, and the radial distance from it by r, the equation of continuity is then

$$\frac{\partial u}{\partial x}+\frac{\partial v}{\partial r}+\frac{v}{r}=0 \tag{5.1}$$

where u and v are the velocity components in the x and r directions, respectively.

The axisymmetric Navier-Stokes equations are

$$\frac{\partial u}{\partial t}+u\frac{\partial u}{\partial x}+v\frac{\partial u}{\partial r}=-\frac{1}{\rho}\frac{\partial p}{\partial x}+\gamma\left(\frac{\partial^2 u}{\partial x^2}+\frac{\partial^2 u}{\partial r^2}+\frac{1}{r}\frac{\partial u}{\partial r}\right) \tag{5.2}$$

$$\frac{\partial v}{\partial t}+u\frac{\partial v}{\partial x}+v\frac{\partial v}{\partial r}=-\frac{1}{\rho}\frac{\partial p}{\partial r}+\gamma\left(\frac{\partial^2 v}{\partial x^2}+\frac{\partial^2 v}{\partial r^2}+\frac{1}{r}\frac{\partial v}{\partial r}-\frac{v}{r^2}\right) \tag{5.3}$$

where γ is the kinematic viscosity.

For an axial flow appoximation ($v = 0$) the equation of continuity is

$$\frac{\partial u}{\partial x}=0 \tag{5.4}$$

Substituting $v = 0$ into equation 5.3 yields:

$$\frac{\partial p}{\partial r}=0 \tag{5.5}$$

which shows that the pressure is uniform across the section of the inertia track and

$$p = p(x,t) \tag{5.6}$$

The equation of motion (equation 5.2) is then converted into

$$\frac{\partial u}{\partial t}=-\frac{1}{\rho}\frac{\partial p}{\partial x}+\gamma\left(\frac{\partial^2 u}{\partial r^2}+\frac{1}{r}\frac{\partial u}{\partial r}\right) \tag{5.7}$$

Assuming that the pressure is linearly decreasing along the x axis, and differentiating equation 3.20 with respect to x,

$$\frac{\partial p}{\partial x}=-\frac{P(\omega,X_0)}{l}e^{i\omega t} \tag{5.8}$$

where $P(\omega, X_0)$ is expressed by equation 3.24.

Then

$$-\frac{1}{\rho}\frac{\partial p}{\partial x}=\frac{P(\omega,X_0)}{\rho l}e^{i\omega t}=qe^{i\omega t} \tag{5.9}$$

where

$$q=\frac{P(\omega,X_0)}{\rho l} \tag{5.10}$$

Assuming harmonic dependence as t

$$u(r,t)=f(r)e^{i(\omega t+\phi)} \tag{5.11}$$

yields

$$\frac{\partial u}{\partial r}=f'(r)e^{i(\omega t+\phi)} \tag{5.12}$$

$$\frac{\partial^2 u}{\partial r^2}=f''(r)e^{i(\omega t+\phi)} \tag{5.13}$$

$$\frac{\partial u}{\partial t}=i\omega f(r)e^{i(\omega t+\phi)} \tag{5.14}$$

Substituting equations 5.9, 5.12, 5.13 and 5.14 into equation 5.7,

$$f''(r)+\frac{1}{r}f'(r)-\frac{i\omega}{\gamma}f(r)=\frac{q}{\gamma}e^{-i\phi} \tag{5.15}$$

For the homogeneous equation

$$f_h''(r)+\frac{1}{r}f_h'(r)-\frac{i\omega}{\gamma}f_h(r)=0 \tag{5.16}$$

Let's introduce a similarity variable as

$$z=r\sqrt{\frac{-i\omega}{\gamma}} \tag{5.17}$$

Then by chain rule of differentiation

$$f'(r)=\frac{\partial f}{\partial z}\frac{\partial z}{\partial r}=f'(z)\sqrt{\frac{-i\omega}{\gamma}} \tag{5.18}$$

$$f''(r)=\frac{\partial f'}{\partial z}\frac{\partial z}{\partial r}=f''(z)\left(\sqrt{\frac{-i\omega}{\gamma}}\right)^2 \tag{5.19}$$

Substituting equations 5.18 and 5.19 into equation 5.16 gives

$$f_h''(z)+\frac{1}{z}f_h'(z)+f_h(z)=0 \tag{5.20}$$

Equation 5.20 is a Bessel equation of first kind of order zero. Its solution of equation 5.20 is given by (Kreyszig, 1993)

$$f_h(r)=c_1J_0\left(r\sqrt{\frac{-i\omega}{\gamma}}\right)+c_2Y_0\left(r\sqrt{\frac{-i\omega}{\gamma}}\right) \tag{5.21}$$

where c_1 and c_2 are constants and J_0 and Y_0 are the first and second kind of Bessel functions of zero order, respectively.

For the particular solution of equation 5.15:

$$f_p''(r) = f_p'(r) = 0 \tag{5.22}$$

Then

$$\frac{i\omega}{\gamma} f_p(r) = \frac{q}{\gamma} e^{-i\phi} \tag{5.23}$$

$$f_p(r) = \frac{q}{i\omega} e^{-i\phi} \tag{5.24}$$

Therefore, the general solution of equation 5.15 becomes

$$f(r) = c_1 J_0\left(r\sqrt{\frac{-i\omega}{\gamma}}\right) + c_2 Y_0\left(r\sqrt{\frac{-i\omega}{\gamma}}\right) + \frac{q}{i\omega} e^{-i\phi} \tag{5.25}$$

The general solution of equation 5.7 is

$$u(r,t) = \left(c_1 J_0\left(r\sqrt{\frac{-i\omega}{\gamma}}\right) + c_2 Y_0\left(r\sqrt{\frac{-i\omega}{\gamma}}\right) + \frac{q}{i\omega} e^{-i\phi}\right) e^{i(\omega t+\phi)} \tag{5.26}$$

At the axis of the inertia track $r = 0$, $Y_0(0)$ is not finite. Because the velocity is finite at the center, the coefficient c_2 vanished.

No slip boundary condition dictates that $u(R,t) = 0$. Therefore, c_1 is

$$c_1 = -\frac{\frac{q}{i\omega}}{J_0\left(R\sqrt{\frac{-i\omega}{\gamma}}\right)} e^{-i\phi} \tag{5.27}$$

Hence, the solution of equation 5.7 becomes

$$u(r,t) = -\frac{P(\omega, X_0)}{i\rho l\omega}\left[1 - \frac{J_0\left(r\sqrt{\frac{-i\omega}{\gamma}}\right)}{J_0\left(R\sqrt{\frac{-i\omega}{\gamma}}\right)}\right]e^{i\omega t} \tag{5.28}$$

The mean velocity can be calculated as

$$u_m = \frac{2\pi}{a}\int_0^R u(r,t)rdr \tag{5.29}$$

where a is the cross-sectional area of the inertia track. Therefore

$$u_m = -\frac{2P(\omega, X_0)}{iR\rho l\omega}\left[\frac{R}{2} - \frac{J_1\left(R\sqrt{\frac{-i\omega}{\gamma}}\right)}{\sqrt{\frac{-i\omega}{\gamma}}J_0\left(R\sqrt{\frac{-i\omega}{\gamma}}\right)}\right]e^{i\omega t} \tag{5.30}$$

Inertia Track Damping Coefficient

The system differential equation is

$$m\frac{du_m}{dt} + C_I u_m - P(\omega, X_0)ae^{i\omega t} = 0 \tag{5.31}$$

where

m—Fluid mass in the inertia track, which equals to ρal;

C_I—Inertia track damping coefficient (lumped).

Substituting equation 5.30 and its derivative into equation 5.31 yields

$$C_I = \frac{\frac{1}{2} i\pi R^3 \rho l \omega}{\frac{1}{2}R - \frac{J_1\left(R\sqrt{\frac{-i\omega}{\gamma}}\right)}{\sqrt{\frac{-i\omega}{\gamma}}J_0\left(R\sqrt{\frac{-i\omega}{\gamma}}\right)}} - i\omega\rho\pi R^2 l \tag{5.32}$$

The real part of the above equation is the inertia track damping coefficient.

Figure 5.1 shows the plot of damping coefficient versus frequency for the parameters shown below

$$R = 500 \text{ mm}$$

$$l = 500 \text{ mm}$$

$$\gamma = 1.0\times10^{-6} \text{ m}^2/\text{s}$$

$$\rho = 1000 \text{ kg/m}^3$$

It is found that the higher the frequency, the higher the damping coefficient.

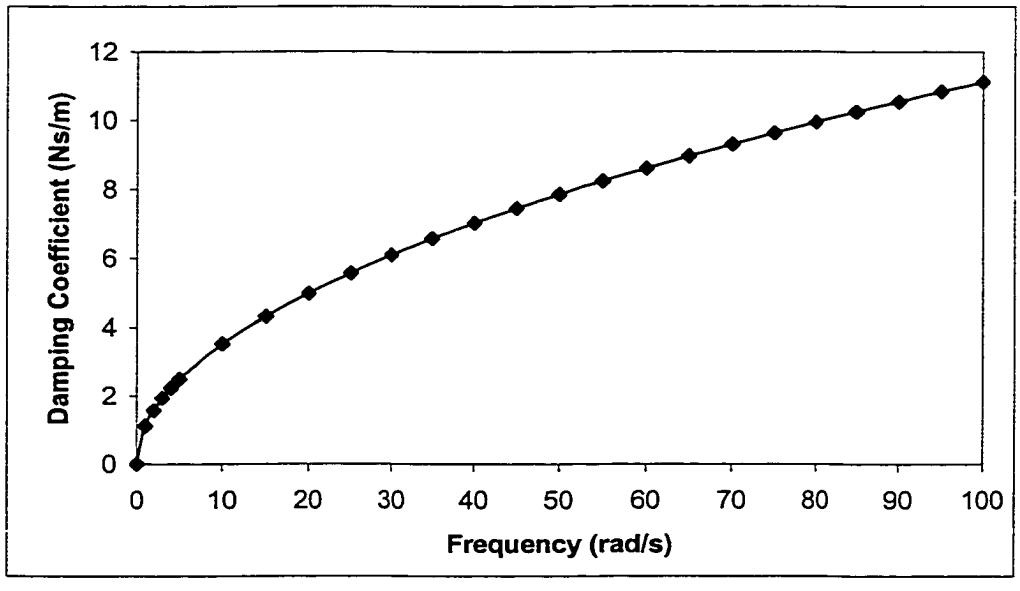

Figure 5.1. Inertia Track Damping Coefficient vs. Frequency

Composition of Inertia Track Damping Coefficient

To study the sources of the inertia track damping coefficient C_I, Newton's second law for the fluid in the inertia track

$$la\rho\dot{u}_m = (p - \Delta p)a \tag{5.33}$$

is employed, where the major contribution to Δp is the pressure loss caused by the friction (major head loss). Therefore, for a laminar flow (Potter, 1993)

$$\Delta p = f\frac{l}{D}\frac{u_m^{\,2}}{2}\rho \tag{5.34}$$

where f and D are the friction factor and the diameter of the inertia track, respectively.

Reynolds number Re is

$$\mathrm{Re} = \frac{u_m D}{\gamma} \tag{5.35}$$

(γ is the kinematic viscosity) and the relation between the friction factor f and Reynolds number Re is

$$f = \frac{64}{\mathrm{Re}} \tag{5.36}$$

Equation (5.34) then becomes

$$\Delta p = \frac{32\gamma l}{D^2}\rho u_m \tag{5.37}$$

Substituting equation (5.37) into equation (5.33) yields

$$la\rho\dot{u}_m + \frac{32\gamma l}{D^2}\rho a u_m = pa \tag{5.38}$$

Comparing equations (5.38) and (3.4) shows that

$$C_I = \frac{32\gamma l}{D^2}\rho a \tag{5.39}$$

or

$$C_I = 8\pi\gamma l\rho \tag{5.40}$$

Sensitivity Study

Equation 5.32 shows that the damping coefficient of the inertia track is a function of variables such as the inertia track radius, length, fluid viscosity and density. Changing each individual variable results in different inertia track damping coefficient. The trends of these changes are studied in this section.

Effect of Radius

The variation of damping coefficient versus frequency for R = 100, 200 and 500 mm while keeping l = 500 mm, and $\gamma = 10^{-6}$ m^2/s is shown in Figure 5.2. It is found that the larger the radius, the higher the damping coefficient.

Effect of Inertia Track Length

The variation of damping coefficient vs. frequency for l = 200, 350 and 500 mm while keeping R = 100 mm, and $\gamma = 10^{-6}$ m^2/s is shown in Figure 5.3. It is found that the longer the inertia track length, the higher the damping coefficient.

Effect of Viscosity

The variation of damping coefficient versus frequency for $\gamma = 10^{-7}$, 10^{-6} and 10^{-5} m^2/s while keeping R = 100 mm, l = 500 mm is shown in Figure 5.4. It is found that the higher the viscosity, the higher the damping coefficient.

Effect of Fluid Density

The variation of damping coefficient vs. frequency for ρ= 500, 1000 and 1500 kg/m^3 while keeping R = 100 mm, l = 500 mm and $\gamma = 10^{-6}$ is shown in Figure 5.5. It is found that the higher the fluid density, the higher the damping coefficient.

Conclusion

The damping coefficient of the inertia track filled with oscillating flow is a function of frequency. The higher the frequency, the higher the damping coefficient. It is also a function of the geometric variables and flow properties. The larger the inertia track diameter, the higher the damping coefficient; the longer the inertia track, the higher the damping coefficient; the more viscous the fluid, the higher the damping coefficient; the heavier the fluid, the higher the damping coefficient.

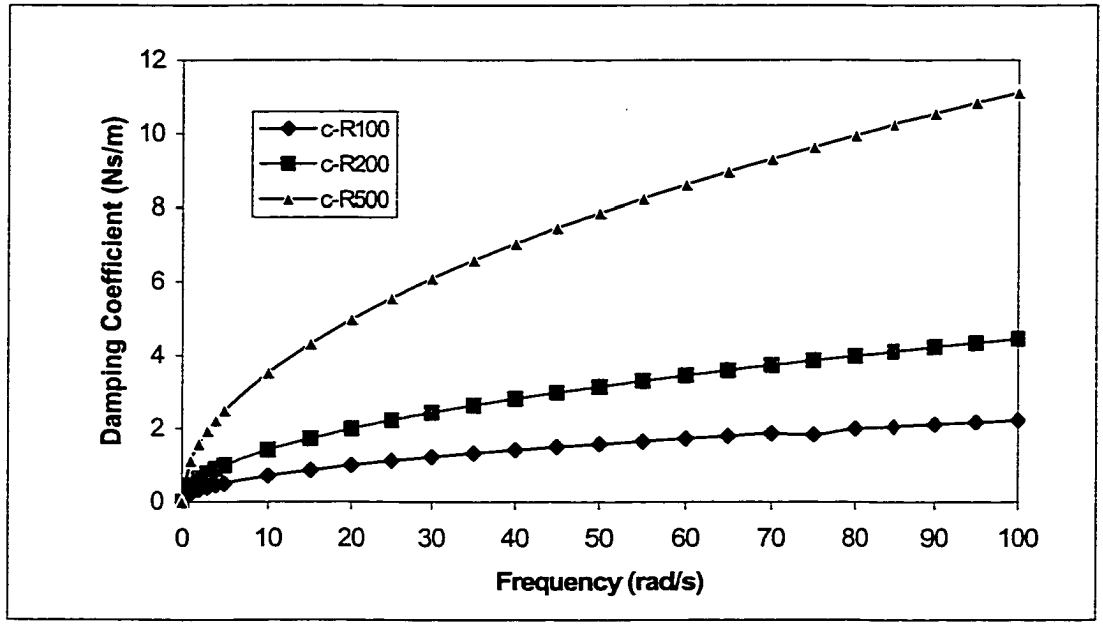

Figure 5.2. Inertia Track Damping Coefficient vs. Frequency for Various Radii

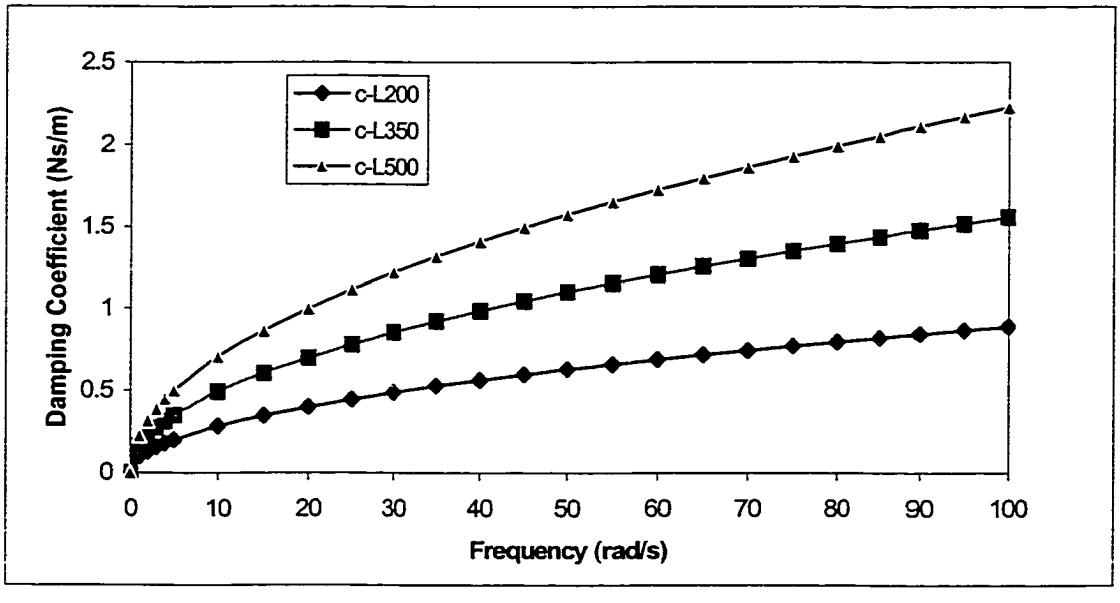

Figure 5.3. Inertia track Damping Coefficient vs. Frequency for Various Inertia Track Lengths

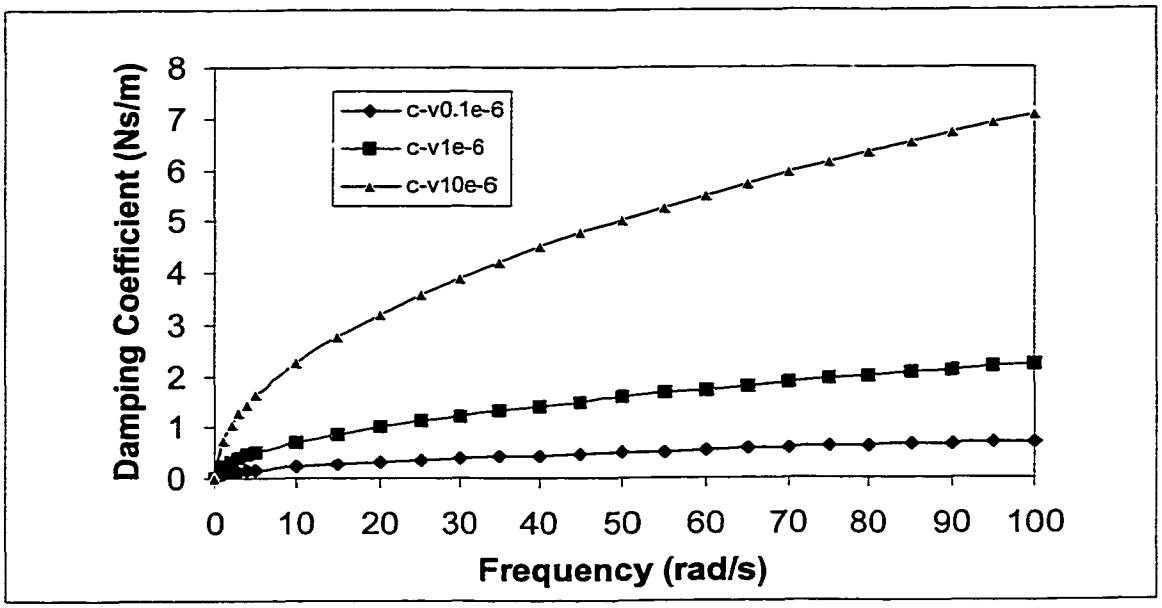

Figure 5.4. Inertia Track Damping Coefficient vs. Frequency for Various Viscosity

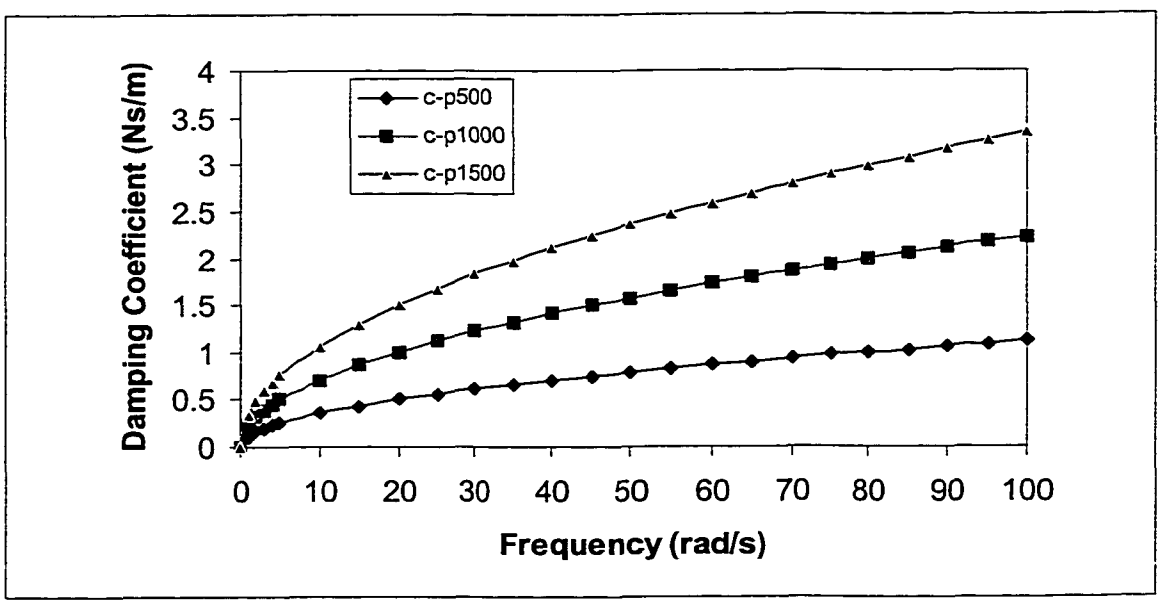

Figure 5.5. Inertia Track Damping Coefficient vs. Frequency for Various Fluid Densities

Experimental Verification

The hydromount mechanism and its related parameters have been studied so far. To verify the theory, two hydromounts were tested, and their dynamic characteristics are compared with the predicted results.

Equivalent Radius

Equation 5.32 was derived based on the configuration of a round straight inertia track. However the two hydromounts tested in this research have inertia tracks with rectangular cross-sections. In addition, the inertia track is curved and not straight. The conversion from the curved rectangular cross-section to the equivalent circular straight inertia track is accomplished approximately through the equivalent radius R_{eq} concept. Due to the fact that the damping force is proportional to the surface area, it is assumed that the perimeter of a rectangular section is equal to the equivalent circular perimeter. Then, the equivalent radius is expressed by

$$R_{eq} = (\frac{s+t}{\pi})b \tag{5.41}$$

where s and t are the lengths of the sides of the rectangle (see Figure 5.6) and b is the correction factor, which reflects to other factors not included by this research, such as the fluid energy loss when it enters and leaves inertia tracks etc. While reserving it for further study, an estimated value of 1.3 for the correction factor b is used in the following test comparisons.

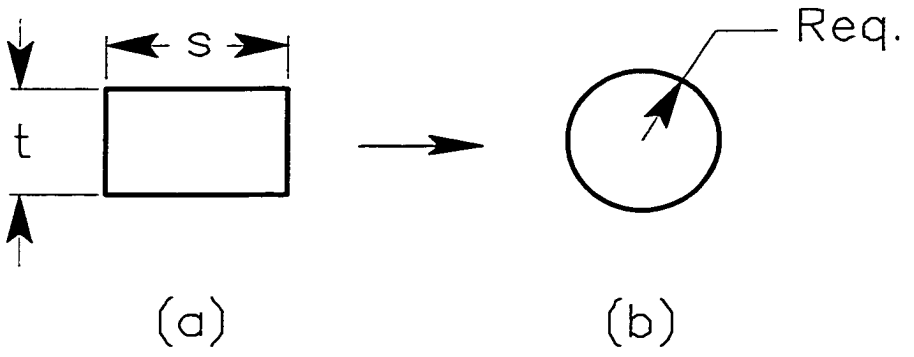

Figure 5.6. Schematic of Conversion From Rectangular Section to Circular Section

Hydromount I

This hydromount is the one given in Chapter III. Comparison of the calculated dynamic characteristics with those measured showed good correlation based on the assumed inertia track damping coefficient (see Figure 3.13). Figure 5.7 presents the inertia track damping coefficient versus frequency according to equation 5.32, for which the equivalent radius concept has been adopted. The damping data along with the parameters given above could be used by equation 3.15, and then the dynamic stiffness and loss angle are obtained as shown in Figure 5.8, along with the measured curves for comparison.

It is seen that the predicted and measured phase angles and resonant frequencies agree well, but the predicted peak dynamic stiffness is higher than the measured value.

Hydromount II

This hydromount exhibits the following parameters:

k_s = 180 N/mm;

k_v = 220 N/mm;

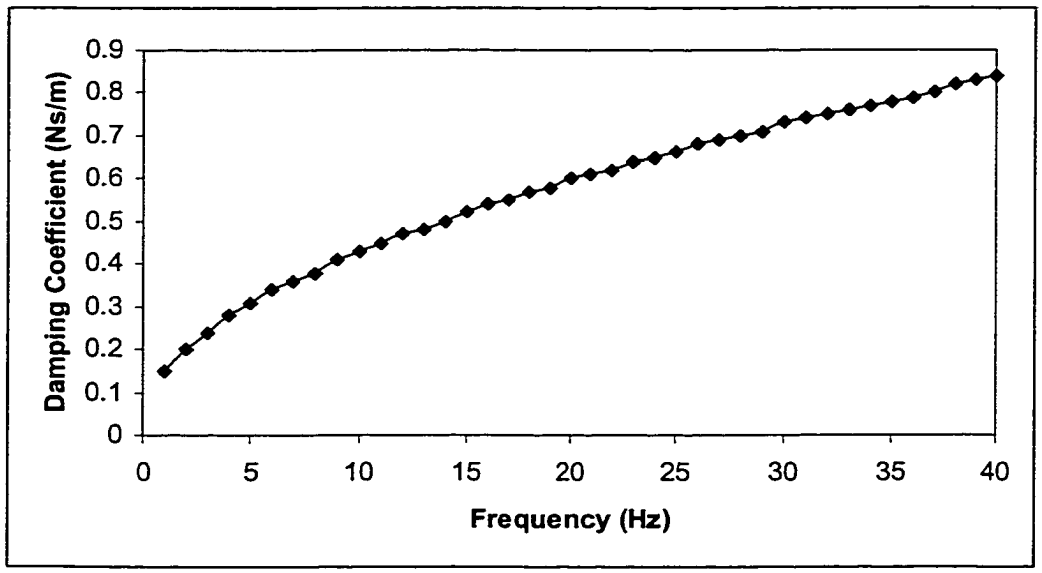

Figure 5.7. Inertia Track Damping Coefficient vs. Frequency for Hydromount I

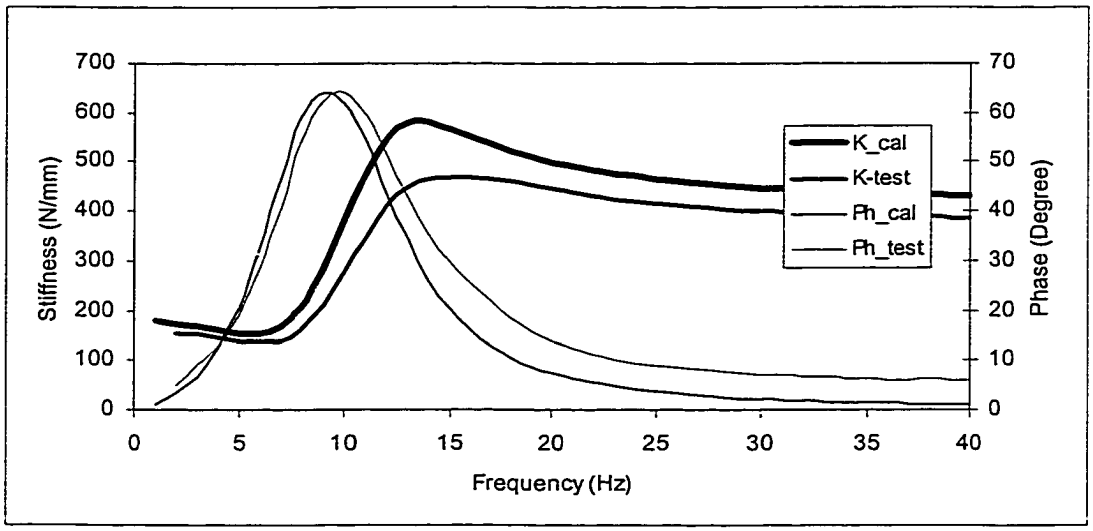

Figure 5.8. Comparison of Measured and Predicted Dynamic Stiffness and Phase Angle (Hydromount I)

$l = 180$ mm;

$a = 77$ mm^2;

$A = 3470$ mm^2;

$\rho = 10^{-6}$ kg/mm^3;

$s = 7$ mm;

$t = 11$ mm.

Its measured dynamic characteristics are shown in Figure 5.9. The variation of the inertia track damping coefficient versus frequency according to equation 4.32 is shown in Figure 5.10. The comparison of the tested and calculated dynamic stiffness and loss angle is shown in Figure 5.11. Again, the comparison shows that the predicted peak dynamic stiffness is higher than the measured value as well as the phase angle.

Discussion and Conclusion

By means of the equivalent radius concept, the predicted dynamic properties of the hydromounts agree reasonably well with the measured results. But the higher peak dynamic stiffness and phase indicates that the predicted value of the inertia track damping coefficient is lower than it should be. Because the inertia track damping coefficient is a function of inertia track radius R or the equivalent radius R_{eq}, and an increase in R or R_{eq} results in increase in inertia track damping coefficient, it is suggested that equation 5.41, which is based on pure assumption, may be underestimated. Further studies will be performed for this phenomenon.

Because the inertia track is not straight, it is possible that an equivalent inertia track length should be used in order to have a better correlation between the predicted and measured results. The parametric study in Chapter III shows that decreasing the

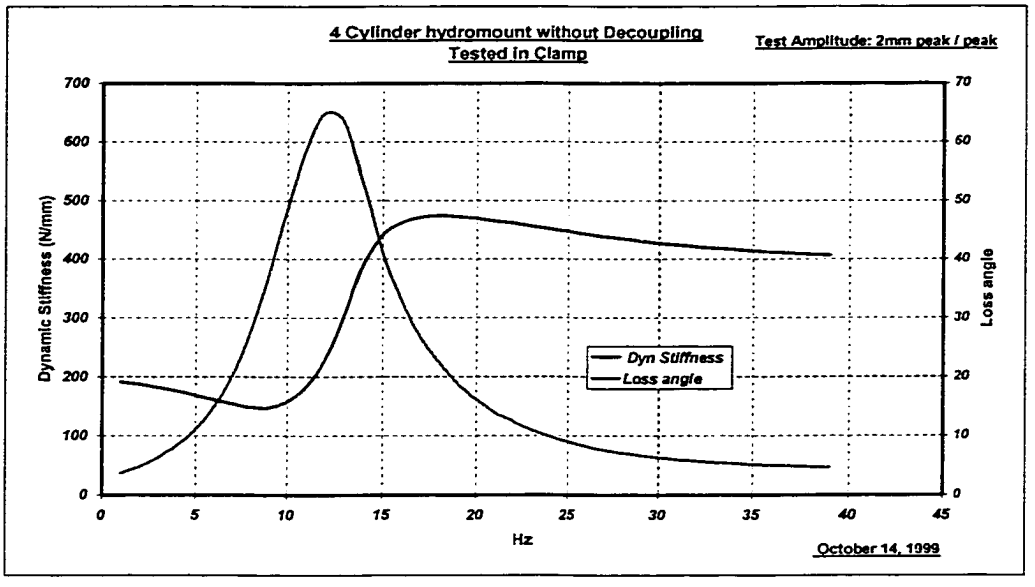

Figure 5.9. The Measured Dynamic Characteristics for Hydromount II

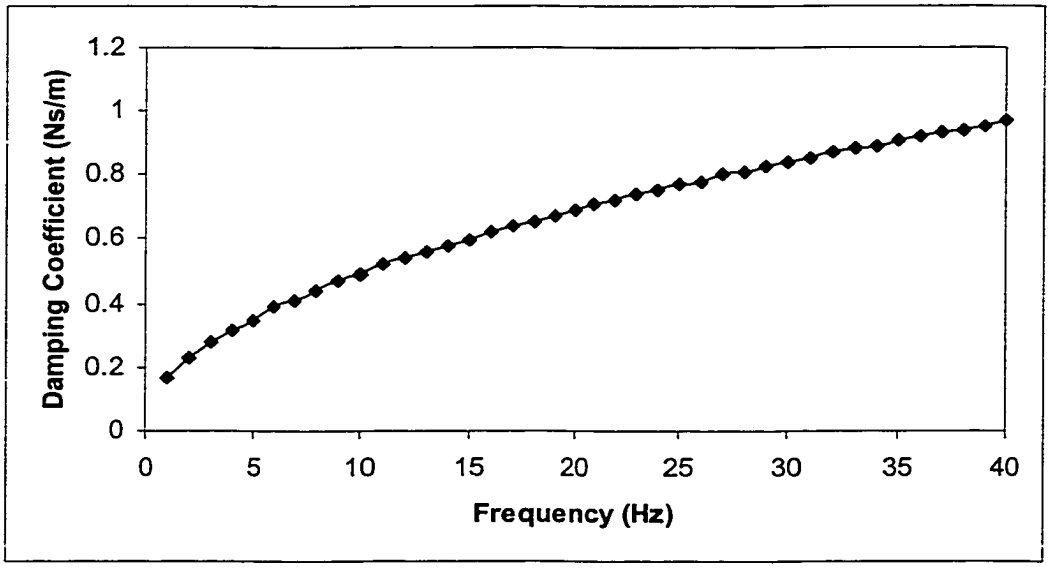

Figure 5.10. Inertia Track Damping Coefficient Versus Frequency Curve (Hydromount II)

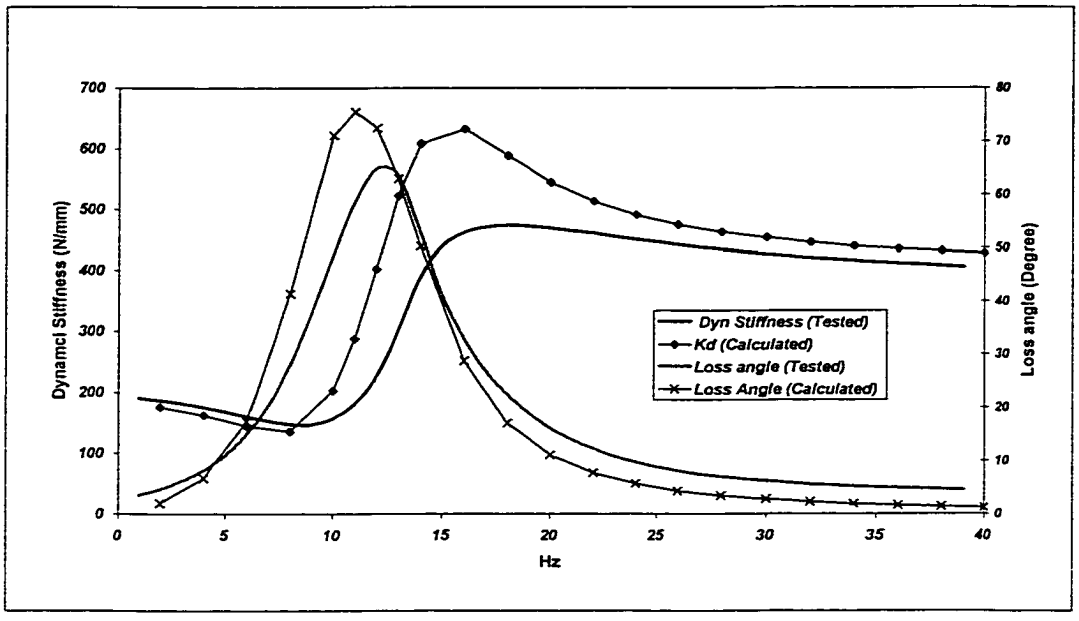

Figure 5.11. Comparison of Measured and Calculated Dynamic Stiffness and Phase Angle (Hydromount II)

inertia track length results in lower peaks for both dynamic stiffness and loss angle. If the equivalent inertia track length l_{eq} is shorter than l, for example:

$$l_{eq} = 0.9l \tag{5.42}$$

then a comparison of the inertia track damping coefficients for Hydromount II with full and equivalent lengths (see Figure 5.12) shows that the inertia track damping coefficient is lower for the shorter length, which agrees with the parametric study results shown in Figure 5.3. Plots of the dynamic characteristics of this hydromount with full and equivalent inertia track length ($0.9l$) are shown in Figure 5.13. It is seen that both peak dynamic stiffness and loss angle for the shorter length are higher than those for the longer length. This appears to contradict the parametric study results shown in Figures 3.27 and

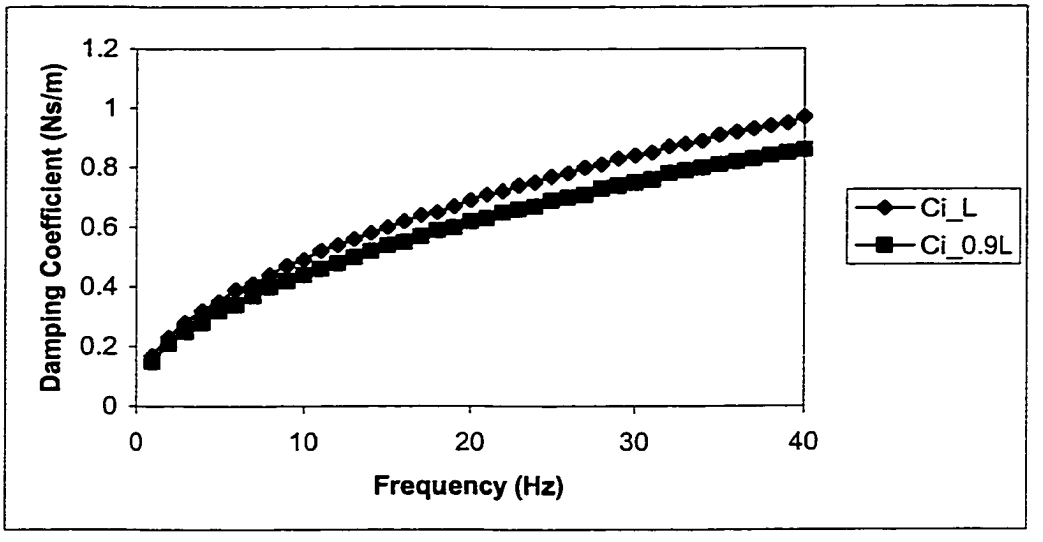

Figure 5.12. Inertia Track Damping Coefficients for Inertia Track With Full and Equivalent Lengths

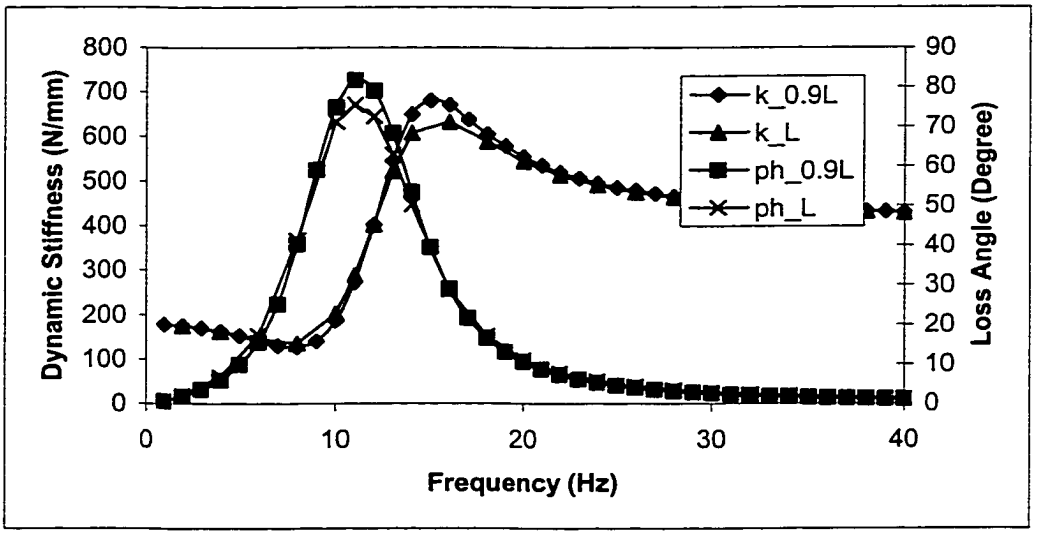

Figure 5.13. Comparison of Dynamic Characteristics of Hydromount II With Full and Equivalent Inertia Track Lengths

3.28, but there the inertia track damping coefficient C_I was held constant while here it is a function of the inertia track length.

Following the same procedure for the assumption of a longer equivalent inertia track length, for example:

$$l_{eq} = 1.1l \tag{5.43}$$

the comparison of the dynamic characteristics of Hydromount II for the equivalent inertia track lengths and its measured results is presented in Figures 5.14 and 5.15 along with the results for inertia track length l. The comparison shows that the lowered peaks for the dynamic stiffness and loss angle come in the expense of undesired frequency shift at the maximum loss angle. This indicates that further research is needed for better correlation.

Summary

The inertia track damping coefficient is a function of frequency along with other variables: inertia track equivalent radius, inertia track length and fluid density and its viscosity. An increase in frequency, radius, viscosity and density results in higher damping coefficient. Using the equivalent radius concept, the calculated dynamic properties of the hydromounts agree reasonably well with the measured results.

To update the procedure of the dynamic characteristic prediction of a hydromount by the research conducted so far, the gray filled ovals, which symbolized the unknown inertia track fluid damping coefficient C_I in Figures 3.49 and 4.13, are replaced by equation 5.32 (see Figure 5.12). It is seen that the goal of the research stated in Chapter I has been accomplished so far--a theory has been developed to predict the

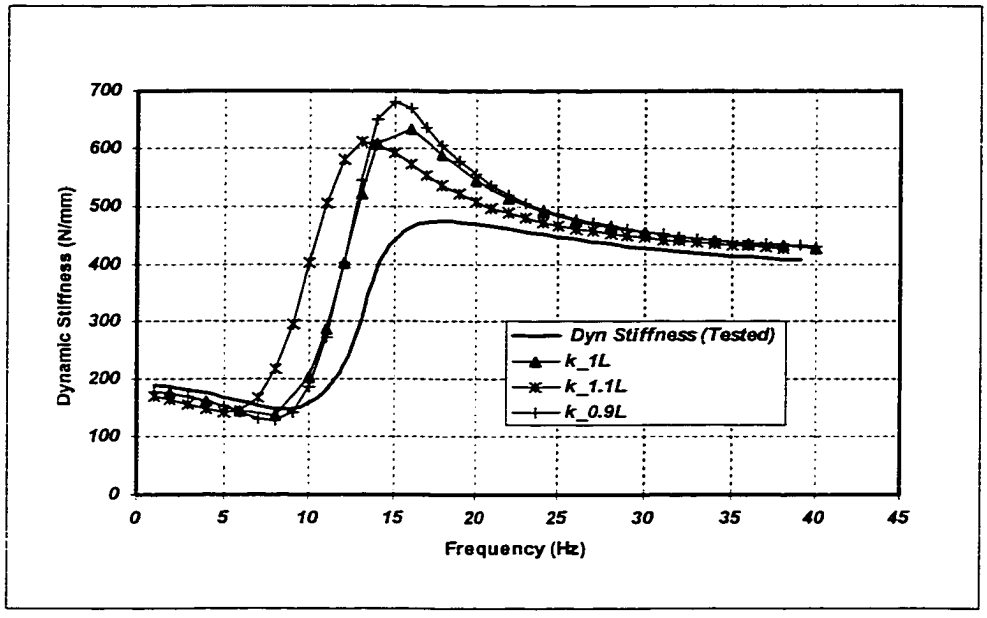

Figure 5.14. Comparison of Dynamic Stiffness of Hydromount II With Full and Equivalent Inertia Track Lengths to Test Results

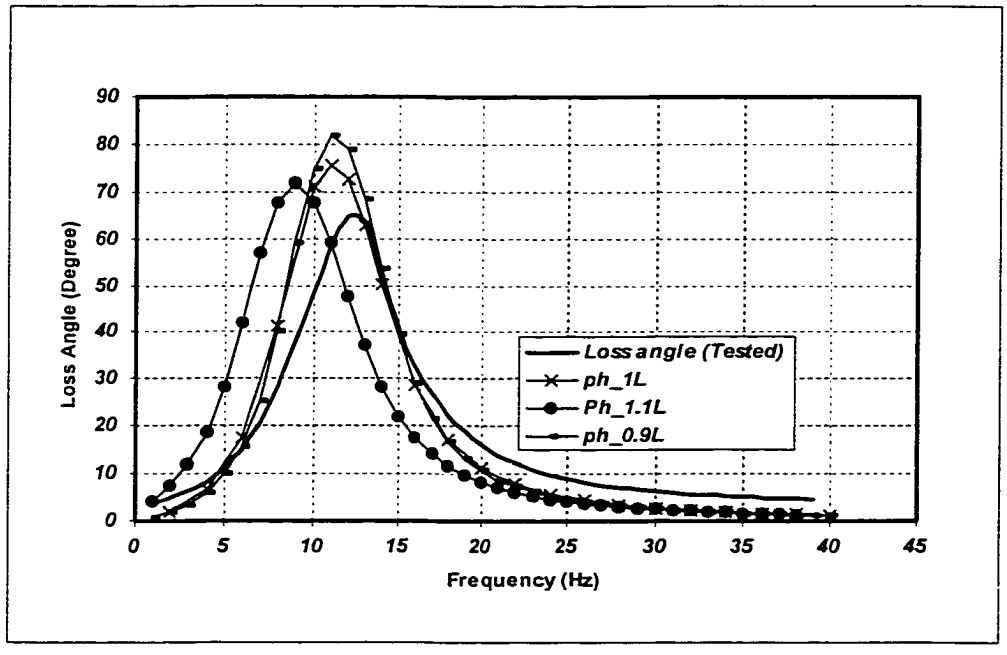

Figure 5.15. Comparison of Loss Angle of Hydromount II With Full and Equivalent Inertia Track Lengths to Test Results

dynamic characteristics of hydromounts based on the parameters which are determinable in the design stage.

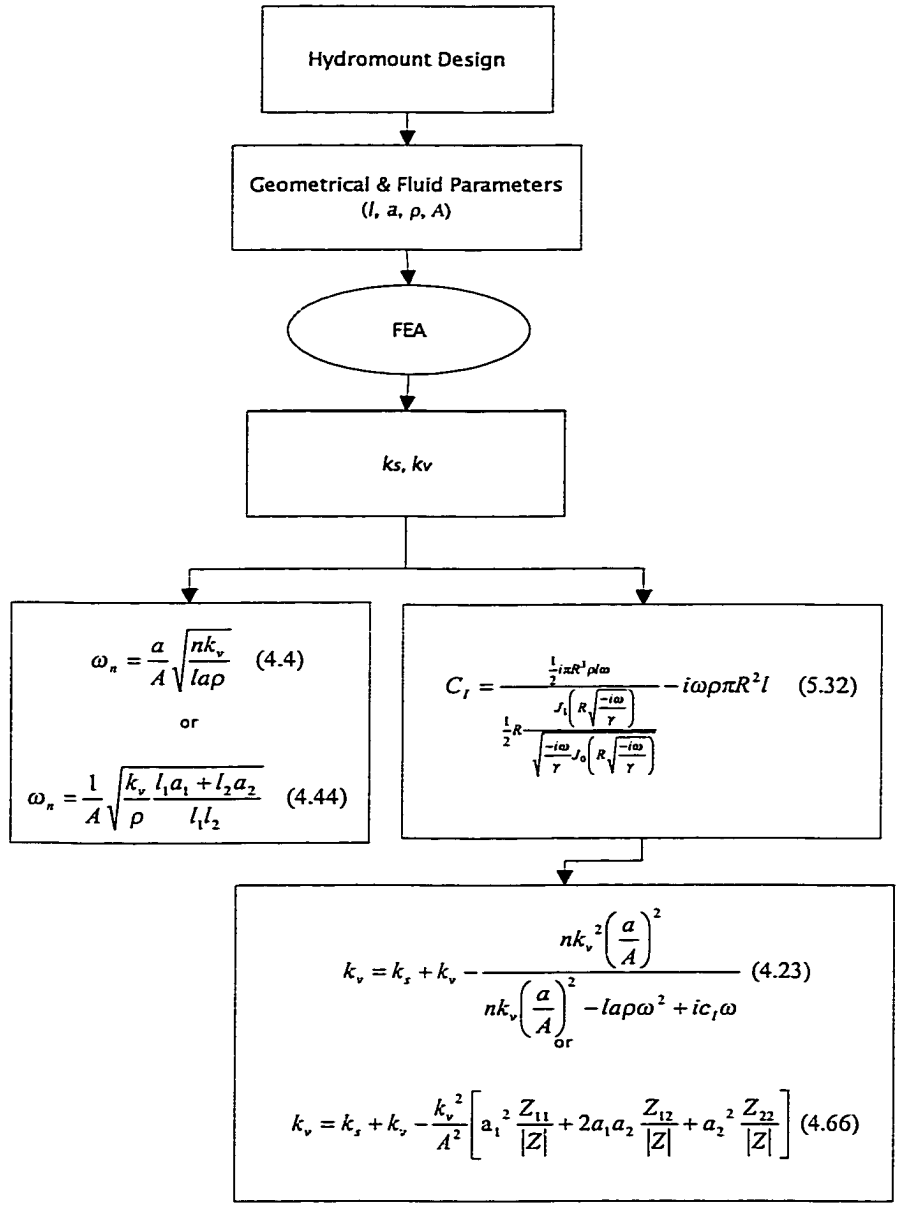

Figure 5.16. Dynamic Characteristics Prediction Procedure of Hydromounts With Design Determinable Parameters

CHAPTER VI

SUMMARY AND CONCLUSIONS

A procedure to predict the dynamic characteristics of the hydromount based on the design parameters was developed and verified experimentally. It is concluded that the dynamic characteristics of the hydromounts are related to the rubber static stiffness, rubber damping coefficient, volumetric stiffness and effectiveness of the oscillating fluid in the inertia track. At high frequencies, however, the fluid in the inertia track becomes inefficient so that the effect of fluid may be neglected. It is also concluded that the rubber damping has a minimal effect on the hydromount dynamic properties and may be neglected. The maximum loss angle, which corresponds to the maximum damping coefficient of the hydromount, occurs at a frequency close to the inertia track fluid resonant frequency. The degree of its closeness depends on the damping ratio and dynamic stiffness ratio. It was found by a parametric study that an increase in the rubber static stiffness results in an increase in the dynamic stiffness, but a decrease in the loss angle. Increases in the volumetric stiffness, fluid density, inertia track cross-sectional area and its length result in increases in the dynamic stiffness and loss angle. An increase in the equivalent piston area results in a decrease in the dynamic stiffness and loss angle. The inertia track damping coefficient generated by the oscillating fluid between chambers is a function of frequency along with other variables: inertia track equivalent radius, length, fluid density and viscosity. The calculated dynamic characteristics match well

with those from the measurements. With this developed theory, it is possible to develop the hydromount without relying on trial and error procedure, which is lengthy and costly.

Recommendation for Further Research

The hydromount has poorer vibration isolation performance than the rubber mount at high frequencies because of its high dynamic stiffness, which ultimately causes the high damping at high frequencies. Adding a membrane-like floating element, a decoupler, in the hydromount results in lower stiffness that generates low damping at high frequencies. The mechanism of this type of the hydromount has not been well understood yet. Also, the hydromount dynamic properties are displacement amplitude dependent, which was not investigated in this research. Furthermore, the displacement dependent volumetric stiffness and the equivalent radius mechanism are among the unresolved issues as well.

BIBLIOGRAPHY

Bernuchon, M. (1984), *A New Generation of Engine Mounts*, SAE Paper 840259.

Brach, R.M. and Haddow (1993), A.G., *On the Dynamic Response of Hydraulic Engine Mounts*, SAE Paper 931321.

Clark, M. (1985), *Hydraulic Engine Mount Isolation*, SAE Paper 851650.

Corcoran, P.E. and Ticks (1984), G, *Hydraulic Engine Mount Characteristics*, SAE Paper 840407.

Charlton, D.J. and Yang J., *A Review of Methods to Characterize Rubber Elastic Behavior for use in Finite Element Analysis*, Rubber Chemistry and Technology, Vo.67, 1994.

Finney, R.H and Kumar, A., Development of Material Constants for Nonlinear Finite-element Analysis, Rubber Chemistry and Technology, Vo.61, 1988.

Flower, W.C. (1985), *Understanding Hydraulic Mounts for Improved Vehicle Noise, Vibration and Ride Qualities*, SAE Paper 850975.

Ford, D.M. (1997), *Hydraulic Powertrain Mount Characteristics and Simulation*, SAE Paper 973269.

Gau, S.J. and Cotton, J.D. (1995), *Experimental Study and Modeling of Hydraulic Mount and Engine System*, SAE Paper 951348.

Graf, P.L. (1987), *Semi-Active and Active Control of Frame Vibration in Automotive Vehicles*, Ph.D Thesis, Purdue University.

Kim, G. (1992), *Study of Passive and Adaptive Hydraulic Engine Mounts*, Ph.D Thesis, The Ohio State University.

Kim, G. and Singh, R. (1993), *Engine Vibration Control Using Passive, Active, and Adaptive Hydraulic Mount Systems*, SAE Paper 932897.

Kim, G. and Singh R. (1993), *Nonlinear Analysis of Automotive Hydraulic Engine Mount*, Journal of Dynamic Systems, Measurement and Control, Vol.115, No.3.

Kim, G. and Singh R. (1992), *Resonance, Isolation and Shock Control Characteristics of Automotive Nonlinear Hydraulic Engine Mounts*, Transportation Systems,

Proceedings of ASME/WAM, DSC-Vol.44, pp.165-180.

Kreyszig, E., *Advanced Engineering Mathematics*, John Wiley & Sons, Inc., 1993.

Lu, M., Ari-Gur, J., "Study of Dynamic Properties of Automotive Hydrobushing", Advanced Vehicle Technologies, ASME Proc., DE-Vol.106, November 2000, pp.135-140. Submitted to the Journal of Sound and Vibration.

Lu, M., Ari-Gur, J. and Garety, J., "Prediction of Automotive Hydrobushing Resonant frequency", Noise Control and Acoustics Division, ASME Proc., NCA-Vol.26, November 1999, pp.157-159.

Mooney, M., Journal of Applied Physics, Vol. 11, p.582, 1940.

Muzechuk, R.A. (1984), *Hydraulic Mounts-Improved Engine Isolation*, SAE Paper 840410.

Rosenberg, R. and Karnopp, D., *Introduction to Physical System Dynamics*, McGraw Hill, New York, 1983.

Potter, M.C., *Fundamentals of Engineering*, Great Lakes Press, MI, 1993.

Royston, T. and Singh R. (1997), *Study of Nonlinear Hydraulic Engine Mounts Focusing on Decoupler Modeling and Design*, SAE Paper 971936.

Seto, K., Sawatari, K., Nagamatsu, A., Ishihama M.,and Doi, K. (1991), *Optimum Design Method for Hydraulic Engine Mounts*, SAE Paper 911055.

Singh, R., Kim G. and Ravindra P.V. (1992), *Linear Analysis of Automotive Hydro-Mechanical Mount with Emphasis on Decoupler Characteristics*, Journal of Sound and Vibration, V.158.

Sugino, M., and Abe, E. (1986), *Optimum Application for Hydroelastic Engine Mount*, SAE Paper 861412.

Thomson, T.W (1988), *Theory of Vibration with Applications*, Prentice Hall.